Structural and functional investigation of the essential secondary active transporter LicB from the human pathogen *S. pneumoniae*

Inauguraldissertation

zur Erlangung der Würde eines Doktors der Philosophie vorgelegt der

Philosophisch-Naturwissenschaftlichen Fakultät

der Universität Basel

von

Natalie Bärland

Basel, 2023

Genehmigt von der Philosophisch-Naturwissenschaftlichen Fakultät

Auf Antrag von:

Erstbetreuer: Prof. Dr. Camilo Perez,

Zweitbetreuer: Prof. Dr. Sebastian Hiller,

Externe Expertin: Prof. Dr. Ute Hellmich

Basel, 22. März 2022

Prof. Dr. Marcel Mayor

Dekan

Table of Contents

Acknowledgement

I would like to express my gratitude to my supervisor Prof. Dr. Camilo Perez for giving me the opportunity to do my PhD at the Biozentrum of the University of Basel on this challenging, interesting and significant project. I am thankful for the provided scientific environment and the mentoring, which helped me to become the curious and ambitious scientist that I always aspired to be.

I would like to thank our collaborators and colleagues without whom this work would not have been possible: Prof. Dr. Markus Seeger, Prof. Dr. Jan-Willem Veening, Anne-Stephanie Rueff, Cedric Hutter, Gonzalo Cebrero, Andre Bazzone and Maria Barthmes.

I especially thank the committee members Prof. Dr. Sebastian Hiller and Prof. Dr. Ute Hellmich and my former PhD advisory board members Prof. Dr. Tilman Schirmer and Dr. Janet Vonck for their support and advise.

I want to thank Dr. Johanna Ude, Malgorzata Sobota and Dr. Guillaume Mas for proofreading and giving helpful suggestions for improving this work.

I would like to thank the following incredible and inspiring scientists for great discussions, funny, unforgettable moments and for being amazing colleagues who encourage me to keep going: Malgorzata Sobota, Vanessa Malagnino, Daniel Ehrsam, Johanna Ude, Joka Pipercevic, Guillaume Mas, Anima Schäfer, Karol Kaiser, Melanie Engelin and Suvarnan Selliah.

I want to express my greatest gratitude to my parents, my sister, to my whole family and friends, for their kindness and their support not only, but especially, during this period of my life. I could not imagine a world without you and I am grateful to have you. Namely I would like to thank Sona Avetisjan, Anna Magos, Thomas Ellinghaus, Sarah Newberry, Dario Sanchez, Ivan Yanez, Jennifer Assaturi, Katharina Egner, Ina Derewjanko and Babak Aghahassani for always being there for me and checking in on my vital signs.

Last but not least I would like to thank Tina, Andy, Lionello, Doris, Lynsey, Anja, Jana and Jonas for pushing me to run faster and climb higher.

Abbreviations

AATGal	2-acetamido-4-amino-2,4,6-trideoxygalactose
ABC	ATP-binding cassette
ATP	Adenosine triphosphate
BAT	Bacterial/archaeal transporter
BLM	Black lipid membrane
CBP	Choline binding protein
CbpA	Choline-binding protein A
CbpE	Choline-binding protein E
CDP	Cytidin diphosphate
ChoP	phosphorylcholine
CST	CMP-sialic acid transporter
cryo-EM	Cryogenic electron microscopy
CTF	Contrast transfer function
DDD	Direct detection device
DMT	Drug/metabolite transporter
Fab	Antigen fragment
FSC	Fourier shell correlation
GalNAc	N-acetylgalactosamine
Glc	Glucose
HC-3	Hemicholinium-3
LPS	Lipopolysaccharides
LR	Laminin receptor
LTA	Lipoteichoic acids
MDR	Multidrug-resistance
NADPH	Dihydronicotinamide adenine dinucleotide phosphate
NST	Nucleotide sugar transporter
PAFR	Platale-activating factor receptor

PCV	Pneumococcal conjugate vaccines
PG	Peptidoglycan
PIGR	Polymeric immunoglobulin receptor
SLC	Solute carrier transporter
SMR	Small multidrug resistance
SNR	Signal-to-noise ratio
SSM	Solid-supported membrane
TA	Teichoic acids
TM	Transmembrane
TPT	triosephosphate/phosphate translocator
UDP	Uridine diphosphate
WTA	Wall teichoic acids
2D	Two dimensional
3D	Three dimensional

Abstract German

Streptococcus pneumoniae ist ein menschliches Pathogen, das milde Symptome hervorrufen kann, aber auch das Potential trägt, um schwerwiegende Infektionen in der Lunge oder im Gehirn auszulösen. Als ein Gram-positives Bakterium trägt es sogenannte Teichonsäuren auf dessen Oberfläche. Bei den Teichonsäuren unterscheidet man zwischen zwei Arten, die entweder in der Membran eingebettet sind oder an die Mureinschicht gebunden sind. Die Synthese der Teichonsäuren in *S. pneumoniae* ist einzigartig, da beide durch einen geteilten Weg der Biosynthese hergestellt werden. Ein anderes einzigartiges Merkmal ist, dass die Teichonsäuren mit Phosphorylcholin modifiziert werden. Das Anhängen von Phosphorylcholin findet an der Innenseite der Membran während der Synthese der entstehenden Teichonsäurekette statt und nur diejenigen Teichonsäuren, die mit Phosphorylcholin modifiziert sind, werden an die Oberfläche exportiert. Cholin ist das Substrat für die Phosphorylcholin Einheiten und essentiell für das Überleben von *S. pneumoniae*. Das Substrat kann vom Bakterium nicht synthetisiert werden, sondern muss von einem sekundär aktiven Transporter, genannt LicB, importiert werden. Der Transporter gehört zur *Drug/Metabolite* Transporter Superfamilie, die aus Transportern mit zehn Transmembranhelices bestehen. Die Gemeinsamkeit der Transporter besteht darin, dass diese aus zwei invertierten, wiederholenden Einheiten bestehen, die durch Genduplikation entstanden sind. Die Struktur und die Funktion von LicB wurden bisher nicht beschrieben und Strukturen bekannter Mitglieder der *Drug/Metabolite* Superfamilie sind karg und beschreiben größtenteils nur einen kleinen Ausschnitt dieser Superfamilien.

Diese Arbeit beschreibt die Funktion und die strukturellen Merkmale des Cholinimporters LicB der Pneumokokken. Der Transporter weist ein substratverbreitertes Verhalten auf, bei dem es nicht nur Cholin, sondern auch Arsenocholin und Acetylcholin importiert. Die mittlere effektive Konzentration wurde mittels *Solid Supported Membrane* Elektrophysiologie zu 47 ± 15 µM für Cholin,

170 ± 9 µM für Arsenocholin und 740 ± 84 µM für Acetylcholin bestimmt. Radioaktiv markiertes Acetylcholin wurde zum Cholin-armen Medium zugesetzt, um *S. pneumoniae* Zellen heranzuziehen und anschließend die Teichonsäuren zu extrahieren. Die extrahierten Teichonsäuren weisen ein radioaktives Signal auf, das den Beweis für den Import und die Katabolisierung von Acetylcholin als alternative Cholinquelle liefert. Protonenkopplung, als treibende Kraft für den *Alternating Access* Mechanismus des Transportzyklus, wurde durch ein fluoreszenzbasiertes Assayverfahren bestätigt.

Zusätzlich dazu wurde eine synthetische Nanokörperbibliothek, die gegen LicB selektiert wurde, basierend auf dessen inhibitorisches Potential charakterisiert, bei der einzigartig bindende Nanokörper identifiziert wurden. In diesem Fall hat sich *Solid Supported Membrane* Elektrophysiologie als eine robuste und schnelle Methode zum Filtern von inhibitorischen Nanokörpern bewährt und bietet sich zur Anwendung an anderen Zielproteine als potentielles Arzneimittel an. Die Struktur des Transporters LicB wurde mittels Röntgenkristallographie im substratgebundenen, verschlossenen Zustand bei einer Auflösung von 3.8 Å bestimmt. Mittels *single particle cryo-EM* wurde LicB in Nanodiscs rekonstituiert, an einen synthetischen Nanokörper gebunden und im nach außen gekehrten Zustand bei einer Auflösung von 3.75 Å bestimmt. Der Transporter spielt eine zentrale Rolle für das Überleben des menschlichen Pathogens und die Kenntnis über dessen Struktur, die Funktion und die Identifizierung inhibitorischer, synthetischer Nanokörper bieten eine Plattform für die Entwicklung antimikrobieller Arzneimittel und neuartiger Alternativen zur Bekämpfung von Pathogenen.

Abstract English

Streptococcus pneumoniae is a human pathogen that can cause mild symptoms but also exhibits the potential to cause severe infections in the lungs or the brain. As a Gram-positive bacteria it has teichoic acids attached to its surface, where there are two types which are either embedded in the membrane or bound to the peptidoglycan. The synthesis of those teichoic acids is unique for *S. pneumoniae*, as it shares the same biosynthetic pathway for both types. Another unique feature is their modification with phosphorylcholine. The attachment of phosphorylcholine happens at the inner leaflet during the synthesis of the nascent teichoic acid chain and only those modified teichoic acids are exported to the surface. Choline is the substrate for the phosphorylcholine moieties and is essential for the survival of *S. pneumoniae*. The substrate cannot be synthesized by the bacteria and can only be imported by a secondary active transporter denoted as LicB. This transporter belongs to the drug/metabolite transporter superfamily, which is comprised of transporters with ten transmembrane helices of two inverted repeats arising from internal gene duplication. The structure and function of LicB has not been described before and known structures of other members of the drug/metabolite transporter superfamily are sparse and mostly describe only a small part of the families.

This study describes the functional and structural features of the pneumococcal choline importer LicB. LicB exhibits promiscuous transport behavior, where it shows to transport not only choline but also arsenocholine and acetylcholine. The half maximal effective concentrations have been determined by solid supported membrane electrophysiology to 47 ± 15 µM for choline, 170 ± 9 µM for arsenocholine and 740 ± 84 µM for acetylcholine. Radiolabeled acetylcholine was supplemented in choline reduced media to grow *S. pneumoniae* cells and to subsequently extract the teichoic acids. The extracted teichoic acids exhibited a signal which provides evidence of the import and catabolization of acetylcholine as an alternative choline source. Proton-coupling as the driving force for the alternating access mechanism

during the transport cycle has been confirmed with a fluorescence-based assay. Additionally, a library of synthetic nanobodies, selected against LicB, was characterized based on their inhibitory potential resulting in the determination of several unique inhibitors. In this case solid supported membrane electrophysiology has proven to be a robust and fast technique to screen inhibitory nanobodies and presents an application for other potential drug targets. The structure of the transporter LicB was solved in the substrate bound occluded state at a resolution of 3.8 Å via x-ray crystallography and in the outward facing state, reconstituted into nanodiscs and bound to a synthetic nanobody at a resolution of 3.75 Å via cryo-EM. The transporter plays a crucial role for the survival of the human pathogen and the knowledge about the structure, the function and the identification of inhibitory synthetic nanobodies can help to provide a platform for antimicrobial drug development and for novel alternatives to combat pathogens.

1 Introduction

1.1 Pneumococcal virulence and choline import

1.1.1 History of antibiotics and antibiotic resistances

In 1928 in the laboratory of the St Mary's Hospital London a now famous piece of mould contaminated a petri dish belonging to the microbiologist Alexander Fleming[1]. The mould was producing a substance that was killing bacteria surrounding it. This substance, penicillin, was further developed by Fleming and others into a drug that could cure bacterial infections and would revolutionize our healthcare[2,3]. It became one of the greatest medical advances of the 20th century and common and deadly illnesses such as pneumonia and tuberculosis could now be treated. Life expectations were extended and dangers of infections from small cuts, routine surgeries and childbirth were vastly reduced[4,5].

But unfortunately bacteria and other pathogens have intrinsic and acquired mechanisms to resist drugs that are made to combat them[6,7]. There are two important pathways with which bacteria can acquire resistances: from mutations of the existing genome[8,9] or from the uptake of foreign DNA[10]. Those important processes already existed long before the introduction of antibiotic use in healthcare and evolved due to strong selection pressures in the environment[11,12]. Penicillin was introduced to the market in the 1940s and shortly after its introduction the first resistant bacterial strain was discovered which threatened the antimicrobial advancements during the 1950s[13,14]. Soon after, other novel types of beta-lactam antibiotics were discovered and developed. One of those antibiotics was methicillin but as in the previous cases and already in the same decade of its introduction, the first methicillin-resistant bacterial strains were reported[13,15].

Reasons that contribute to antimicrobial resistances are manyfold and can be found in nature or are manmade, starting with the over-prescription of antibiotics[16,17], patients not finishing their treatments, large and often unnecessary overuse in

livestock and fish farms[18], poor hygiene in hospitals[19], poor sanitary conditions[20] and the lack of development of novel antimicrobials[21]. This additional survival pressure on the bacteria due to the use of antibiotics, increases the chances of occurrence of antibiotic resistances.

1.1.2 Virulence and antibiotic resistance of *Streptococcus pneumoniae*

Strains of bacteria that exhibit antimicrobial resistances to drugs that usually target them are responsible for life-threatening infections, are a global burden and called 'superbugs'. One of those superbugs is *S. pneumoniae*[22,23], a highly invasive human pathogen that is harbored in the nasopharynx, a part of the nasal airways. Up to 27-65% of healthy children and between 5% to 30% of healthy adults can be carriers of the bacteria[24-26]. The bacteria can cause mild to severe infections and propagate to the ears, the sinus, the bloodstream, the lungs and even to the brain, if they cross the blood brain barrier[27] (**Figure 1**). The mortality rate of meningitis caused by *S. pneumoniae* is associated to 16% - 37%. About 30% - 50% of adults surviving those infections, are presenting permanent symptoms due to irreversible damages in the brain[28,29].

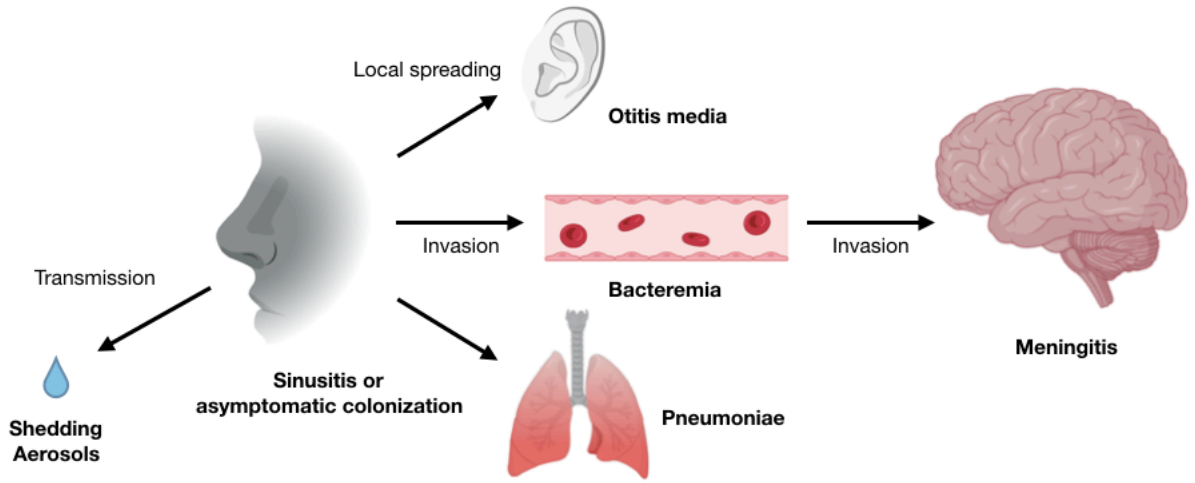

***Figure 1**: Pathogenesis of S. pneumoniae. S. pneumoniae can asymptomatically colonize the nasopharynx and is transmitted via shedding through aerosols. The bacteria can spread and invade other organs, where it can cause sinusitis, otitis media, bacteremia, pneumoniae or meningitis. Figure created with BioRender.*

The World Health Organization included *S. pneumoniae* as one of nine priority pathogens of international concern in 2014[30]. Similar to other superbugs it developed resistances to antibiotics shortly after their introduction (**Figure 2**)[31-33]. Penicillin and cephalosporin belong to the class of β-lactam antibiotics and as such they inhibit the final steps of the peptidoglycan (PG) synthesis[34]. Since the PG is a part of the bacterial cell wall of both Gram-positive and Gram-negative bacteria, those antibiotics are therefore used against both types of bacteria. The first resistances against penicillin in *S. pneumoniae* were reported in the 1960s and those against cephalosporin in the 1980s[33]. Erythromycin is another type of antibiotic and was introduced to the market in 1953. It belongs to the class of macrolide antibiotics that inhibit bacterial protein synthesis by binding to a component of the 50S ribosomal subunit[35]. The first pneumococcal strain resistant to erythromycin was already reported 15 years after the introduction of the antibiotic in 1968.

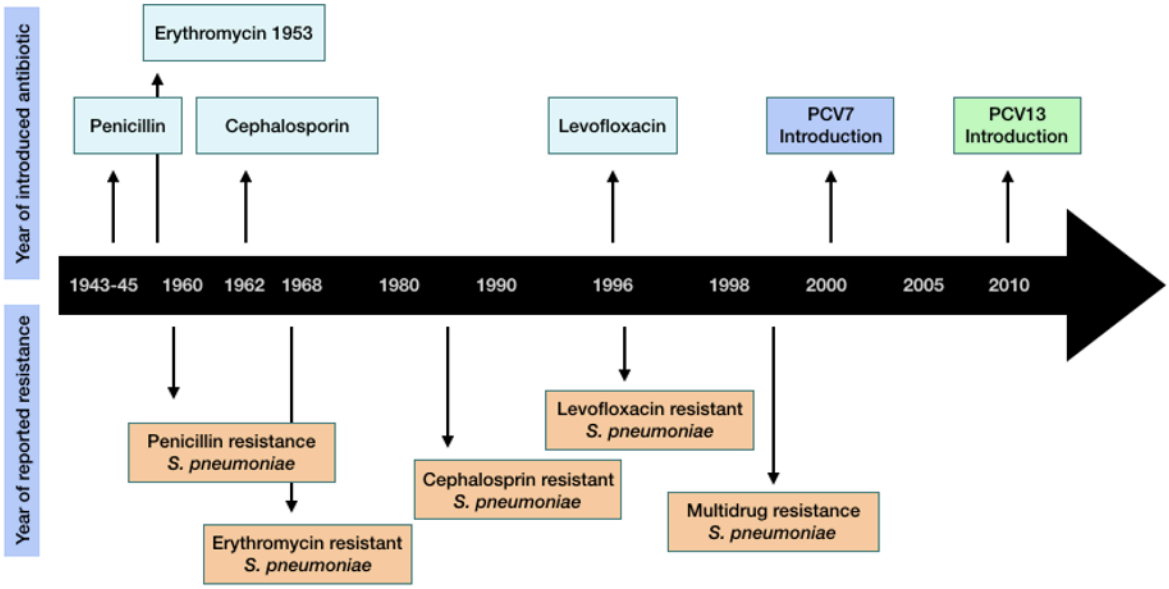

***Figure 2**: Timeline of the introduction of antibiotics and occurrence of resistance in S. pneumoniae. The introduced antibiotics and pneumococcal conjugate vaccines (PCV) are shown on the upper half of the figure, whereas the first reported resistant strains of S. pneumoniae are shown at the lower half of the figure. Figure adapted and modified from Cillóniz et al., 2018.*

This rapid emergence of antimicrobial resistance to β-lactams, macrolides and other types of antimicrobials is a major global concern. Multidrug-resistant (MDR) strains exhibit resistance to two or more antibiotics are an additional burden[33,36-39] and the

first MDR strains of *S. pneumoniae* resistant to erythromycin, clindamycin, tetracycline and chloramphenicol or those resistant to penicillin, chloramphenicol and tetracycline were reported in 1977[33]. The prevalence of MDR *S. pneumoniae* ranges geographically from 36% in Asia to 15% in Europe[36,40]. It is estimated that 30% of the severe hospital acquired infections are caused by *S. pneumonia* strains which are resistant to one or more antibiotics. This makes the treatment extremely challenging especially for patients with a suppressed immune system, children and the elderly. Pneumococcal conjugate vaccines (PCV) help to prevent infections but only target a fraction of the known pneumococcal serotypes[41,42]. Nevertheless, vaccines aid to lower the incidents of infections significantly[43,44].

Community acquired pneumoniae remains associated with high morbidity and mortality up to this day[45]. Here, especially MDR pathogens contribute to challenges for clinical management and patient treatments and the search for novel drugs and drug targets remains crucial[36].

1.1.3 Teichoic acids synthesis in Gram-positive bacteria and in *S. pneumoniae*

For over a decade we have known about the existence of two types of bacteria, those that exhibit a Gram-coloring, the Gram-positives and those bacteria that do not exhibit any coloring, the Gram-negatives[46]. The main difference between these two types is the composition of the cell envelope. Both bacteria have an inner membrane and a layer. However, Gram-positive bacteria have a thicker PG layer of up to 10-30 nm[47] and no outer membrane, compared to Gram-negative bacteria. Gram-positive bacteria have their name from the fact that the Gram-staining can be retained by the PG that is accessible due to the absence of the outer membrane and cause the typical staining[46].

While the outer membrane of Gram-negative bacteria is important for cell stability, cell integrity, protection from toxic molecules in the environment and cell turgor among other things[47-50], the thicker PG layer in Gram-positive compensates for the absence of an outer membrane[47]. It is possible to draw some conclusions on

virulence from the different compositions of the surface exposed polymers and their modifications. Those polymers are so-called lipopolysaccharides (LPS) in Gram-negative bacteria[49,51] and the teichoic acids (TA) in Gram-positive bacteria[52]. The LPS from Gram-negative bacteria are attached to the outer layer of the membrane (Figure 3A). Its surface exposed O-antigens is composed of oligosaccharide repeating units which are attached to the LPS. Those are highly diverse depending on the bacterial strain and are an important virulence factor[53-56]. Gram-positive bacteria on the other hand have two types of anionic polymers (Figure 3B) which can be either attached to the membrane, the so-called lipoteichoic acids[57-59] (LTA) or to the peptidoglycan layer, which are then denoted as wall teichoic acids[60-62] (WTA).

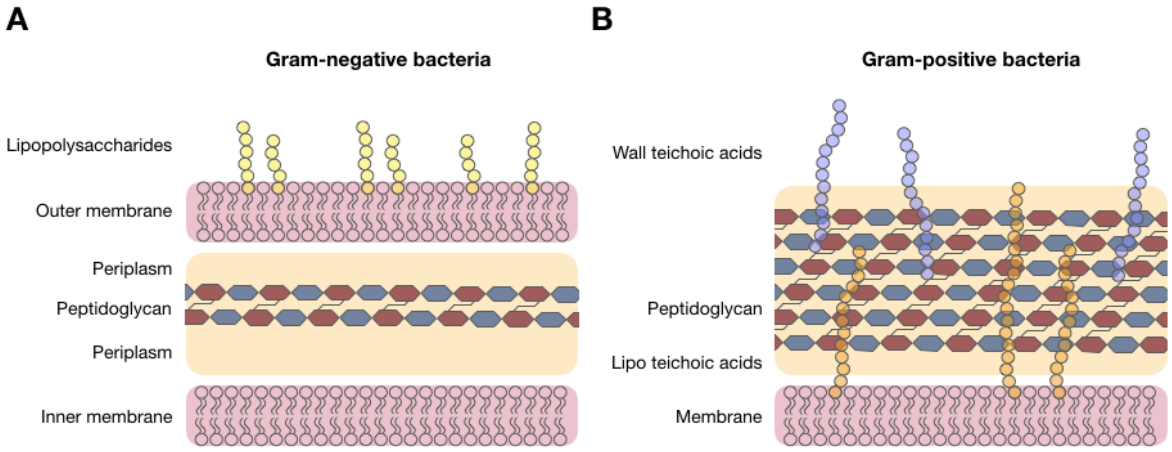

*Figure 3: Differences in cell wall composition of Gram-positive and Gram-negative bacteria. **A.** The cell wall of Gram-negative bacteria consists of the inner and outer lipid membrane and a thin peptidoglycan layer. The periplasmic space is located on both sides between the membrane and the peptidoglycan. Lipopolysaccharides are attached to the outer membrane and exposed to the surface. **B.** Gram-positive bacteria lack an outer membrane but have a thick layer of peptidoglycan. They lack LPS but have another type of anionic polymers, the teichoic acids, that are exposed to the surface. Those teichoic acids are either attached to the peptidoglycan and are called wall teichoic acids or are attached to the inner membrane by diacylglycerol and called lipoteichoic acids.*

Teichoic acids are important for the survival of the bacteria, to maintain cell shape and keep the integrity of the cell[63]. They exhibit a variety of modifications at their surface, e.g. the modification with D-alanyl ester residues that, together with the peptidoglycan, form a polyanionic matrix[52]. This anionic charge is important for cation homeostasis, trafficking of ions, small molecules and it protects the bacteria against

cationic antimicrobial peptides[64]. For most Gram-positive bacteria the composition and the synthesis of LTAs and WTAs differ significantly. The LTAs can be divided into five classes[57,65] and the WTAs into four classes[65,66], depending on their repeating units. Type I LTAs are comprised of linear glycerol phosphates. They are generally synthesized at the outer leaflet of the membrane, after its glycolipid anchor is flipped to the outside[67,68] (**Figure 4A**). The glycolipid anchor in *Staphylococcus aureus* is synthesized by the glycosyltransferase YpfP and flipped to the outside by LtaA. Several glycerol phosphate molecules are then attached to the nascent chain by the LTAs synthetase LtaS, before it is further modified with D-alanyl ester residues[69].

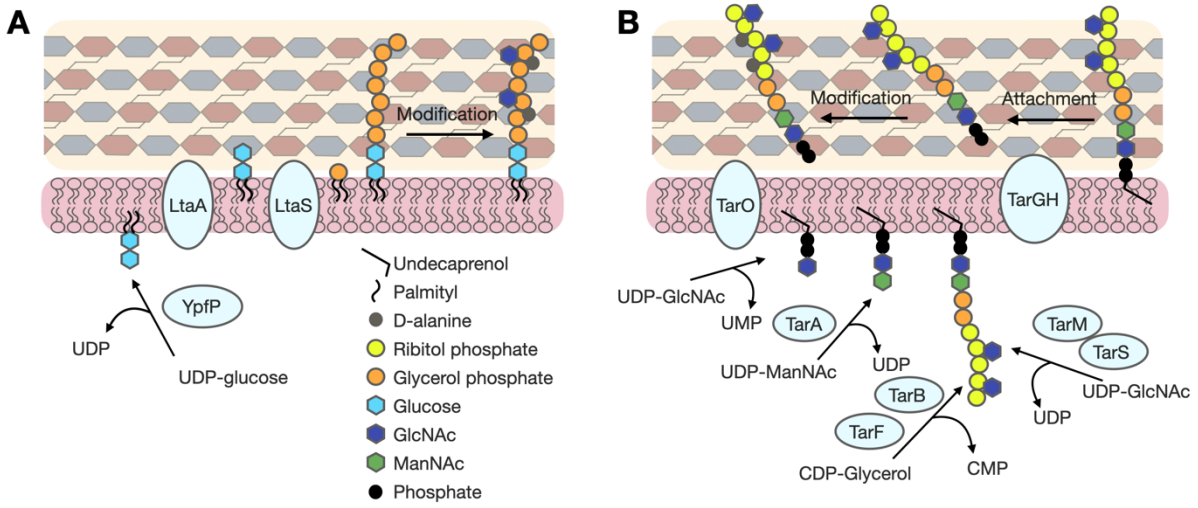

***Figure 4**: Biosynthetic pathways of the synthesis of teichoic acids in S. aureus. **A**. Biosynthetic pathway of type I LTA starts at the inner leaflet of the membrane. After the synthesis of the glycolipid anchor, it is transported to the outer leaflet and the LTA is synthesized by the transfer of glycerol phosphates. The LTA is then modified with glucose and D-alanines. **B.** The type I WTA is synthesized at the inner leaflet of the membrane, where residues of GlcNAc, ManNAc, glycerolphosphates and ribitolphosphates are attached, before the nascent chain is flipped to the outer leaflet. The nascent chain is then attached to the peptidoglycan and further modified with D-alanines. Figure adapted and modified from van der Es et al., 2017.*

Type I WTAs from *Bacillus subtilis* and *S. aureus* are comprised of glycerol phosphates and ribitol phosphate repeating units. They are synthesized at the inner leaflet of the membrane, flipped to the outside and attached to a muramic acid moiety via a phosphodiester linkage to the peptidoglycan[70] (**Figure 4B**). In the initial steps of the type I WTAs synthesis in *S. aureus*, the linker is synthesized by consecutive actions of TarO and TarA[70]. Cytidin diphosphate glycerol (CDP-glycerol) is then used

as a glycerol phosphate donor by TarB to transfer glycerol phosphates onto the linker. The poly (ribitol phosphate) chain is then created by the attachment of another glycerol phosphate moiety by TarF and ribitol phosphate polymers by TarL using the substrate CDP-ribitol. TarM and TarS further modify the chain with carbohydrates[71] and the complete polymer is then transported through the membrane by TarGH[70].

The synthesis of teichoic acids in *S. pneumoniae*, on the other hand, is unique and differs significantly from the one of the type I teichoic acids[72]. Pneumococcal LTAs and WTAs are synthesized through a single pathway and only later, after being flipped across the membrane, divided into LTAs and WTAs. Both teichoic acids in *S. pneumoniae* therefore have identical repeating units and length distributions of their chains[73]. *S. pneumoniae* synthesizes a very elaborate and complex type of teichoic aicds at the inner leaflet of the membrane (**Figure 5**). It is of the type IV LTAs that consist of a repeating unit containing 2-acetamido-4-amino-2,4,6-trideoxygalactose (AATGal), glucose (Glc), ribitol phosphate and N-acetylgalactosamine (GalNAc). In the first step of the synthesis the sugar AATGal is transferred to the undecaprenyl-phosphate lipid anchor[72,74]. The source of the sugar is a chemically activated UDP-AATGal, converted from UDP-GlcNAc as a precursor by a subsequent activity of a dehydrase and an aminotransferase[75]. In the following step a glycose residue is attached by a glycosyltransferase[72,76]. CDP activated ribitol is acquired through the activity of the two enzymes TarJ and TarI[77]. TarJ requires NADPH for the synthesis of ribitol-5-posphate, which is then used by the cytidylyl transferase TarI to form CDP-ribitol. The phosphotransferase LicD3 is then transferring ribitol with the substrate CDP-ribitol onto the nascent teichoic acid chain. The repeating unit core is completed through the attachment of two GalNAc residues by two glycosyltransferases[72].

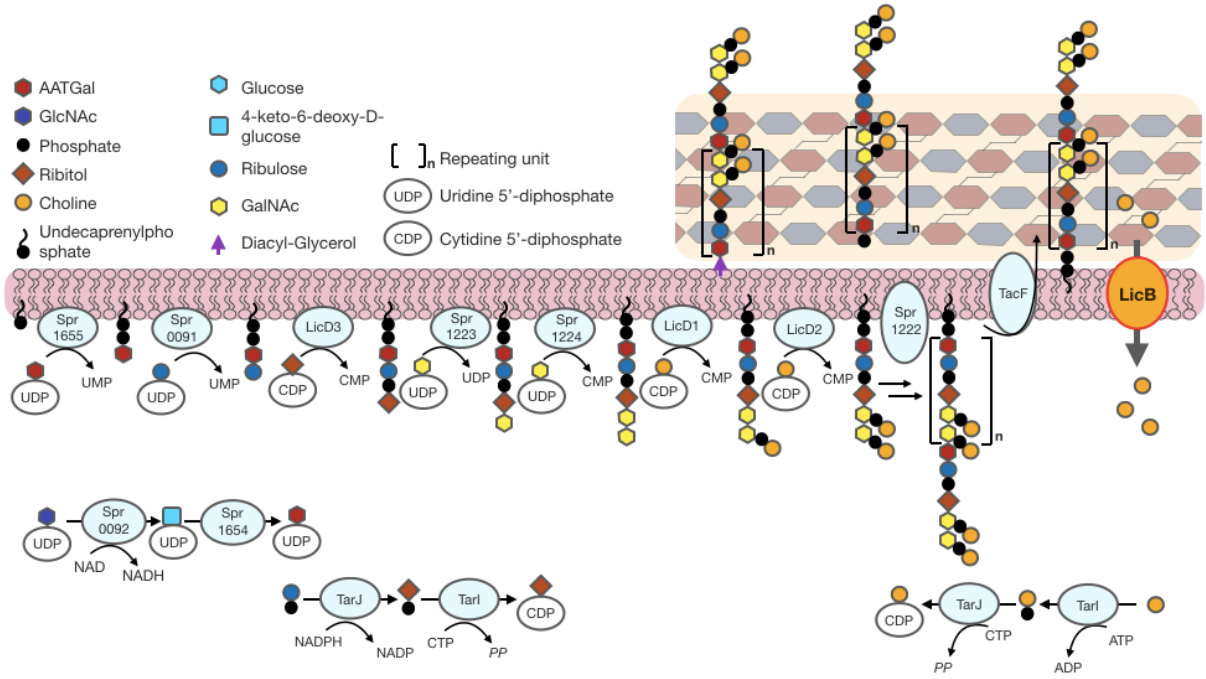

***Figure 5**: Biosynthetic pathway of teichoic acid synthesis in S. pneumoniae. The synthesis of LTAs and WTAs in S. pneumoniae is shared for both teichoic acids and starts with the synthesis of a type IV LTAs at the inner leaflet of the membrane. The precursor for the synthesis is an undecaprenyl phosphate that is attached to the membrane and to which residues of different sugars are attached. The attachment is carried out by several membrane associated proteins and the repeating units, i.e. UDP-AATGal and CDP-ribitol, are chemically activated and provided by soluble proteins. The nascent chain is modified with phosphorylcholine moieties. CDP-choline is chemically activated and its precursor choline can only be acquired exogenously through the choline importer LicB. After the chain has been synthesized and modified with phosphorylcholine residues, it is flipped outside and either attached to a diacylglycerol anchor at the inner membrane, yielding a LTA, or to the peptidoglycan, yielding a WTA. Figure adapted and modified from Denapaite et al., 2012.*

Another unique characteristic for pneumococcal teichoic acids is their modification with phosphoryl choline[78], similar to *Haemophilus influenzae*, a Gram-negative human pathogen with phosphorylcholine decorated lipopolysaccharides[79]. *S. pneumoniae* cannot synthesize choline from other compounds and imports choline with a putative secondary active transporter from the drug/metabolite transporter (DMT) superfamily, LicB[79,80]. The imported choline is then phosphorylated by the choline kinase LicA[81]. The cytidylyl transferase LicC activates phosphorylcholine into CDP-choline[82,83]. CDP-choline is used as a substrate by LicD1 and LicD2, which attach phosphorylcholine moieties at the GalNac residues on the nascent chain[84]. Both phosphorylcholine

transferases exhibit high specificity for the location of the modification[85]. LicD1 specifically attaches phosphorylcholine moiety to the α-GalNAc position, whereas LicD2 only attaches the moiety to the β-GalNAc position of the nascent chain. The nascent chain is further polymerized by a so far unknown putatively highly hydrophobic membrane protein Spr1222[72]. The transmembrane transporter TacF flips the teichoic acid to the outer leaflet[76], where it is either attached to the peptidoglycan to yield a WTA, or to the glycolipid anchor to yield a LTA. Additionally to the phosphorylcholine modification on the teichoic acids, it has been shown that *S. pneumoniae* has a pathway for D-alanylation of the teichoic acids and teichoic acids have been shown to contain D-alanines[86].

1.1.4 Choline requirement in *S. pneumoniae*

Choline is an essential nutrient for mammals that needs to be supplemented additionally to the endogenous synthesis in the liver and the brain[87]. In humans and other rodents it plays an important role for the maintenance of cell membranes, synthesis of phospholipids, for the synthesis of acetylcholine for cholinergic neurotransmission and the methyl metabolism for epigenetic changes among others[88,89]. Research on humans and rodents shows that choline is required for the development of the brain and for cognition[90-92]. Choline deficiency can lead to pathological conditions such as epilepsy, schizophrenia or Alzheimer's disease[93]. Because of its central role in key processes and functions, several specific choline transporters can be found in human cells that can take up the hydrophilic cation[94]. There are low affinity choline importers that supply choline for the synthesis of phosphatidylcholine and other lipids[95], and there are high affinity choline transporters located at pre-synaptic clefts of cholinergic nerves[96-98]. The latter is putatively coupled to the synthesis of acetylcholine in the brain. Another human choline transporter has been recently found to be involved in choline import in the plasma membrane and in mitochondria[99].

For bacterial cells, choline mostly plays an important role in the glycine-betaine pathway for osmoregulation[100]. Choline is for example supplied externally by the BetT importer in *E. coli*[101], which then synthesize the osmolyte glycine betaine if other compatible solutes are not available for the compensation for osmotic stress[100,102].

Some respiratory tract pathogens, on the other hand, have a unique way of using choline, decorated as phosphorylcholine moieties on their surface exposed polymers, to invade host cells[103-105]. *H. influencae* and *S. pneumoniae* are both human pathogens that are harbored in the nasopharynx and exhibit phosphorylcholine moieties as part of their LPS[106] and teichoic acids[84], respectively. It has been known for a long time that choline is an essential growth factor for *S. pneumoniae* [107] but it is unique for this Gram-positive human pathogen that choline is used exclusively for the decoration of its teichoic acids[108,109]. There are two main pathways by which those pathogens can invade host cells. They can either mimic choline and interact with abundant host receptors that bind choline, or by so called choline binding proteins (CBP) that are attached on the phosphorylcholine moieties of the pneumococcal teichoic acids. In the first scenario, the phosphorylcholine moiety can interact with the platale-activating factor receptor (PAFR) or the laminin receptor (LR) to allow to adhere to host cells[110]. The PAFR and LR receptors are highly abundant proteins that are expressed on the surface of many human cells, where the PAFR accepts phosphorylcholine as its natural ligand[24,111,112]. The other pathway of invasion follows pneumococcal CPBs and their various functions involved in the adherence and invasion of host cells[113]. CBPs are a unique group of cell-wall associated proteins that bind non-covalently to the phosphorylcholine moieties of the teichoic acids[113-115] (Figure 6A). All CBPs have a conserved choline binding domain of two or more repeats of a 20-amino acid long sequence. Pneumococcal CBPs have been described to be involved in autolysis[105], separation of the daughter cell[116], lysozyme-like activity[117], adherence to epithelial cells[118], virulence[119,120] and colonization[121]. Some of those CBPs, together with the phosphorylcholine moieties on the teichoic acids, are crucial for several stages of pneumococcal adherence and invasion of host

cells[27,122]. The process is summarized schematically in Figure 6B. One of the first steps during pneumococcal invasion of the respiratory tract is the clearance of the mucus and mucucilia, by proteolytic degradation and deglycosilation[123]. The clearance allows the adherence of the pathogen to the apical surface of the epithelial cells. The adherence is mediated by phosphorylcholine and choline-binding protein A (CbpA, also known as PspC)[111,124]. The phosphorylcholine can bind to the PAFR[111] whereas CbpA is able to bind to the polymeric immunoglobulin receptor (PIGR)[124]. Both events can induce endocytosis, where the pneumococcal cell is taken up and released in the basolateral compartment[125,126].

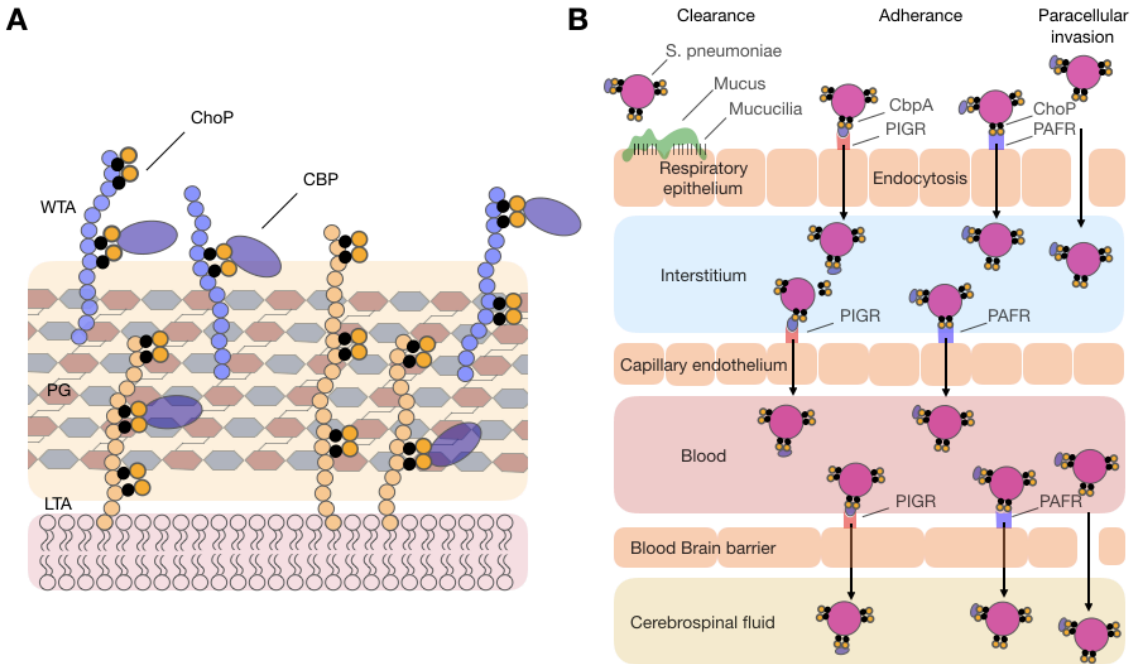

Figure 6: Invasion and adherence to host cells by pneumococcal teichoic acids decorated with phosphorylcholine (ChoP) and choline binding proteins. ***A.*** *CBPs are non-covalently attached via the choline binding domain to phosphorylcholine decorated teichoic acids on the surface of S. pneumoniae.* ***B.*** *The pneumococcal cell clears the mucus and the mucucilia by proteolytic degradation and deglycosylation. ChoP or CbpA can then interact with the PAFR or the PIGR receptor to adhere to cells. Such receptor interactions at the epithelial or the endothelial cells can induce endocytosis of the bacterial cell and its release to the basolateral epithelium or into the bloodstream. The epithelial barrier can also be crossed through the degradation of the extracellular matrix through the involvement of the CbpE. The blood-brain barrier can be crossed through the interaction of ChoP with the PAFR, CbpA with the PIGR or LR, respectively. Figure adapted and modified from Weiser et al., 2018.*

A paracellular invasion is possible through the direct damage of the epithelium and the degradation of the extracellular matrix by choline-binding protein E (CbpE)[127]. The capillary endothelial barrier and the blood-brain barrier can be crossed to enter the bloodstream by the same mechanism of interaction of phosphorylcholine-PAFR or CbpA-PIGR[111,125,126]. Additionally, CpbA can interact with the LR at the blood-brain barrier[24].

The pneumococcal cells can undergo opacity phase variations during the process of invasion, depending on the environment and the stage of invasion which upregulates key virulence factors[122,128]. Those two types are called transparent and opaque, where the transparent type can be typically isolated from the nasopharynx and the opaque type can be typically harvested from the blood. During stages of adhesion the transparent type of pneumococcal strains is dominant with upregulated levels of expression of phosphorylcholine[129] and CbpA[121]. The opaque type is a phagocytosis resistant phenotype and is dominant when the bacteria is in the blood stream. During that stage the expression of PspA is upregulated[119,130]. PspA is another pneumococcal choline-binding protein and involved in the protection against apolactoferrin, a bactericidal against *S. pneumoniae*.

Because of the essential role of phosphorylcholine moieties and the CBPs, that are involved in many crucial processes and dependent on choline for binding at the bacterial surface, it is not a surprise that the disruption of choline supply leads to cell death in pneumococci[107]. Because of the abundance of choline in the human body, it is not possible to cut the pneumococcal supply by decreasing choline levels as a potential treatment for pneumococcal infections, but there is another potential drug target involved in the import of choline. It is known from knockout studies, that there is only a single transporter involved in choline import, which is the secondary active transporter LicB from the DMT superfamily. Until now, this membrane protein has neither been characterized functionally nor structurally and it is the aim of this study.

1.2 Transport across membranes

1.2.1 Diffusion, passive and active transport

Lipid membranes are natural barriers that separate cells, organelles and the nucleus for compartmentalization and as protective layers from the exterior[131,132]. The membrane is a bilayer of lipids and semi-permeable for some small hydrophobic molecules, like water, ethanol or urea. Those molecules can cross the barrier freely along their concentration gradient. Charged or large molecules, on the other hand, cannot cross the lipid bilayer[133]. However, all living organisms need to exchange solutes and molecules in order to perform various functions. Because the majority of biologically important molecules are impermeable for the membrane, they require facilitated transport[134,135]. This comes in the shape of porins, pumps or carriers[136-139]. Those proteins are integral membrane proteins spanning from one side of the membrane to the other to grant access across the membrane (Figure 7).

Porins, also called channels, are membrane spanning, rigid proteins with an opening through which a substrate can cross the membrane[140,141]. The transport through porins happens passively and along a concentration gradient. It therefore requires no energy. Porins and channels are usually highly substrate specific and often have conserved residues that form a selectivity filter[142,143]. On the other hand, transport against the concentration gradient of a substrate requires energy and is carried out by pumps through active transporters[144,145]. Pumps, or transporters, are divided into primary active transporters and secondary active transporters, depending on their energy source. The energy source of primary active transporters comes from chemical processes like the hydrolysis of ATP[146,147]. The most common superfamilies of primary active transporters with shared folds and mechanisms are the ATP-binding cassette (ABC) transporters[148,149], V-type[150,151], F-type[152] and P-type[153] ATPases. Secondary active transporters on the other hand use energy coming from the membrane potential, the proton motive force or from the co-transport of another substrate along its concentration gradient[137,154]. Those transporters are called

uniporters, if they transport only one substrate, symporters, if they transport two substrates in the same direction and antiporters, if they transport two substrates in opposite directions[155,156]. Secondary active transporters can be divided into distinct families depending on sequence or structural similarity. The major facilitator superfamily[157,158], the LeuT fold superfamily[159-161] and the solute carrier transporter (SLC) family in humans[162-165] have been studied extensively and exhibit distinct types of transport mechanisms. Furthermore, the DMT superfamily is a highly interesting transporter superfamily whose family members have striking structural and functional similarities to several subfamily members of the SLC family.

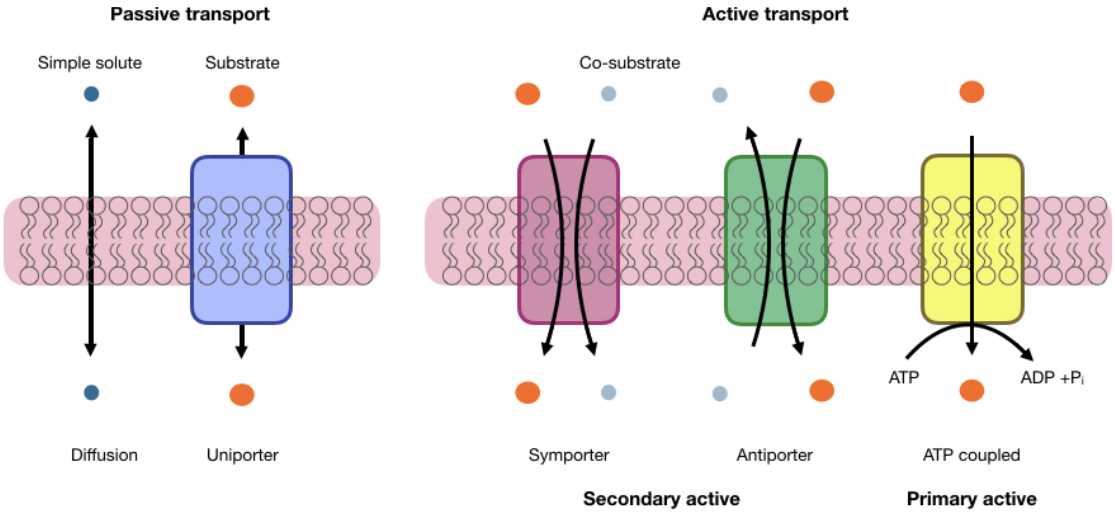

Figure 7: Substrate transport across the membrane. Small and hydrophobic molecules can cross the lipid bilayer through simple diffusion along their concentration gradient. Diffusion can be facilitated with porins or channels. These are rigid membrane proteins that form a pore for the translocation of the substrate along its concentration gradient. Active transporters can facilitate substrates against their concentration gradient. They either use chemical energy (primary active transporters) or secondary energy sources like electrochemical potentials, proton-motive force, etc. (secondary active transporters). Uniporters translocate only one molecule. Symporters transport two molecules in the same direction across the membrane. Antiporters translocate two molecules in opposite directions.

Primary and secondary active transporters undergo conformational changes during the transport of substrates[138,166,167] through an alternating access mechanism[168]. This concept describes, that the substrate binding site is only accessible to one side of the membrane, where the transporter undergoes conformational changes between facing to the outward and to the inward of the membrane. In this concept the

substrate binding site is only accessible to one side of the membrane at a time and the access to the substrate binding site alternates between the outward facing side and the inward facing side of the membrane (Figure 8A). Three general mechanisms have been described for secondary active transporters. Those are the rocker switch[169], the rocking bundle[161,170], and the elevator mechanisms[171,172] (Figure 8B).

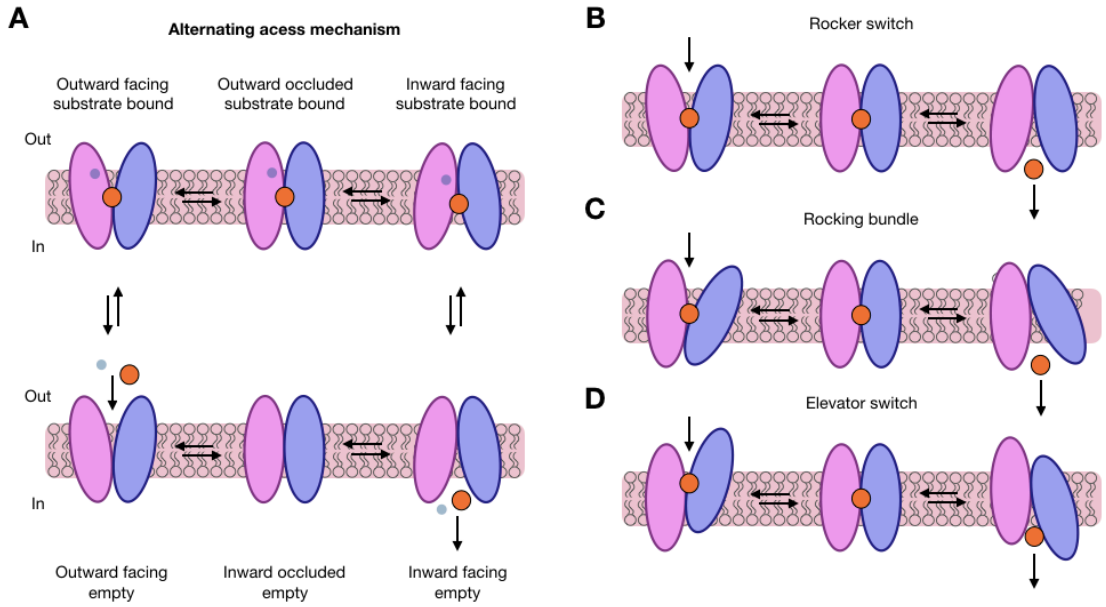

*Figure 8: Schematic representation of an alternating access mechanism during substrate import. **A.** The transporter is accessible to the outward facing side of the membrane in the equilibrium state. Upon binding of the substrate the transporter undergoes a conformational change to outward occluded, before it changes to the inward open state. The substrate can then be released and the transporter changes to the inward occluded state before the cycle starts again. **B.** In the rocker switch mechanism the substrate binds between two domains of the protein. Substrate binding catalyzes the rearrangement of the protein and the domains rock and grant access to the opposite side of the membrane. **C.** The rocking bundle mechanism involves a domain that moves against a more rigid and structurally dissimilar domain in the membrane. **D.** A mobile and an immobile domain are involved in the translocation process in the elevator mechanism. The mobile domain moves against the immobile, rigid domain upon substrate binding and before releasing it at the other side of the membrane.*

It has been the aim of a plethora of investigations to collect and combine the information gathered from crystal structures, single-particle cryogenic electron microscopy (cryo-EM), nuclear magnetic resonance, biophysical, biochemical and computational data to understand the translocation processes of this large variety of transporters. A clearer understanding of the mechanism and structural properties had and will have great impact on the future of pharmacological drug-development in

various fields like the development of novel antimicrobials especially through predictive models for the mechanisms of inhibitor binding.

1.2.2 The drug/metabolite transporter superfamily

The DMT superfamily comprises a large group of membrane transporters found in eukaryotes, archaea and bacteria[173]. This superfamily is subdivided into 14 families that include transporters for a wide range of substrates, metabolites, toxins and drug efflux pumps involved in drug resistances. The assignment to those families is based on phylogeny and the polypeptide chains vary from four transmembrane (TM) segments in the small multidrug resistance (SMR) family, five TM segments in the bacterial/archaeal transporter (BAT) family and in general nine to ten TM segments in the remaining families. It has been shown that the transporting unit of proteins from the SMR or the BAT family consist of a dimer, that is topologically oriented antiparallel towards each other and are expected to be the predecessors of the other family members. The remaining DMT superfamily members are predicted to have a five-TM internal repeat in ten TM helices[174-176]. This characteristic motive of an internal repeat very likely arose from intragenic duplication.

Several transporters from the DMT superfamily have been studied functionally and structurally only recently, revealing the extremely unique topology. The transporters EmrE and Gdx-Clo are members of the SMR family and the available structures exhibit the predicted topology of antiparallel dimers[177-179] (**Figure 9**). During the transport mechanism of the homodimer the proteins swap between the outward open and the inward open conformations[179,180] (**Figure 9 B, D**). Due to the unique topology of an antiparallel homodimeric architecture there is no structural difference between both conformations. In EmrE the substrate tetraphenylphosphonium binds to a glutamate residue in exchange for a proton. The substrate is then transferred to the next residue in exchange for another proton before rearrangements in the helices open an inward facing gate and the substrate dissociates[180] (**Figure 9B**). During the transport cycle in Gdx-Clo the substrate binding site is open to one side, exposing

two conserved glutamates, required for substrate and proton binding[179] (Figure 9D). The published structures suggest a rearrangement upon substrate and proton binding and an opening towards the opposing side for substrate release.

Another member of the DMT superfamily is YddG, an exporter of aromatic amino acids that can be found in *E. coli*, *Starkey novella* and other bacteria[181]. Studies show that the transporter exhibits a broad substrate specificity and expels aromatic amino acids and exogenous toxic compounds in order to maintain its cellular homeostasis[181-183]. The x-ray crystal structure of YddG reveals an outward facing state[181], where the mechanism was proposed based on structural similarities of the inverted repeats to generate a model of an inward-facing state[184,185]. In this mechanism the TM helices TM4 and TM9 are bend and only half way in close contact to cycle between forming a gate towards the extracellular side, or towards the intracellular side[181]. The proposed intermediate state, the occluded state of the cycle, is based on simulations and exhibits both helices in close contact to each other prohibiting access from either side of the membrane.

The structures of three transporter of the nucleotide sugar transporter (NST) family of the DMT superfamily have been studied and elucidated. Those are the triosephosphate/phosphate translocator (TPT) from the thermophilic red algae *Galderia sulphuraria*[186], the CMP-sialic acid transporter (CST) from *Mus musculus*[187] and *Zea mays*[188] and the GDP-mannose transporter Vrg4 from *Saccharomyces cerevisiae*[189,190]. The CST and Vrg4 transporters additionally belong to the SLC35 family of nucleotide sugar transporters[191,192]. The family of SLC transporters are an important group of more than 300 human solute carriers that play important roles during physiological processes, uptake of nutrients and the efflux of drugs or xenobiotics and have been shown to play important roles in various diseases[162-165]. Many drugs target those transporters, which are challenging to study and only a sparse number of structures are published[193,194]. Some of the SLC transporters, i.e. SLC35 and SLC39, exhibit the same topology of 10 TM helices with an inverted repeat of 5 TM helices[173,195]. The family of SLC35 transporters is therefore part of the NST

family of DMT transporters. In fact, not only the NST transporters TPT, CST and Vrg4, but additionally YddG, and both SMR transporters Gdx-Clo and EmrE exhibit similar characteristics as those found in other SLC35 transporters.

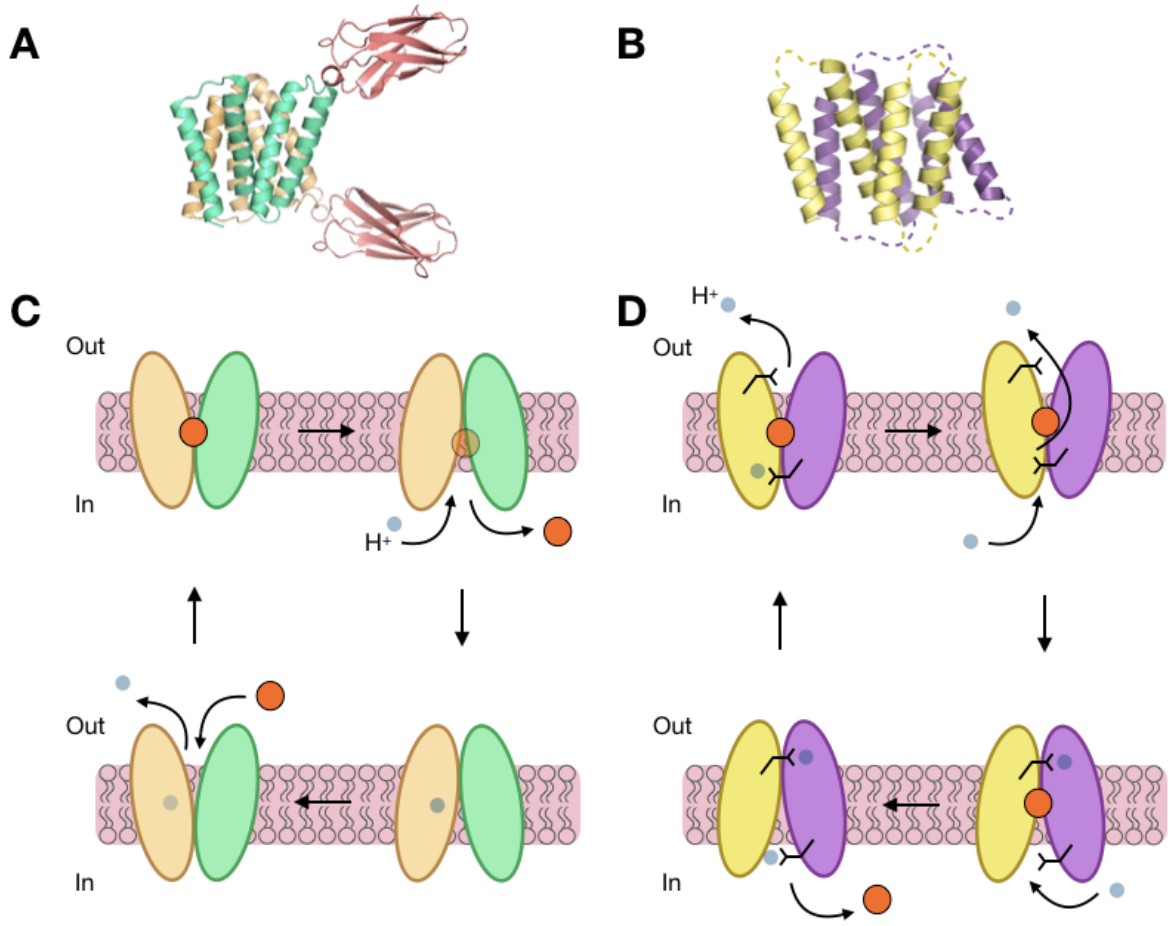

***Figure 9**: Topology and mechanism of Gdx-Clo and EmrE. **A.** Topology of Gdx-Clo (PDB:6WK8) with the inverted repeats colored in beige and green. The monobody is colored in red. **B.** Topology of EmrE (PDB:2I68) **C.** Schematics of the proposed alternating access for substrate import via Gdx-Clo. The substrate is depicted as an orange sphere and protons for coupling as grey spheres. **D.** Schematics of the proposed alternating access for substrate import via EmrE. The substrate is depicted as an orange sphere and protons for coupling as grey spheres.*

TPT is a phosphate translocator that can be found in many photosynthetic eukaryotes[196] or in plastids of other organisms[197]. It belongs to the plastidic phosphate translocator family[198] and is closely related to NST family of the DMT superfamily and to SLC35 transporters[197,199,200]. TPT catalysis the 1:1 antiport of triose-phosphate, 3-

phosphoglycerate and inorganic phosphate[201]. The crystal structures of TPT in the occluded state bound to 3-phosphoglycerate and inorganic phosphate and comparison to other DMT transporters reveals a rocker switch motion of transport[186].

The CST transporter from the SLC35 family transports CMP-sialic acid across the Golgi[187,188]. Crystal structures of CST in complex with CMP and CMP-sialic acid reveal an antiporter rocking-switch mechanism of action, where CMP-sialic acid is exchanged for CMP. Since CST is an antiporter and antiporters are not able to reset themselves to the outward facing state after substrate release[156], it requires the binding of CMP to change from the inward-facing to the outward facing conformation[188].

The GDP-mannose transporter Vrg4 from the SLC35 family imports GDP-mannose into the Golgi lumen and exports GMP[189,190]. The export of GMP happens slower due to its smaller size and lower affinity. Similar to the CST transporter it requires the export of GMP to change its conformation back to the outward facing state. Interestingly the transporter requires short chain lipids for transport and is inactive when surrounded by longer chain lipids[190].

The last DMT transporter of known structure is PfCRT from *Plasmodium falciparum* that causes malaria[202]. PfCRT is known to be involved in drug resistance to antimalarian drugs and is able to export chloroquine and piperaquine, both antimalarian drugs[203]. Only a structure in the apo state bound to an antigen fragment (Fab) was elucidated using single particle cryo-EM. Therefore it was not possible to speculate about the full transport mechanism. The analysis of the electrostatic potential surfaces revealed an electronegative binding cavity, exhibiting the only example of a negatively charged binding cavity compared to the other DMT transporters of known structure.

There is evidence that some members of the DMT superfamily exist as dimers in the membrane[204] and CST and Vrg4 dimers have been observed when reconstituted into monoolein[188,189] (**Figure 10**). The homodimerization of CST is not mediated by lipids[188] whereas Vrg4 reveals a lipid mediated dimer[189]. The Vrg4 transporter has been

observed to be in its monomeric form when purified in detergent and mutation studies reveal that the transporter is able to cycle faster when it is in its dimeric form. It is hypothesized that the reason for a faster cycling is a higher thermal stability of the dimer. Since most structures were solved via crystallization, which would not prove dimerization, it remains to be shown if the homodimerization is present in all DMT transporters and if it is an important characteristic of those.

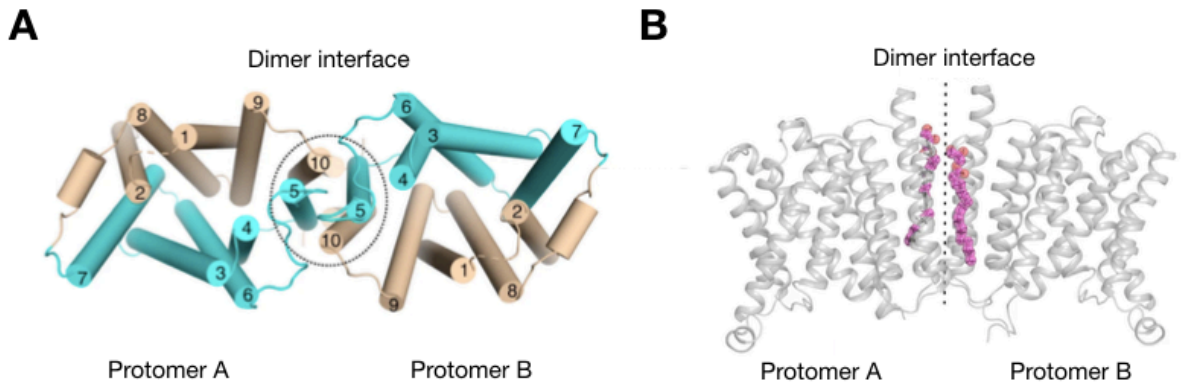

Figure 10: Homodimers of CST and Vrg4. ***A.*** *Homodimer of the CST transporter. The inverted repeats are colored in beige and blue, respectively and the protomers are indicated. Helices 5 and 10 interact at the dimer interface. Figure adapted from Nji et al., 2019.* ***B.*** *Homodimer of Vrg4 transporter. The protomers are indicated and monoolein is shown in pink. Figure adapted from Parker et al., 2019.*

1.3 Selected methods from biophysics and structural biology to study membrane proteins

1.3.1 SSM electrophysiology

Conventional electrophysiological methods like the voltage clamp[205,206] or the patch-clamp[207-210] methods were introduced to study electrogenic transport across membranes. The voltage clamp method measures the ion current through excitable cells[205,206]. The voltage clamp technique, has been further revolutionized with the development of the patch-clamp method[210]. Patch-clamp allows the measurement of individual ion channel currents opposed to collective currents. Initially currents were measured on excitable native cells that exhibit axons or muscle cells but the advances in cloning and the introduction of oocytes to study electrogenic behavior increased opportunities to apply the method on new systems. The oocytes of the African frog *Xenopus laevis* have been proven to be a great expression system for the application of voltage- and patch-clamp methods on ion channels[211] and later on even to study transporters[212,213]. However, the techniques of voltage clamp or patch-clamp are in general not suitable to study bacterial transporters. Bacterial cells are too small for both techniques and the expression of bacterial transporters in mammalian cells is difficult. This limitations do not apply for solid-supported membrane (SSM)-electrophysiology which has been proven to be a powerful technique to measure electrogenic transport[214]. The method is suitable for many transporters that are difficult to study under conventional electrophysiological conditions. SSM electrophysiology is applicable on protein samples reconstituted into liposomes, crude membranes or membrane vesicles from cell lines or any membrane preparation with the protein of interest. The method of SSM is based on the black lipid membrane (BLM) technique. The BLM is a planar membrane onto which a membrane fraction containing a transporter is adsorbed. The measurement is achieved via capacitive coupling[215]. The planar bilayer sits between two compartments that are connected via electrodes with a variable voltage source. The demand for

concentration jumps between both compartments has led to the development of a more stable technique for this application the SSM based electrophysiology. The advantages of SSM compared to BLM are a higher membrane stability and with that a much faster solution exchange is applicable without disturbances. Additionally, the sensor size is up to 3 mm in diameter and can be coated with the membrane preparation containing the protein of interest. With the large sensor size, the signal amplitude is much larger compared to whole-cell patch-clamp[216]. SSM requires fewer protein, has a better signal-to-noise ratio (SNR) and a higher sensitivity compared to patch-clamp.

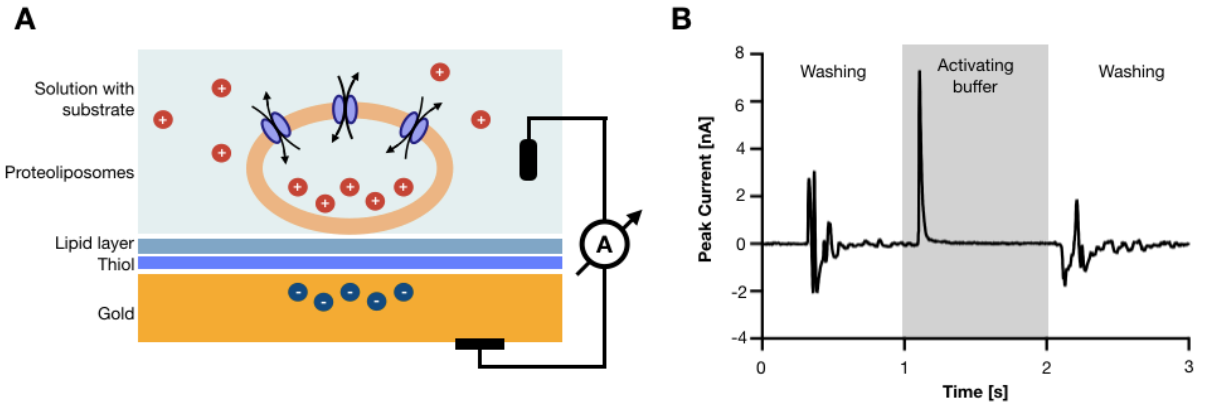

Figure 11: Experimental setup of SSM electrophysiology on transport proteins. ***A.*** *Proteoliposomes are adsorbed on the gold layer of the SSM chip and form a capacitively coupled system for the measurement of charge displacement.* ***B.*** *Current trace for a typical SSM measurement. A rapid solute exchange allows the measurement of current as a function of time.*

The SSM sensor chip consists of a gold sensor electrode and an alkyl-mercaptan monolayer[214,217]. The SSM forms spontaneously upon addition of a lipid mixture and a subsequent rinsing with a buffer. The membrane preparation is added on top of the SSM, which, on top of the sensor chip, performs as a measuring electrode and forms a capacitively coupled system (Figure 11A). The measurements are performed in a Faraday cage and the sensor is connected to a fluidic system. The membrane fraction with the protein of interest is adsorbed on the SSM layer on the gold surface of the chip and the transport activity is measured upon fast solution exchange to a buffer containing the electrogenic substrate (Figure 11B). Although the measured

current is not in a steady-state, the peak current amplitude in SSM electrophysiology is proportional to the turnover rate and allows the calculation of half saturation constants like the EC_{50}, inhibitory constant IC_{50}, Michaelis-Menten constant K_m or the dissociation constant K_D[214,218]. Further analysis of the signal rise and its decay can give additional information about the kinetics in the shape of rate constants. Additionally, to the measurement of the substrate turnover, alternative substrates, inhibition, pH and salt dependence can be measured.

1.3.2 Principles of x-ray crystallography techniques for membrane proteins

The elucidation of protein structures through x-ray crystallography has been the most favored technique throughout the years since the first published structures of myoglobin[219] and lysozyme[220,221]. X-ray crystallography together with nuclear magnetic resonance and single particle cryo-EM provide a platform for the understanding of structure related functions and help in structure based drug design[222]. Membrane proteins have been shown to be rather challenging to study, due to less yield, lower stability and a difficult handling but X-ray crystallography remains nonetheless the leading technique to solve three dimensional (3D) structures with a contribution of up to 80% even for membrane proteins[223]. Cryo-EM is catching up with nearly the same number of published membrane proteins structures per year compared to other methods[223].

One of the first steps for a successful crystallization is the expression and purification of homogenous membrane proteins. Different host cell systems are available for the protein expression, depending on the source of the protein of interest and necessary post-translational modifications, i.e. expression of prokaryotic or eukaryotic proteins. Furthermore, to delipidate and extract the membrane protein from its native membrane, it is crucial to select a suitable lipid substitute. Since the membrane consists of phospholipids with a hydrophobic tail and a hydrophilic head, a chemical with the same amphiphilic characteristic is required and detergents have proven to be useful for not only the extraction of the protein from the membrane but also for

keeping it stable in solution. Depending on the charge of their head group they can be divided into three groups: ionic, nonionic and zwitterionic detergents[224,225]. Ionic detergents have a great efficiency in the extraction of membrane proteins from the membrane, however they are prone to denaturing effects on membrane proteins and their use has become limited[224]. The most popular group of detergents is the nonionic group. Those are usually milder and exhibit a nondisruptive nature[226]. They are additionally the most widely used group of detergents for the crystallization of membrane proteins[226]. Zwitterionic detergents carry positive and negative charges in the polar head and have a zero net charge[224]. Those are not as mild as nonionic detergents but rather lie between the ionic and nonionic effects of harshness and have been successfully used for crystallisation[226].

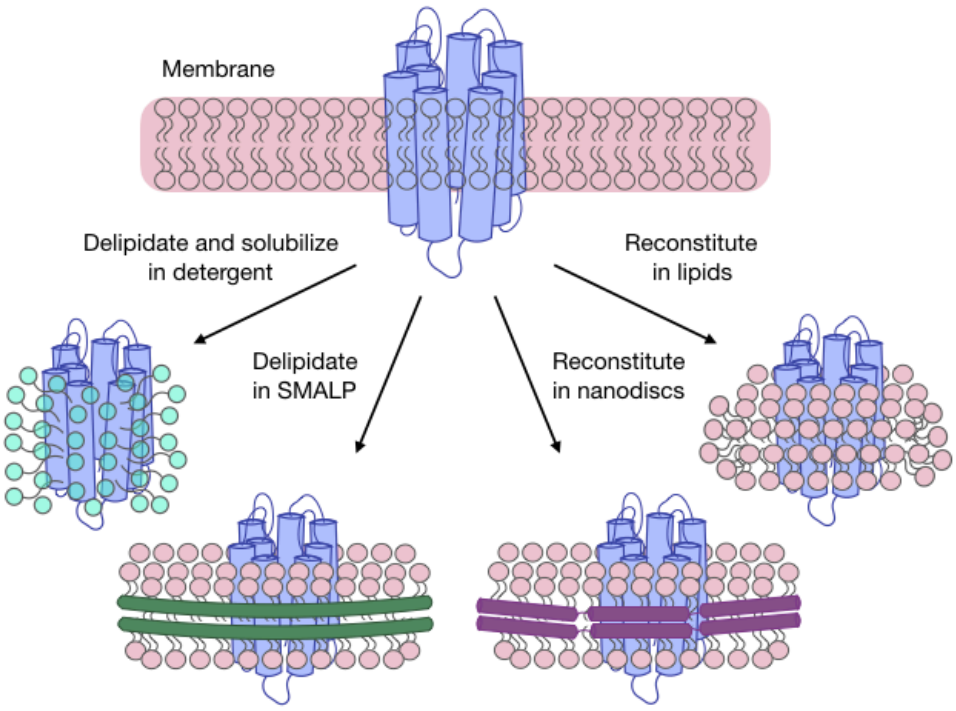

Figure 12: Schematics of membrane proteins in membrane scaffolds. Membrane proteins are extracted from the lipid membrane. The lipidic environment can be replaced by detergents that mimics the characteristics of lipids or it can be replaces by membrane scaffolds, like nanodiscs or SMALPs. Nanodiscs and SMALPs contain lipids and provide a close to native environment.

An alternative platform for the stabilization of membrane proteins are membrane mimetic systems (Figure 12). Those can be nanodiscs or styrene malic acid lipid particles (SMALPs). Nanodiscs consist of membrane scaffold proteins (MSPs), which

is a genetically engineered variant of the human serum apolipoprotein-A[227]. To get a membrane protein reconstituted into nanodiscs, one mixes the membrane protein solubilized in detergent with MSP and phospholipids. The self-assembly of nanodiscs happens spontaneously during the removal of detergent via biobeads or dialysis[228]. Not as popular but using the same principles are the SMALPs, but in contrast to nanodiscs they contain native membranes from the proteins[229].

There have been successes in the crystallization of membrane proteins using nanodiscs[230] and SMALPs[231] but it remains challenging and the main platform for those techniques stays single-particle cryo-EM[232-234]. Detergent solubilized membrane proteins remain widely used for x-ray crystallography. The main difficulty in crystallizing membrane proteins is that the detergent or the membrane mimetic structures cover the hydrophobic part of the protein and in many cases, this only leaves a very small surface area for the formation of crystal contacts. Those small surfaces sometimes consist of very flexible regions or loops, which can be either digested or truncated. The pitfall of using loop truncations is that the crystalized protein is not a native full-length representation of the membrane integrated protein of interest. Another hurdle can be the presence of protein-free micelles which reduce the success rate of crystallization through the disruption of protein-protein interactions which is important for crystal contacts. Membrane proteins in detergent also exhibit a higher rate of crystallographic defects, anisotropy and twinning.

The main technique for crystallizing membrane proteins, as for soluble proteins in general, is vapor diffusion. After screening for optimal conditions of purity and stability of the membrane protein, the sample is concentrated up to its aggregation threshold (this can be monitored using e.g. dynamic light scattering) but approximately 10 mg/ml can be generally used as a rule of thumb[235,236]. There are the sitting drop and the hanging drop methods for vapor diffusion (Figure 13A). For the sitting drop, the pure and concentrated protein is mixed with the solution from the screen that is also present in the reservoir and a drop is set in a sealed environment. In the hanging drop method, the drop is placed on top of the cover slide.

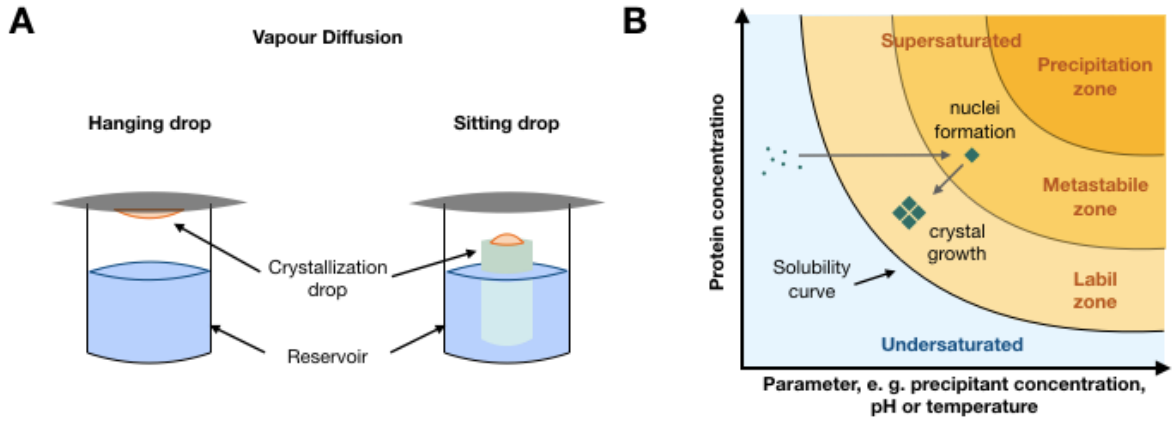

*Figure 13: Crystallization methods and phase diagram. **A.** Vapor diffusion crystallization. The purified membrane protein in detergent is mixed with the crystallization buffer that is contained in the reservoir. The protein-buffer mixture is used to set up drops by either using the hanging drop method or the sitting drop method. **B.** Schematics of a typical phase diagram for the crystallization of proteins as a function of protein and a precipitant concentration, e.g. salt concentration. The diagram is divided into a region of undersaturation and a region of supersaturation. The solubility curve describes the equilibrium between the solid phase and the liquid phase with free molecules. Nucleation can arise in the region of supersaturation and crystals grow closer to the solubility curve in the supersaturation region.*

The symmetrical composition that is found in a crystal lattice is not a preferred composition of proteins and needs to be induced artificially. The protein needs to transition from a completely disordered state into an ordered one. During that critical transitional stage the first ordered assemblies are formed that allow the nucleation of macromolecular protein crystals. The point of nucleation is a critical non-equilibrium state of supersaturation (Figure 13B). The state of supersaturation is unique for each system and protein and is reached through the addition of a precipitant, which can be a neutral salt, a polymer or, more commonly, polyethylene glycol (PEG), available at different sizes. During that state nuclei form spontaneously and the growth of the actual crystal can start. During the vapor diffusion technique, the drop mixture with the protein has a lower reagent concentration and water vapor leaves the drop to reach equilibrium. During that exchange the drop exhibits increasing concentration and undergoes supersaturation. The initial screen is usually carried out using the sitting drop method and commercially available screens that cover a variety of

crystallization conditions specifically prepared after collecting data from successful crystallization compositions for membrane proteins[237-239]. After the identification of the initial hit, a subsequent screen is prepared using a composition around it by varying the pH, salt and PEG concentrations.

Specifically for the crystallization of membrane proteins and to overcome the problems of crystallization using detergents, *in meso* crystallography was developed[240,241]. For *in meso* crystallography, neutral lipid molecules, mostly monoacylglycerols like monoolein, are mixed with the detergent solubilized protein. The mesophase, or also called lipidic cubic phase (LCP), forms spontaneously and forms a bicontinuous LCP bilayer. Through the addition of precipitants the proteins are migrating into lamellar domains to form crystals.

Another very useful tool for the crystallization of membrane proteins are specific binders used as crystallization chaperones, that increase the surface area of proteins which can participate in forming crystal contacts. Such binders are usually soluble proteins and can be T4 lysozymes, Fab fragments[242,243], nanobodies[244,245] or synthetic nanobodies[246] (Figure 14).

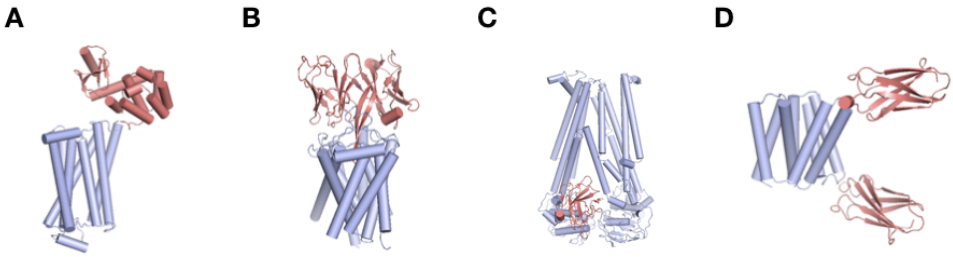

***Figure 14**: Representation of scaffold chaperones for membrane protein structure elucidation. **A.** Crystal structure of G protein-coupled receptor with T4 lysozym (PDB:2RH1). **B.** Single particle cryo-EM structure of Fab-bound PfCRT (PDB:6UKJ). **C.** Crystal structure of nanobody bound receptor (PDB:5NBD). **D.** Crystal structure of Gdx-Clo transporter bound to a monobody (PDB:6WK9).*

There are many methods for the crystallization of membrane proteins, but the physical principles of x-ray crystallography stay the same for all methods and are based on the properties of crystals and their diffraction using an x-ray beam. The protein crystal consists of a symmetrical lattice formed by identical copies of the protein in a regular

and repeated pattern (Figure 15A). The unit cell is the smallest repeating unit and can be described in 3D by the lengths of the three axes *a*, *b*, *c* and angles *α*, *β*, *γ*.

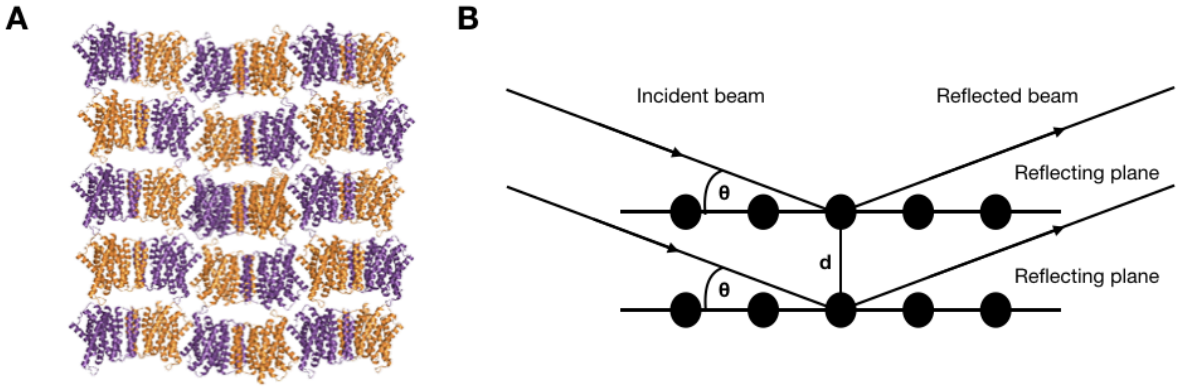

Figure 15: Protein lattice and Bragg diffraction. ***A.*** *Crystal packing of a membrane protein (TPT, PDB:5Y78).* ***B.*** *Schematics of x-ray reflection from a crystal lattice plane based on Bragg's law.*

When x-rays hit atoms, they are scattered by the electrons in the atoms. A diffraction pattern is created on a detector by either constructive or destructive interferences of the scattered x-ray waves. A constructive interference happens when the atoms are ordered periodically, as is the case in a crystal and occurs only if the crystals are in planar layers with distance *d* (Figure 15B) and constructive interference appears if it satisfies the Bragg diffraction conditions, derived from Pythagoras theorem, where *n* is the order of reflection, *θ* is the angle of the deflected beam[247]:

$$2d\ sin\theta = n\lambda \qquad \text{(Equation 1)}$$

The diffraction pattern that is visible on the detector is a representation of the reciprocal lattice of the crystal, described by the miller indices *h, k, l.* The diffraction pattern describes the electron density in reciprocal space, where the electron density *ρ(X)* of the crystallized protein can be described in terms of a Fourier integral:

$$\rho(\mathbf{X}) = \int F(h,k,l)\, e^{2\pi i \mathbf{X}\cdot(h,k,l)}\, dV \qquad \text{(Equation 2)}$$

Where $\mathbf{X}$ are the reciprocal coordinates and $e^{2\pi i \mathbf{X}\cdot(h,k,l)}$ the phase of the scattered wave. The electron density is related to the structure factor *F(s)* through the inverse Fourier transform:

$$F(h,k,l) = \int \rho(\mathbf{X}) e^{-2\pi i \mathbf{X}\cdot(h,k,l)}\, dx \qquad \text{(Equation 3)}$$

The structure factor describes the amplitudes and phases of the reflections, where the amplitudes can be derived from the intensities of the scattered diffraction pattern. However, the phase information of the structure factor is lost during the scattering experiment but necessary in order to calculate the electron density map and to determine the structure. This problem is called the phase problem in x-ray crystallography and needs to be guessed though an *a priori* known structure from, e.g. a homolog model for the method of molecular replacement, which is carried out *in silico*, or by solving the phase problem experimentally by selenomethionine-replacement or heavy-atom derivatization. From the electron density at atomic resolution higher than 2 Å it is possible to build the backbone and the residues of the protein *de novo*.

1.3.3 Principles of single particle cryo-EM on membrane proteins

With recent and ongoing advances in single-particles cryo-EM, it has become possible to elucidate structures of proteins that are too heterogeneous or flexible[248] and those that cannot easily crystallize[249]. Limitations of single particle cryo-EM are constantly improving and novel methods are being developed to study challenging proteins, complexes and proteins of molecular sizes below the resolution limit for cryo-EM[223,250,251]. Especially the structural elucidation of membrane proteins has benefitted from the advances in the field and can be seen in an increasing number of published structures for membrane proteins per year[223]. The irradiation with electrons produces two dimensional (2D) projections of the protein (particle) at different views[252]. Single particle cryo-EM allows a 3D reconstruction of the protein structure from those 2D projections. The advantages of single particle cryo-EM compared to other techniques are that it requires less protein sample, the protein is flash frozen in a buffer of choice at close to native conditions, it requires no crystallization and there is no phase problem that needs to be solved. This method allows the study of membrane proteins or complexes in detergent[223,253], embedded in membrane mimetics like nanodiscs[254] or bound to scaffolds, like nanobodies[255],

synthetic nanobodies (sybodies)[246,256], megabodies[257], Fab fragments[258,259] or DARPins[260], to either decrease homogeneity and trap a specific state or to enlarge the particle size if the protein of interest is below the resolution limit.

Transmission electron microscopy has been developed for physics and material sciences but it has become very popular to solve structures of biological macromolecules when energy-filtered and operated at lower dose of electron irradiation[261]. As for x-ray crystallography, a highly pure protein sample is required and the concentration needs to be optimized for each protein and preparation method individually[262]. For the investigation via electron microscopy the sample can be either embedded in a heavy atom stain like uranyl acetate[263] or be vitrified in amorphous ice through flash freezing in liquid ethane[264]. Both techniques require glow-discharged grids[265,266], which the protein sample is applied on for support. Glow-discharging the grid prior to application is important for the removal of adsorbents like water and to make the grid hydrophilic, to allow an even spread of an aqueous solution. The staining technique is called negative staining and the observed images from those samples are the negatives of the specimen[267,268]. Although the negatively stained sample can be irradiated with a higher electron dose and operated at room temperature, the resolution is limited due to the grain size of the staining agent to approximately 20 Å[252]. For such resolutions it is sufficient to use electron microscopes operating at 120 kV. The vitrification in amorphous ice decreases the effect of radiation damage[269] and flash freezing prevents the formation of ice crystals, which would produce artefacts in the acquired image[264]. Additionally, it is not limited to a low resolution as in negative staining. The electron microscope needs a higher voltage up to 300 kV and is operated at liquid nitrogen temperatures. With cryogenic samples it is possible to reach higher resolution with atomic resolution below 2 Å[270,271].

The main components of an electron microscope are the electron source, lenses in the form of magnetic coils, a sample holder and a detector[272] (Figure 16A). The most widely used electron source is a field emission gun[273] that emits electrons from a

tungsten tip when a high electric field is applied[274,275]. The lens system consists of a condenser lens, just below the electron source, an objective lens, which sits below the sample holder and forms the initial image and a projector lens that magnifies the image before the electrons hit the detector[252]. An aperture sits between the objective and projector lenses and stops electrons that are scattered wide, to increase the image contrast.

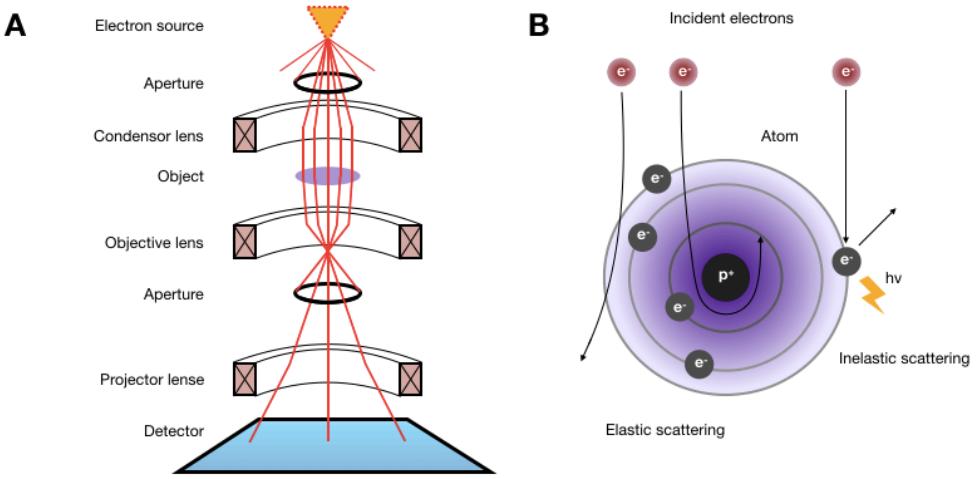

*Figure 16: Schematic representation of the lens system in an electron microscope and electron scattering. **A.** Schematics of the lens system with an electron source emitting electrons that are accelerated and cross several apertures, lenses and the object before their detection. **B.** Schematics of possible electron interactions with atoms when passing an object. Electrons can pass the sample without interactions, they can scatter elastically or inelastically.*

While charge coupled devices are sufficient for the use of negatively stained specimen and provide increased low-frequency contrast[276,277], it is crucial to use very sensitive and precise detectors for single particle cryo-EM[278]. Direct detection device (DDD) detectors fulfil the requirements with a higher detective quantum efficiency and an improved SNR[278,279]. Those DDD detectors come closer to the theoretical resolution limit of the Nyquist frequency[280,281], where the Nyquist limit is the maximum detectable resolution which is limited to twice the pixel size of the detector[252]. Additionally, those detectors are used to record movies of the irradiated sample on a grid.

Charged electrons unfortunately induce a movement of the grid and the ice and decrease the image contrast[282]. This charged induced movement can be corrected

for, if separate frames are recorded across the total dose of irradiation, which is usually aimed at around 20-50 $e^-/Å^2$. Special movie alignment algorithms can correct for the dose induced movement between the recorded movie frames and additionally weight each frame[283,284], depending on the available information. The weighting is important because the first frames experience larger movements and the latter frames exhibit less information due to irradiation damage[282], where covalent bonds can be broken and side chains or residues can be missing.

When electrons hit atoms in the sample they can be either scattered elastically, without any energy loss, inelastically, where energy from the electron is transferred to an atom in the sample or they can pass without any deflection[252] (Figure 16B). The electrons form an image at the detector that corresponds to a 2D projection of the 3D object. The inelastically scattered electrons exhibit a phase shift that contributes to the phase contrast of the final image at the detector, whereas the inelastically scattered electrons that don't reach the detector contribute to the amplitude contrast. However, biological samples are weak phase objects with very low contrast as they are mostly composed of H, C, O and N atoms that interact weakly with electrons. Therefore, it is important to collect as many images of the particles as possible in order to average them out and increase the information. Additionally, to the low contrast there are other factors that decrease the information. Since the microscope lenses system is not ideal it exhibits spherical, astigmatic and chromatic aberrations[272]. The observed image contrast $\psi_{observed}(\mathbf{x})$ is therefore a convolution of the ideal object image $\psi_{ideal}(\mathbf{x})$ with the so called point spread function $PSF(\mathbf{x})$:

$$\psi_{observed}(\mathbf{x}) = \psi_{ideal}(\mathbf{x}) \otimes PSF(\mathbf{x}) \qquad \text{(Equation 4)}$$

The Fourier transform of the image contrast is:

$$F[\psi_{observed}(\mathbf{x})] = F[\psi_{ideal}(\mathbf{x})] \cdot CTF(k) \cdot E(k) \qquad \text{(Equation 5)}$$

The contrast transfer function $CTF(k)$ describes the aberration and $E(k)$ is the envelope function that describes spatial and temporal aberrations[252,275]. The $CTF(k)$ depends on the wavelength of the electrons λ, the defocus Δz, the spherical aberration C_s and the spatial frequency k:

$$CTF(k) = sin\left[\frac{2\pi}{\lambda}\left(\frac{Cs\,\lambda^4 k^4}{4} - \frac{\Delta z\,\lambda^2\,k^2}{2}\right)\right] \qquad \text{(Equation 6)}$$

The envelope function, with B being the experimental B-factor[285] is:

$$E(k) = e^{-Bk2} \qquad \text{(Equation 7)}$$

The phase and the amplitude both contribute to the contrast of the gained images and the CTF describes the spatial frequencies of the transmitted information[286,287]. Defocussing of the objective lens increases the phase contrast and with it the overall contrast, of a thin layer of a biological sample of light atoms[286,288]. The Fourier transform of the power spectrum of the image reveals so called Thon rings, that determine the minima, maxima and zero crossings of the CTF[286] (**Figure 17**). Correction for the CTF, and therefore the correction for aberration of the microscope, can be carried out by various available algorithms and increases the quality of the available information in the image, called micrograph, and therefore lead to a higher resolution in the final density map[288,289].

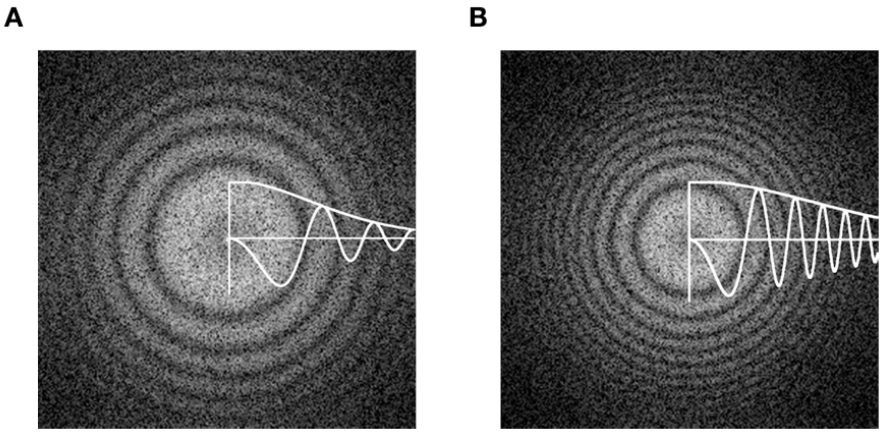

***Figure 17**: Thon rings and CTF at different defoci. Two exemplary power spectra from two micrographs obtained at different defoci, without astigmatism and showing centrosymmetric Thon rings. The corresponding CTF curves are overlayed. CTF curves oscillate between positive and negative contrast with cero-crossing. **A.** Micrographs image obtained at 0.5 µm defocus. **B.** Micrographs image obtained at 1 µm defocus. Image adapted from Orlova et al., 2011*

After processing the micrographs by correcting for the beam induced movement and the CTF, the coordinates of the center of the particles are selected either manually or automatically from each micrograph and extracted using a smaller size to reduce computational resources[252,290,291]. During the 2D classification many projections of the same view of the protein are grouped together and averaged to increase the

information from each individual particle, which on their own do not contain enough contrast and information. The approaches for the 2D classification use the maximum likelihood, where individual particles can be assigned to different classes and the assignment is weighted[292,293]. The 2D classification is important to reduce false positives and to reduce heterogeneity in terms of particle size if empty micelles, empty nanodiscs or other impurities are present in the sample. The 3D reconstruction can then be carried out with a clean set of particles from selected classes[252,290,291]. It is crucial for a successful 3D reconstruction to have particles and particle classes covering all possible angular orientations. The bottleneck for this can be preferred orientation of the protein at the air-water interface[294] or just not enough quantity of particles. The latter can be solved by increasing the recorded dataset, whereas the first issue is challenging to tackle. This can be overcome by increasing the ice thickness, the addition of detergents or tilting the grid during data collection[294,295].

The reconstruction of the 3D object is carried out in Fourier space and the first step of the 3D reconstruction is the determination of the orientation of the particles, which is determined by calculating the cross-correlation values[252,296]. The map can then be calculated from the determined angular parameters using maximum-likelihood and a Bayesian approach to determine the structure[290,291,297]. An initial map of a homologous protein can be used for the 3D reconstruction, but prior knowledge is not always available and this method is prone to biases if a wrong map[298] or a wrong handedness[299,300] is used. Another approach is the *ab initio* 3D reconstruction which can lead to the determination of a density map of different conformations if those are present in the particle set[291]. To ensure that the calculated maps are not computed due to initial map bias or other biases, the dataset is split into two random, independent halves, which are treated individually and compared via cross-correlation over a spatial frequency shell called Fourier shell correlation (FSC) after each iteration step until the density map converges[252,301]. To compute the resolution of the obtained map, a refinement is carried out subsequently and the quality of the map can be described through a threshold FSC value of 0.143, which has become

the gold-standard for map evaluation[300,302]. The threshold value has been chosen empirically through a systematic comparison of structural features from EM density maps and electron density maps from x-ray crystallography of the same protein structure.

Similar techniques as in x-ray crystallography can be applied for the structural elucidation of membrane proteins. The alignment and evaluation of proteins that have a molecular size below 120 kDa, if they are mostly embedded in a detergent belt or nanodiscs or those that are very flexible with high conformational heterogeneity, is difficult due to the lack of rigid structural features for an unambiguous determination. Therefore nanobody[255], sybody[246] or Fab fragment[303] bound protein samples are generated to overcome size limitations or very flexible features. The issue of flexible regions can additionally be addressed computationally through the masking of protein regions during the data processing[304-306].

Membrane proteins make up to more than 60% of current drug targets[307], but for most of them there is no detailed knowledge about their structure and mechanism of inhibition available[223]. By increasing our understanding about membrane proteins, we can establish a platform for future drug-design and help to increase the structural database for computer aided structure prediction and drug-design[308-310].

2 Aim of the study

The aim of this work was to elucidate and study the structure, function and mechanism of the essential pneumococcal choline importer LicB. There was not much known about this transporter from the DMT superfamily, except that it supposedly imports choline and the deletion of its gene is lethal for *S. pneumoniae*. The aim of the study was to provide insight about the mechanism of the transporter, its potential as a novel drug-target and its capability of inhibition. Additionally, it was important to provides a broader context for the DMT superfamily, which includes some SLC family members, beyond the knowledge about the NST-type transporters from the same superfamily. The study can be split into the following steps:

The first step of the study was to over-express a recombinant copy of the pneumococcal LicB in a suitable bacterial vector, to extract and purify stable and natively folded LicB for *in vitro* studies. A pure and stable protein in detergent was crucial for all follow-up experiments. In general, it is possible to carry out structural and functional experiments using only the detergent solubilized protein, but it was crucial to reconstitute the protein in lipids and nanodiscs, respectively in order to provide close to native conditions. The second step was to investigate the function of the transporter using SSM-electrophysiology, to look at the transport of the substrate, of similar bioavailable compounds and inhibitors. Furthermore, it was required to identify the energy source for the transport and its coupling ions. The third step was the structural elucidation of LicB in different states to identify the binding pocket and predict the mechanism. X-ray crystallography and cryo-EM were both suitable methods allowing different approaches, e.g. variations of detergents, in LCP, using nanodiscs and crystallization scaffolds. The fourth step was to identify compounds for the inhibition of choline import. Sybodies not only perform well as crystallization scaffolds and for the trapping of different conformational states but can act as potential inhibitors.

3 Results

The doctoral thesis is based on two peer-reviewed publications and a book chapter:

3.1 **Bärland, N.**, Rueff, A. S., Cebrero, G., Hutter, C. A., Seeger, M., Veening, J. W., & Perez, C. (2021). Mechanistic basis of choline import involved in teichoic acids and lipopolysaccharide modification. *Accepted, Science Advances. BioRxiv preprint: doi: https://doi.org/10.1101/2021.09.14.460277*

3.2 **Bärland, N.**, & Perez, C. (2021). Selection of Transporter-Targeted Inhibitory Nanobodies by Solid-Supported-Membrane (SSM)-Based Electrophysiology. *Journal of Visualized Experiments: Jove*, (171). *doi: https://dx.doi.org/10.3791/62578*

3.3 **Bärland, N.**, & Perez, C. (2020). Fast Small-Scale Membrane Protein Purification and Grid Preparation for Single-Particle Electron Microscopy. In *Expression, Purification, and Structural Biology of Membrane Proteins* (pp. 275-282). Humana, New York, NY. *doi: https://doi.org/10.1007/978-1-0716-0373-4_18*

3.1 Mechanistic basis of choline import involved in teichoic acids and lipopolysaccharide modification

Natalie Bärland[1], Anne-Stephanie Rueff[2], Gonzalo Cebrero[1], Cedric A.J. Hutter[3,4], Markus A. Seeger[3], Jan-Willem Veening[2], Camilo Perez[1]

[1] Biozentrum, University of Basel, 4056 Basel, Switzerland

[2] Department of Fundamental Microbiology, Faculty of Biology and Medicine, University of Lausanne, 1015 Lausanne, Switzerland.

[3] Institute of Medical Microbiology, University of Zurich, Zurich, Switzerland

[4] Current address: Linkster Therapeutics AG

Contribution Natalie Bärland: Expression, purification of LicB and sybodies, crystallization experiments, reconstitution (lipids, nanodiscs), functional assays (SSM-electrophysiology, transport assay), WTA and LTA extraction, docking, data acquisition, analysis and interpretation, drafting of manuscript. Contribution to study design, mutagenesis, sample preparation for cryo-EM, processing of X-ray and cryo-EM data, building and validating models.

Journal: BioRxiv preprint, accepted Science Advances.

Mechanistic basis of choline import involved in teichoic acids and lipopolysaccharide modification

Natalie Bärland[1], Anne-Stéphanie Rueff[2], Gonzalo Cebrero[1], Cedric A.J. Hutter[3,4], Markus A. Seeger[3], Jan-Willem Veening[2], Camilo Perez[1*]

[1]Biozentrum, University of Basel, 4056 Basel, Switzerland

[2]Department of Fundamental Microbiology, Faculty of Biology and Medicine, University of Lausanne, 1015 Lausanne, Switzerland.

[3]Institute of Medical Microbiology, University of Zurich, Zurich, Switzerland

[4]Current address: Linkster Therapeutics AG

[*]Correspondence to: Camilo Perez at camilo.perez@unibas.ch

Phosphocholine molecules decorating bacterial cell wall teichoic acids and outer-membrane lipopolysaccharide have significant roles in adhesion to host cells, immune evasion, and persistence. Bacteria carrying the operon that performs phosphocholine decoration, synthesize phosphocholine after uptake of the choline precursor by LicB, a conserved transporter among divergent species. *Streptococcus pneumoniae* is a prominent pathogen where phosphocholine decoration plays a fundamental role in virulence. Here we present cryo-electron microscopy and crystal structures of *S. pneumoniae* LicB, revealing distinct conformational states and describing architectural and mechanistic elements essential to choline import. Together with *in vitro* and *in vivo* functional characterization, we found that LicB displays proton-coupled import activity and promiscuous selectivity involved in adaptation to choline deprivation conditions, and describe LicB inhibition by synthetic nanobodies (sybodies) and hemicholinium-3. Our results provide novel insights into the molecular mechanism of a key transporter involved in bacterial pathogenesis and establish a basis for inhibition of the phosphocholine modification pathway across bacterial phyla.

Teichoic acids (TA) are fundamental biopolymers that make part of the cell wall of Gram-positive bacteria (*1-3*), whereas lipopolysaccharides (LPS) are exclusively found at the outer membrane of Gram-negatives (*4-6*). Although their compositions differ, both TA and LPS function as endotoxins in bacterial pathogens, participate in immune evasion, prevent recognition and opsonization by antibodies, and play important roles in adhesion and colonization (*7, 8*). Decoration of TA and LPS with phosphocholine moieties is among the most impactful cell wall modifications, conferring virulence advantages to multiple pathogens (*9-11*). Gram-positive *Streptococcus pneumoniae* and Gram-negative *Haemophilus influenzae*, both residing in the human respiratory tract, are well characterized pathogens that expose phosphocholine epitopes on their cell surface (*12, 13*). Interactions of phosphocholine with host proteins, such as the platelet activating factor receptor (*14-16*), allow adhesion to the surface of host cells followed by cell invasion (*17, 18*). In addition, *S. pneumoniae* and commensal streptococci use phosphocholine decorated TA as a platform that anchors a great variety of choline binding proteins, which contribute to adherence, colonization and virulence (*19-26*).

Bacteria generally import choline from the extracellular milieu and use it for osmoregulation (*27, 28*). However, some bacteria import choline exclusively for modification of TA or LPS (*10, 29, 30*). The important function of this modification leads to choline auxotrophy in *S. pneumoniae* (*31*), although this pathogen can increase the available extracellular natural pool of choline by processing host phospholipids via surface exposed or secreted phosphodiesterases (*32, 33*). Thus, choline

import catalysed by LicB, is an essential trait of pathogens like *S. pneumoniae* (**Fig. 1A**) (*31, 34-37*). LicB is a 32-kDa protein, member of the drug/metabolite transporters (DMT) superfamily, which consists of 14 transporter families, harbouring more than 300 membrane proteins ubiquitously distributed in eukaryotes, bacteria and archaea (*38*). Members of this superfamily display 4 to 10 transmembrane (TM) helices, and are derived from primitive proteins of 4 TM helices similar to EmrE, a member of the small multidrug resistance (SMR) family (*39*).

The *licB* gene is located in the *lic* operon which encodes the protein machinery that converts choline into phosphocholine and that decorates TA and LPS (*34, 36, 40*). Inactivation of the *licB* gene leads to non-viable *S. pneumoniae* (*31*), whereas in *H. influenzae* leads to choline uptake deficiency under human nasal airway conditions (*34*). Genes from the *lic* operon can be found in multiple other Gram-positive and Gram-negative bacterial species where phosphocholine decoration of TA, LPS, or other structures occur (*35*). A sequence-similarity network showing *licB* genes sharing high sequence identity (>40%) among different bacterial phyla, demonstrates the important role of this transporter in phosphocholine decoration across Gram-positive and Gram-negative bacteria (**Fig. 1B and Fig. S1**). Despite its clear relevance and potential as drug target, there are no structural or functional studies aiming to characterize the mechanism of LicB or that provide clues on how to inhibit its function.

To elucidate mechanistic elements essential to LicB function, we determined apo-outward-open and choline-bound-occluded structures of *S. pneumoniae* LicB solved by cryo-electron microscopy (cryo-EM) and X-ray crystallography, and performed *in vitro* assays in proteoliposomes and in *S. pneumoniae* cells. We demonstrate that LicB displays promiscuous selectivity involved in adaptation to choline deprivation conditions, and describe architectural elements conserved among divergent bacterial phyla essential for choline binding and proton-coupled import activity. In addition, we describe inhibition of LicB by synthetic nanobodies (sybodies) and hemicholinium-3, thereby establishing the basis for selective inhibition of the phosphocholine decoration pathway.

Results

S. pneumoniae LicB is a promiscuous high-affinity choline transporter

We characterized the transport activity of LicB reconstituted in proteoliposomes using solid supported membrane (SSM) electrophysiology (*41*) (**Fig. 2A,B**). Transport of choline is electrogenic, as evidenced by a positive current consistent with transport of the positively charged choline into proteoliposomes (**Fig. 2A**). The amplitude of the current measured before reaching electrochemical equilibrium, evidenced by the rapid current decay, is proportional to the initial rate of choline transport. Using this assay, we determined that LicB displays an EC_{50} (apparent K_M) for

choline of 47 ± 15 μM (**Fig. 2B**). In contrast, protein-free liposomes exhibit no transport of choline (**Fig. 2A**). We tested whether LicB can transport alternative compounds with choline-like characteristics. Activation by arsenocholine, a natural compound with a similar composition to choline but containing arsenic instead of nitrogen (*42*), can be transported by LicB as evidenced by positive currents arising from transport into proteoliposomes (**Fig. S2A**). LicB displays lower transport affinity for arsenocholine (EC_{50} = 170 ± 9 μM) (**Fig. 2B**), likely due to the larger radius of the positively charged trimethyl-arsonium group. These results recapitulate prior observations of arsenocholine transport by a choline-transporting variant of the betaine symporter BetP (*43*), and by the choline and betaine transporters OpuB and OpuC, respectively (*44*). In addition, acetylcholine, a positively charged molecule that in contrast to choline carries an ester acetyl instead of a hydroxyl group, is also transported by LicB into proteoliposomes (**Fig. S2B**), albeit with lower affinity (EC_{50} = 740 ± 84 μM) (**Fig. 2B**). Taking together, these results show that LicB is a high-affinity choline transporter that displays promiscuous activity towards other choline-like molecules.

Acetylcholine can be processed by *S. pneumoniae* for decoration of teichoic acids

Acetylcholine is a neurotransmitter with function in the central and peripheral nervous system, where it is produced in cholinergic neurons and activates acetylcholine receptors before being processed by acetylcholinesterase. *S. pneumoniae* is one of the major meningitis-causing pathogens in part due to its ability to cross the blood-brain barrier (*45*). During invasion of the central nervous system, *S. pneumoniae* can be exposed to acetylcholine. Thus, in light of the promiscuous transport activity of LicB towards this molecule, we tested whether *S. pneumoniae* can make use of acetylcholine to supply the pathway that carry out decoration of TA. To do this, we grew *S. pneumoniae* D39V cells in choline-reduced media containing acetylcholine isotopically labeled with [^{3}H]-methyl at its trimethyl-ammonium group (**Fig. 2C**). After harvesting the cells, we performed extraction of TA and quantification of their radiolabeled content (**Fig. 2C**). Our results show prominent [^{3}H] radioactivity in TA extracts, indicating that indeed acetylcholine was used for functionalization of TA.

To demonstrate that acetylcholine has been hydrolyzed by *S. pneumoniae*, and that only its choline moiety was used for decoration of TA, we performed the same experiment but in presence of acetylcholine labeled with [^{3}H]-methyl at its acetyl group (**Fig. 2C**). In this case, we expected to see background levels of radioactivity as the choline moiety will remain unlabeled after acetylcholine hydrolysis. Our results show that extracted TA display 100-fold lower levels of [^{3}H] radioactivity in comparison to what was observed for extracted TA, when acetylcholine labeled at its trimethyl-ammonium group was used (**Fig. 2C**). These results reveal that *S. pneumoniae* is able

to uptake acetylcholine, hydrolyze it, and supply the phosphocholine synthesis pathway for functionalization of TA. Thus, the promiscuous activity of LicB represents an advantage that allows retrieving choline from alternative sources.

Sybodies inhibit LicB activity but do not affect *S. pneumoniae* growth *in vitro*

We reasoned that due to the small size of LicB (32-kDa), complex formation with a sybody (~16 kDa) would facilitate structure elucidation by single particle cryo-EM. Thus, we raised sybodies against biotinylated LicB in the presence of 5 mM choline through a combination of ribosome- and phage-display (*46, 47*). Subsequent ELISA screening resulted in the identification of multiple sybodies exhibiting good expression levels and decent behavior on SEC. To characterize the effect of sybodies on choline transport, we reconstituted LicB in proteoliposomes and performed SSM-electrophysiology as described before (*48*). We measured electrogenic transport after activation with 5 mM choline and evaluated peak current amplitudes in the presence and absence of 12 sybodies (**Fig. 2D and Fig. S3**). Five sybodies displayed strong inhibition of LicB transport activity, as evidenced by a decrease of about 80% of the peak currents, whereas seven sybodies did not affect choline electrogenic transport (**Fig. 2D**). Whereas the sequences of the complementarity determining regions (CDRs) of inhibitory sybodies shared high similarity, the CDR regions of non-inhibitory sybodies were more diverse (**Fig. S4**). We further selected a set of three inhibitory sybodies (Sybodies A, B, and D) and one non-inhibitory (Sybody-C), based on their high yields of expression and good behavior during and after purification (**Fig. S5**), and determined their binding kinetics using Grating-coupled interferometry (GCI). This showed that all sybodies bind to LicB with high-affinity displaying binding constants (K_D) in the range of 30 to 40 nM. Interestingly, binding constants did not differ in the presence of 5 mM choline, indicating that the inhibitory sybodies can bind equally well to choline-bound and substrate-free LicB and are thus not conformationally selective (*49*) (**Fig. S6**).

Due to their small size, strong antigen affinity, low immunogenicity, and easy production, sybodies are strong candidates for development of therapeutics (*50-52*). Thus, we wanted to test whether the inhibitory sybodies A, B and D, were able to affect growth of *S. pneumoniae* due to inhibition of LicB activity. To test this, we grew unencapsulated *S. pneumoniae* D39V cells (strain VL567) in liquid media in presence of the selected inhibitory sybodies, and the non-inhibitory sybody-C as a control, at concentrations ranging from 0.25 µM to 25 µM (**Fig. S7**). Our results indicate that under these experimental conditions, the three inhibitory sybodies tested did not affect *S. pneumoniae* growth. We hypothesize that sybodies might be unable to penetrate the cell wall, or that the remaining LicB choline transport activity, 14% to 28% based on SSM-electrophysiology

measurements (**Fig. 2D**), might suffice to supply the pathway for phosphocholine synthesis.

Structure of outward-open LicB in complex with sybody

We incorporated purified *S. pneumoniae* LicB in nanodiscs containing a mixture of POPG and *E. coli* polar lipid extract (3:1, w:w), and incubated with the non-inhibitory sybody-C during reconstitution (**Fig. S8A**). In contrast to the inhibitory sybodies, sybody-C led to cryo-EM data of better quality. The LicB:Sybody complex structure was solved to a nominal resolution of 3.75 Å (**Fig. 3A, Fig. S8B-D and S9A, and Table 1**). Sybody-C was found bound via its CDR3 region to cytoplasmic loop 4 located between TM4 and TM5 of LicB (**Fig. 3A,B**). The structure revealed a LicB dimer in nanodiscs, with both protomers having the same topological orientation (**Fig. 3A,C**). The dimer interphase involves hydrophobic interactions between aromatic and aliphatic residues located in TM1, TM8, and TM9, and a putative partially resolved POPG lipid molecule, the most prominent phospholipid in the *S. pneumoniae* membrane (*53*) (**Fig. 3C,D and Fig. S9B,C**). The polar headgroup of the lipid faces the extracellular side of the membrane and the aliphatic tails are surrounded mostly by aromatic residues (**Fig. S9B,C**).

LicB displays a 10-TM helix topology with both N- and C-terminal domains facing the cytoplasm (**Fig. 3B,C**). LicB exhibits the DMT superfamily fold consisting of two 'inverted' structural repeats with antiparallel topology comprised by the N-terminal (TM1-TM5) and the C-terminal (TM6-TM10) domains (**Fig. 3B**). TM1–TM4 and TM6–TM9 form a central cavity that opens up towards the extracellular side of the membrane, indicating that the structure is in an outward-open conformation (**Fig. 3E**). Access to the central cavity from the cytoplasmic face is sealed off by multiple interactions between TM6-TM9 and TM7-TM8 and the cytoplasmic loops connecting TM6-7 and TM8-9. Multiple aromatic residues including W17 (TM1), Y109 (TM4), W167 (TM6), Y233 (TM9), Y236 (TM9), and Y255 (TM10) participate in formation of the central cavity (**Fig. 3C**). The structural fold exhibited by LicB is similar to that of other structurally characterized DMT transporters including the amino-acids exporter Yddg (*54*), the *Plasmodium falciparum* drug transporter PfCRT (*55*), the triosephosphate/phosphate antiporter TPT (*56*), and the SLC35 nucleotide sugar antiporters CST (*57, 58*) and Vrg4 (*59, 60*).

Structure of choline-bound LicB in occluded state

A choline-bound structure, displaying a different conformational state to that observed by cryo-EM, was obtained after co-crystallization of *S. pneumoniae* LicB in presence of choline (**Fig. 4A, Fig. S10A,B and Table 2**). An important experimental aspect to solve this structure was to perform dehydration of LicB crystals, which improved diffraction resolution from 6 to 3.8 Å. Phases were

204 determined by molecular replacement using a LicB protomer from the cryo-EM structure as search
205 model. The overall electron density map was of good quality throughout the polypeptide chain,
206 except for loops 2 and 7, which were not included in the final model (**Fig. 4A**). The crystal structure
207 revealed a conformation occluded from both sides of the membrane (**Fig. 4B**). Access to the central
208 cavity is sealed by extracellular interactions between helices TM1-TM4 and TM2-TM3, and the
209 loops connecting TM1-2 and TM3-4, and by cytoplasmic interactions between TM6-TM9 and
210 TM7-TM8 and the cytoplasmic loops connecting TM6-7 and TM8-9. A clear positive peak in the
211 *Fo-Fc* map indicated the presence of choline in the central cavity (**Fig. 4A and Fig. S10B**).
212 Residues coordinating the choline molecule include W17 (TM1), Y109 (TM4), W167 (TM6), Y233
213 (TM8), and Y255 (TM9), which form an 'aromatic box' surrounding the trimethylammonium
214 group, whereas Y236 (TM8), and N252 (TM9) coordinate the hydroxyl end of the molecule.
215 Computational docking confirmed that the same binding pocket could accommodate an
216 acetylcholine molecule (**Fig. S11A**). The larger size of acetylcholine likely explains the lower
217 affinity observed for this molecule (**Fig. 2B**). In agreement with the distribution of substrate binding
218 residues described here for LicB, substrate-bound structures of other DMT transporters, including
219 the triosephosphate/phosphate antiporter TPT (*56*) and the SLC35 nucleotide sugar antiporters CST
220 (*57, 58*) and Vrg4 (*59, 60*), have shown that residues from TM1-TM4, from the first inverted repeat,
221 and TM6-TM9, from the second repeat, are involved in substrate coordination. Thus, albeit the
222 significant differences among substrates of DMT transporters, the arrangement of substrate binding
223 residues seems to be conserved.
224
225 **Conserved choline binding residues are relevant for *S. pneumoniae* fitness**
226 Sequence conservation analysis revealed that residues W17, Y109, W167, Y233, Y236, N252, and
227 Y255, participating in coordination of choline at the central pocket are highly conserved among
228 LicB proteins across different bacterial phyla (**Fig. 4C and Fig. S11B**), including the Gram-
229 negative pathogen *H. influenzae* (**Fig. S11C**). To further show the importance of residues
230 participating in choline binding, we performed complementation assays in *S. pneumoniae*. First, we
231 constructed strains in which residues participating in formation of the 'aromatic box' surrounding
232 the trimethylammonium group of choline (**Fig. 4A**) were exchanged to alanine (W17A, W167A,
233 Y233A, Y236A) and the genes encoding these variants were cloned under the control of an IPTG-
234 inducible promoter (P_{lac}) and integrated at the ectopic ZIP locus as second copy of *licB* (*61*).
235 Transformation assays were done aiming to replace the native *licB* gene with an erythromycin
236 resistance cassette and transformants were plated with and without IPTG. As expected, wild type
237 (WT) P_{lac}-*licB* could complement the *licB* deletion (**Fig. 4D**). We obtained an average

transformation efficiency of approximately 1% in the presence of IPTG while no colonies appeared in the absence of IPTG. Exchange to alanine of residues Y233 and W167 resulted in transformation efficiencies comparable to WT *licB*, whereas mutants W17 and Y236 resulted in significantly reduced transformation efficiencies indicating that these are essential residues for LicB function (**Fig. 4D**). Thus, slight modifications of the binding pocket of LicB are sufficient to perturb fitness of *S. pneumoniae*.

LicB is a proton-dependent choline symporter

The central cavity of LicB displays multiple charged residues in close proximity to the choline binding site (**Fig. 4A**), with residues H43, E170, and R191, being conserved among LicB proteins from different bacterial species (**Fig. 4C and Fig. S11B**). The chloroquine resistant transporter PfCRT, which has been described to be a H^+-coupled transporter, displays similar charged residues located at its central cavity (*55, 62*). Charged residues in central cavities of secondary transporters have been frequently associated with proton transport as these residues are prone to protonation and de-protonation due to fluctuations in their surrounding chemical environment during cycling. We wanted to test whether similarly to PfCRT, LicB could display H^+-coupled activity. To test this, we performed membrane potential driven H^+ transport assays with LicB reconstituted in proteoliposomes in presence of the fluorophore 9-amino-6-chloro-2-methoxyacridine (ACMA) (**Fig. 4E**). The robust fluorescence decrease observed upon the addition of valinomycin reflects H^+ influx into LicB-WT proteoliposomes in contrast to the slower quenching of ACMA observed in protein-free liposomes (**Fig. 4E**). Similar experiments with variants E170A, R191A, and H43A reconstituted in proteoliposomes (**Fig. 4E**), revealed that H^+ influx decreases for variants R191A and H43A, whereas E170A exhibited influx similar to that of WT LicB (**Fig. 4E**). Complementation assays in *S. pneumoniae* using the above-mentioned transformation assay, showed that H43A supports viability, whereas mutants E170A and R191A did not (**Fig. 4D**). Strikingly, E170 and R191 are particularly highly conserved residues among bacteria phyla where genes of the *lic* operon are found (**Fig. 4C**), with only very few exceptions as indicated in **Fig. 4F**. Taken together, these results led us to hypothesize that H^+-coupled choline import is a highly conserved trait of LicB proteins across bacteria displaying phosphocholine decoration.

Comparison of LicB outward-open and occluded conformations

Structures of other DMT transporters have been solved either in outward-open or occluded states, and so far, there are no structures available for inward-facing states (*54-56*). Modeling of different conformations have been possible thanks to the structural conservation of the DMT fold and the

pseudo-symmetrical arrangement of TM helices in two inverted repeats (*38*). However, until now, LicB is the only DMT transporter with elucidated structures in two distinct structural states. Analysis of the conformational changes taking place during the transition from outward-open to occluded state, shows that TM3 and TM6 are the main players in closing the access to the central cavity as they move towards the core of the translocation pathway (**Fig. 5A,B**). During this transition, the extracellular halves of TM3 and TM6 tilt about 20°. An inward-facing model based on the pseudo-symmetrical arrangement of the two repeats, predict that the transition from occluded- to inward-open conformation would involve movements of the cytoplasmic halves of TM1 and TM8 (**Fig. 5B**). Large movements of the extracellular halves of TM3 and TM6 are favored by the flexibility introduced by glycine residues at their midsections. In TM3 this includes residues G83-G86; G168 in TM6; G14-G18-G20 in TM1; and G216-G220 in TM8. Similar flexible segments have been observed in YddG (*54*), TPT (*56*), Vrg4 (*60*), and CST (*57, 58*), and glycine residues at this same regions are present in LicB proteins, indicating that similar conformational changes are expected to occur in these proteins.

LicB is inhibited by hemicholinium-3

The importance of LicB in maintaining the choline supply for phosphocholine synthesis, makes this transporter a very attractive target for drugs development. However, besides the inhibitory sybodies described here, there are no reported inhibitors of LicB. In particular, it would be important to develop small molecule inhibitors with the potential to cross the cell wall. Hemicholinium-3 (HC-3) is a well characterized inhibitor of the high-affinity choline transporter CHT1 (SLC5A7) (*63*), a member of the sodium-solute symporter family in which the structurally characterized members exhibit the conserved LeuT-fold (*64*). Albeit, the architecture of DMT and LeuT-fold transporters is markedly different, we wanted to test whether HC-3 could inhibit the choline transport activity of LicB. To test this, we performed SSM-electrophysiology measurements with LicB reconstituted in proteoliposomes, and evaluated electrogenic currents in presence of different concentrations of HC-3 (**Fig. 5C**). Our results show that at a concentration of 0.5 mM of HC-3, the electrogenic transport of choline is reduced about 50%, while at 2 mM, the activity is reduced about 90%. HC-3 displays non-competitive binding to LicB with a K_i of 518 ± 31 μM (**Fig. 5C**). This mode of inhibition indicates that HC-3 does not bind to the choline binding pocket, in agreement with the larger size of this molecule in comparison to choline. Computational docking of HC-3 to the outward-open structure of LicB revealed that it preferentially binds to the extracellular entrance pathway, blocking the access to the central binding site (**Fig. 5D,E**). Taking together, these results indicate that HC-3 is a genuine scaffold for future design of inhibitors targeting LicB proteins.

Discussion

Phosphocholine synthesis is an essential part of the pathways that decorate TA and LPS in pathogenic bacteria. Considering the significant roles of these two biopolymers in adhesion to host cells, immune evasion, and bacterial persistence (*7, 8*), understanding the mechanisms of proteins involved in phosphocholine decoration is critical for the development of strategies aiming to counteract bacterial infections. Pathogens like *S. pneumoniae* and *H. influenzae* are unable to synthesize choline, thus, uptake of this molecule is a fundamental step in exploiting the advantages that TA or LPS phosphocholine decoration provide. The essential role of LicB in supplying with choline the protein machinery encoded by the *lic* operon to perform TA and LPS decoration, makes LicB and other proteins related to this process promising targets for drugs development. Thus, demonstrating how LicB works and elucidating architectural and mechanistic elements essential to its function is of significant relevance. The role of catalytic residues involved in choline binding and proton-coupling in *S. pneumoniae* LicB as described here, and their high conservation across divergent bacteria phyla, support the essential role of these mechanistic elements in supplying the phosphocholine synthesis pathway for decoration of TA and LPS. Indeed, a homology model of *H. influenzae* LicB reveals a central cavity with an 'aromatic box' and charged residues at the same positions as in *S. pneumoniae* LicB (**Fig. S11C**).

Despite the fact that inhibitory sybodies targeting LicB pose great potential to counteract bacterial pathogens, further strategies aiming to facilitate sybodies diffusion across their capsule and cell wall need to be developed. On the other hand, small molecule inhibitors, such as HC-3, are likely to inhibit LicB activity much more effectively under native conditions due to less restricted diffusion. Thus, the biochemical and structural characterization of the inhibitory mechanism of HC-3 set the basis for development of high specificity inhibitors.

The promiscuous selectivity of LicB is a striking finding that point towards an adaptation mechanism of *S. pneumoniae* under conditions with limited accessibility to free choline. We demonstrated that *S. pneumoniae* can catabolize acetylcholine and use the choline product for TA functionalization. However, the nature of the protein(s) that perform acetylcholine hydrolysis in *S. pneumoniae* and how conserved is this mechanism among other bacteria remains to be shown. Docking analysis of acetylcholine indicates that the highly conserved catalytic residues involved in choline binding, suffice to coordinate acetylcholine. Thus, we speculate that LicB proteins in other bacteria would be able to import acetylcholine as well.

From the structurally characterized DMT transporters, PfCRT is the most similar to LicB in terms of function as it performs symport towards the cytoplasm (*55, 62*). PfCRT exports drugs from the acidic digestive vacuole of intra-erythrocytic *P. falciparum* parasites (*62*). Comparison of outward-

open LicB and outward-open PfCRT (PDB: 6UKJ), which superpose with an r.m.s.d. of 2.6 Å (Cα atoms), reveal similarities in the location of charged residues in their central cavities; $H43_{LicB}/H97_{PfCRT}$, $E170_{LicB}/D137_{PfCRT}$, $R191_{LicB}/R231_{PfCRT}$, and $D229_{LicB}/D326_{PfCRT}$. Like LicB, PfCRT also makes use of the electrochemical proton gradient (*65*). Proton-coupled transport by LicB implicates that acidification of the external media would result in faster choline uptake. This might be relevant at the natural niche of pathogens like *S. pneumoniae* and *H. influenzae*, the human nasopharynx, which displays mild acidic conditions ($5.0 < pH < 6.5$) (*66, 67*). In the absence of a proton gradient, neutral pH, or in the presence of a mutation that disrupts proton transport (H43A), transport of choline is driven by the membrane potential and likely by a choline concentration gradient since the phosphocholine synthesis pathway quickly diminishes the concentration of free choline in the cytoplasm (*36, 68, 69*).

The cryo-EM structure of LicB in nanodiscs revealed a homodimer arrangement. Dimerization has been observed in crystal structures of DMT transporters including the triosephosphate/phosphate antiporter TPT (*56*), the GDP-mannose transporter Vrg4 (*59, 60*) and the CMP-sialic acid transporter CST (*57, 58*). Strikingly, the dimer arrangement displayed by LicB is very different to that observed in the crystal structures of these DMT transporters. While the LicB interprotomer interactions involve TM1, TM8, and TM9 (**Fig. 3D**), the interactions observed in the structures of TPT, Vrg4, and CST, involve TM5 and TM10. Interestingly, the packing of the crystal structure of LicB shows a symmetry partner that interact through TM5 and TM10, thus, displaying the same dimer topology as that described for TPT, Vrg4, and CST (**Fig. S10C**). Although for TPT, it is not known whether the dimer is functionally relevant, it has been shown that dimerization of Vrg4 and CST allows faster transport and enhances protein stability (*57, 59*). Since LicB dimerization was observed during purification, albeit in low proportion (**Fig. S12**), and lipid nanodiscs represent a native-like environment due to the presence of a lipid bilayer and absence of detergent micelles, the arrangement of LicB molecules in the cryo-EM structure might represent a functional dimer, but this remains to be shown.

More broadly, we showed a comprehensive mechanistic analysis of a DMT transporter essential for bacterial cell wall modification. Due to the widespread importance of phosphocholine decoration of teichoic acids and lipopolysaccharide in bacterial pathogens, our results constitute a significant advance that is likely to contribute to the development of new strategies to modulate interactions with the host. Indeed, sybody-like molecules or derivatives of HC-3 represent promising chemical structures that will facilitate the engineering of new molecules targeting LicB proteins.

Materials and Methods

LicB expression, purification and nanodiscs reconstitution. The gene encoding *S. pneumoniae* LicB with an N-terminal 10×His affinity tag in a modified pET-19b vector (Novagen) was overexpressed in *E. coli* BL21-Gold (DE3) (Stratagene) cells. The cells were grown at 37°C in Terrific Broth medium supplemented with 1% glucose (w/v) and 100 µg/ml ampicillin. Protein overexpression was induced with 0.2 mM β-D-1-thiogalactopyranoside (IPTG) and cells were incubated for 1 hour before harvesting. Frozen cell pellets were resuspended in 50 mM Tris-HCl, pH 8.0; 500 mM NaCl; 5 mM β-mercaptoethanol and 0.5 mM PMSF. Cells were disrupted, the membrane fraction was separated by ultracentrifugation and subsequently flash frozen with liquid nitrogen until further use. Frozen membranes were solubilized for 2 hours at 4°C in 50 mM Tris-HCl, pH 8.0; 200 mM NaCl; 15 % glycerol (v/v); 20 mM imidazole, pH 8.0; 1% Lauryl Maltose Neopentyl Glycol (w/v) (LMNG, Anatrace); and 2 mM β-mercaptoethanol. After centrifugation the supernatant was loaded onto a Ni-NTA superflow affinity column (Qiagen), pre-equilibrated on 50 mM Tris-HCl, pH 8.0; 500 mM NaCl; 10 % glycerol; 20 mM imidazole, pH 8.0; 0.2% LMNG and 2 mM β-mercaptoethanol and subsequently washed with buffer containing 50 mM Tris-HCl, pH 8.0; 500 mM NaCl; 10 % glycerol (v/v); 50 mM imidazole, pH 8.0; 0.2% LMNG and 2 mM β-mercaptoethanol. The protein was eluted with buffer containing 50 mM Tris-HCl, pH 8.0; 200 mM NaCl; 10 % glycerol (v/v); 500 mM imidazole, pH 8.0; 0.2% LMNG and 2 mM β-mercaptoethanol. The buffer was exchanged to 10 mM Tris-HCl, pH 8.0; 150 mM NaCl and 0.012% LMNG with PD-10 columns (GE healthcare) for the removal of imidazole. The 10×His affinity tag was removed by overnight incubation with Tobacco Etch Virus (TEV) protease, which was later removed by passing through a Ni-NTA affinity column. LicB was further purified by size exclusion chromatography (SEC) with running buffer 10 mM Tris-HCl, pH 8.0; 150 mM NaCl and 0.012% LMNG, using a Superdex 200 Increase 10/300 GL column (GE Healthcare). Purified LicB was reconstituted in MSP1D1 nanodiscs using a ratio of 3:9:7:175 (LicB:Sybody:MSP1D1:lipids) in a buffer containing 50 mM Tris-HCl, pH 8.0; 50 mM NaCl and 10 % glycerol (v/v). The lipid mixture used consist of 16:0-18:1 POPG:*E. coli* polar lipid extract (Avanti) in a 3:1 (w:w) ratio. Detergent was removed by adding Bio-beads SM2 (BioRad). After Bio-beads removal the mixture was centrifuged and loaded on a Superdex 200 Increase 10/300 GL (GE Healthcare) column equilibrated with buffer 50 mM Tris-HCl, pH 8.0; 50 mM NaCl. The peak corresponding to LicB:Sybody in nanodiscs was collected and used for single particle cryo-EM studies.

Synthetic nanobody (sybody) selection. LicB carrying an N-terminal Avi-tag, followed by a SSGTSS linker sequence to warrant efficient biotinylation, was expressed and purified as described

above. Enzymatic biotinylation was performed using recombinant BirA in presence of 0.5 mM biotin, 20 mM Magnesium acetate, 20 mM ATP, and 5% glycerol(*70*). The reaction was incubated for 16 hours at 4°C. Protein biotinylation was confirmed by SDS-PAGE after incubation of the reaction product with Streptavidin. Biotinylated LicB was desalted with buffer 10mM Tris-HCl pH 8.0, 150 mM NaCl, 0.012% LMNG, and His-tagged BirA was removed using a Ni-NTA superflow affinity column. The protein was aliquoted at a concentration of 5 µM, flash frozen in liquid nitrogen, and stored at -80°C until used for nanobodies selection. Sybody selection was performed as previously described(*46*). In short, sybodies were selected against biotinylated LicB in presence of 5 mM choline using the three sybody libraries concave, loop and convex. After one round of ribosome display, two rounds of phage display were performed, switching the panning surface in each round. During the second round of phage display, an off-rate selection was carried using non-biotinylated LicB at a concentration of 5 µM. The enrichment was monitored throughout the selection process by qPCR, which looked ideal with values of 4.6 (concave), 2.5 (loop) and 3.3 (convex) after the first round of phage display and 1922 (concave), 107 (loop) and 70 (convex) after the second round of phage display. 95 single clones of each library were screened by ELISA resulting in 40 hits. Sanger sequencing revealed 29 unique sybodies, of which 26 showed a monodisperse peak at the expected elution volume on a Sepax SRT-10C SEC-100 column. From these, the best behaved sybodies during expression and purification (12 sybodies, all belonging to the convex sybody library, **Fig. S4**) were selected for further functional characterization.

Sybody expression and purification. Sybodies were expressed and purified as previously described(*46, 47*), with minor modifications. In brief, the sybody encoding gene in the pSBinit vector (Addgene #110100) was transformed into *E. coli* MC1061 competent cells, which were then grown at 37°C in Terrific broth media supplemented with 0.004 % glycerol, 100 µg/ml ampicillin and 100 µg/ml streptomycin. Overexpression of the protein was induced with 0.02% L-arabinose at an OD_{600} of 0.7, followed by 15 hours incubation at 22°C before harvesting. The cell pellet was resuspended in 40 mM Tris-HCl, pH 7.4; 500 mM NaCl; 0.5 mM PMSF and cells were lysed using a tip sonicator. The cell debris was discarded by centrifugation and the supernatant was loaded on a Ni-NTA affinity chromatography column equilibrated with 40 mM Tris-HCl, pH 7.4; 150 mM NaCl; 50 mM imidazole. The column was washed with 40 mM Tris-HCl, pH 7.4; 150 mM NaCl; 50 mM imidazole, and the protein eluted with 40 mM Tris-HCl, pH 7.4; 150 mM NaCl; 300 mM imidazole. Imidazole was then removed using a PD-10 column (GE Healthcare). The concentrations of sybody preparations were determined by measuring A_{280} and the quality of the purified sybodies was assessed by SDS-PAGE and SEC.

Sybody binding constant determination. Kinetic characterization of sybodies binding to biotinylated LicB was performed using grating-coupled interferometry (GCI) on a WAVEsystem instrument (Creoptix AG). Biotinylated LicB was captured onto a Streptavidin PCP-STA WAVEchip (polycarboxylate quasi-planar surface; Creoptix AG) to a density of 1700 pg/mm^2. Sybodies were injected at increasing concentrations ranging from 5 nM to 405 nM using a three-fold serial dilution and 5 different concentrations in buffer 10 mM Tris-HCl pH 8.0, 150 mM NaCl, 20 mM imidazole supplemented with 0.02 % LMNG with or without 5 mM choline. Sybodies were injected for 200 s at a flow rate of 50 µl/min. Dissociation recording was set to 900 s to allow the return to baseline. Blanks were injected after every second analyte injection. All sensorgrams were recorded at 25°C and the data was analyzed on the WAVEcontrol software (Creoptix AG). Data were double-referenced by subtracting the signals of buffer injections (blanks) and by subtracting the signals of a reference channel. A Langmuir 1:1 model was used for data fitting. For Sybody-C the two highest concentrations were excluded from data fitting, due to unspecific interaction with the flow channels at high concentrations.

Sample preparation and cryo-EM data acquisition. A sample of nanodiscs reconstituted LicB:sybody-C complex was concentrated between 1 to 1.5 mg/ml using a Vivaspin concentrator with a 30,000 Da cutoff (GE Healthcare). Cryogenic samples were prepared using a Mark IV Vitrobot (Thermo Fisher) at 95% humidity at 4°C. 5 µl of the sample was applied to glow discharged Quantifoil R1.2/1.3 300-mesh copper holey carbon grids, blotted for 4 seconds using a blotting force of 3. The grids were flash frozen in a mixture of propane and ethane, then cooled with liquid nitrogen. Movies were recorded with SerialEM on a Glacios microscope (Thermo Fisher) operated at 200 kV, equipped with a K3 direct electron detector (Gatan). Images were recorded with a defocus range of 0.5 and 3 µm and a pixel size of 0.878 Å/pixel at a nominal magnification of 46,000 ×. Each micrograph was dose-fractionated to 25 frames under a dose rate of 12.5 electrons per pixel per second, with a total exposure time of 4 seconds, resulting in a total dose of about 50 $e^-/Å^2$.

Cryo-EM data processing. Data processing was carried out entirely in cryoSPARC v3.2.0(*71*). Beam-induced drift of 8,229 raw movies was corrected and the movies aligned using patch motion correction. The contrast transfer function (CTF) of each aligned micrograph was determined using patch CTF estimation. Micrographs were Fourier-cropped once during patch motion correction to adjust the pixel size to 0.878 Å per pixel. Micrographs were classified and some discarded, based

476 on CTF fit resolution, relative ice thickness, and total full-frame motion, resulting in 8,008
477 micrographs. A small subset of micrographs was used to adjust parameters for optimal picking of
478 particles, which was performed using blob picker. 3,113,507 particles were extracted with a box
479 size of 384 pixel and Fourier-cropped to 192 pixels, resulting in a pixel size of 1.756 Å per pixel.
480 Multiple rounds of 2D classification with a batch size of 200 particles per class were performed to
481 discard bad particles. The selected particles were used to perform sequential *ab initio*
482 reconstructions with 3 or 4 classes, no similarity, and C1 symmetry. The best-resolved class was
483 used as reference for multiple rounds of heterogeneous refinement with the particle sets selected
484 from the preceding round of 3D classification. After heterogeneous refinement, 148,064 good
485 particles were re-extracted, resulting in a pixel size of 0.878 Å per pixel, and further refined in a
486 non-uniform (NU) refinement(*71*) using C2 symmetry, input reconstruction map filtered to 12 Å,
487 and per-group CTF parameters. NU-refinement resulted in a map with a 4.2 Å resolution, according
488 to the 0.143 cut-off criterion(*72*). This reconstruction map was used to generate templates for
489 automated template-based picking from all good micrographs. Particles were re-extracted and a
490 similar processing procedure as that described above was applied. After NU-refinement, a set of
491 78,649 particles were locally CTF refined before local resolution refinement, which resulted in a
492 map with a 3.75 Å resolution, according to the 0.143 cut-off criterion. The local resolution was
493 estimated with cryoSPARC v3.2.0(*71*) and the directional resolution estimation was done using the
494 3DFSC server(*73*).
495
496 **Model building.** Model building was performed in Coot(*74*). The cryo-EM density of the LicB
497 dimer was of sufficiently high resolution to unambiguously build LicB polypeptide chain into the
498 cryo-EM density. The sybody was only partially resolved, with the part interacting with LicB being
499 its best resolved region. Thus, a homology model of the sybody (based on PDB: 5m14) was
500 positioned by rigid body in the density map, accompanied of manual building of the CDR3 region.
501 Models were improved by iterative cycles of real-space refinement in PHENIX(*75*) with application
502 of secondary structure constrains. Validations of models were performed in PHENIX. The final
503 refined structure has 95.43% of residues in the Ramachandran favored region; 4.32% in
504 Ramachandran allowed; and 0.25% as Ramachandran outliers. Figures of models and densities
505 were made in PyMol (The PyMOL, Molecular Graphics Systems, Schödinger, LLC), and
506 ChimeraX(*76, 77*).
507
508 **LicB crystallization.** LicB in buffer 10 mM Tris-HCl, pH 8.0; 150 mM NaCl; 0.012% LMNG was
509 concentrated up to 8 mg/ml using a 30 kDa MWCO Vivaspin 20 concentrator (GE healthcare).

Extensive optimisation of crystal conditions using sitting-drop and hanging-drop vapour diffusion and other post-crystallisation treatments yielded plate shaped crystals after 3-4 days of incubation at 20°C. The reservoir conditions contained 1.5 mM choline; 100 mM HEPES, pH 7.5; and 33% PEG 400. Optimised crystals were dehydrated and cryoprotected by gently increasing PEG 400 concentration in the drop. Crystals were scooped from the drop at different time points followed by flash freezing by immersion in liquid nitrogen.

Data collection. LicB crystals diffracted X-rays up to about 6-7 Å resolution in general. Drop dehydration through air exposure over 30 minutes led to crystals that diffracted X-rays to higher resolution(*78*). A data-set collected from one LicB crystal that showed anisotropic diffraction and belonged to space group C121 was used to determine the structure. The unit cell constants of this crystal were a = 128.9 Å, b = 43.44 Å, c = 126.82 Å and α = 90º, β = 120.43º, γ = 90º (**Table 2**). Data was processed and merged with XDS(*79, 80*) and anisotropic scaling/ellipsoid truncation was performed(*81*). Resolution limits after ellipsoid truncation were a* = 4.0 Å, b* = 3.5 Å, and c* = 4.2 Å. Karplus CC* (Pearson correlation coefficient) based data cutoff approach was used to determine the usable resolution of the data-sets(*82*). The resolution limit was set considering a $CC_{1/2}$ > ~40% based on data merging statistics and a CC* analysis against unmerged intensities in Phenix package(*75*) satisfying Karplus CC* against CC_{work} and CC_{free} criteria, as well as, R_{free} of the highest resolution shell against the refined structure being less than or equal to ~50%. A second criterion for limiting the resolution was the overall completeness percentage observed after anisotropic ellipsoid truncation, which was kept above 85%. Diffraction data was collected at the beamline X06SA at the Swiss Light Source (SLS, Villigen).

LicB crystal structure determination. The crystal structure of LicB was solved by molecular replacement using the program PHASER(*83*). The model generated by single particle cryo-EM was used as reference. Multiple rounds of refinement in Phenix(*75*) and model building using Coot(*74*) were performed. Map sharpening was used to facilitate model building. X-ray data and refinement statistics are given in **Table 2**. The final refined structure has R_{work} = 29.69% and R_{free} = 31.97%, with 92.16% of residues in the Ramachandran favored region; 7.84% in Ramachandran allowed; and 0.0% as Ramachandran outliers. Molecular graphics were created in PyMOL (The PyMOL, Molecular Graphics Systems, Schödinger, LLC). Surface electrostatics were calculated with the APBS PyMOL plugin.

Reconstitution in proteoliposomes. Lipid mixtures of POPE:POPG 3:1 or ECPL:PC 3:1 (w:w)

(Avanti), were mixed, dried from chloroform, and solubilised in buffer 20 mM Tris, pH 8.0; 150 mM NaCl; 2 mM β-mercaptoethanol, to a final concentration of 20 mg/ml. The lipids were flash frozen with liquid nitrogen and stored at -80°C. Unilamellar liposomes were formed after a 1:1 dilution in buffer and extrusion through a polycarbonate filter (400-nm pore size). After addition of 0.2% DDM, liposomes were mixed with LicB to have a 1:50 TM protein:lipid ratio (w:w). Detergent was removed with Bio-beads SM2 (BioRad). Proteoliposomes at a final concentration of 20 mg/ml of lipids were resuspended in 10 mM HEPES, pH 7.3; 100 mM KCl; 5 mM choline for the proton transport assay, and in 20 mM Tris, pH 8.0; 150 mM KCl; 2 mM β-mercaptoethanol for the SSM-based electrophysiology assays. The proteoliposomes were aliquoted, flash frozen in liquid nitrogen and stored at -80°C until further use.

SSM-based electrophysiology. SSM-based electrophysiology was conducted using a SURFE2R N1 instrument (Nanion Technologies) following published protocols(*48, 84*). 3 mm SURFE2R N1 single sensors (Nanion Technologies) were alkylated by adding 100 µl of 0.5 mM thiol solution (1-octadecanethiol in isopropanol), subsequently incubating for 1 hour at room temperature in a closed petri dish. The sensor was then washed with isopropanol and miliQ water. 1.5 µl of lipid solution (7.5 µg/µl 1,2-diphytanoyl-sn-glycero-3-phosphocholin in n-decane) was applied on the surface of the gold electrode followed by immediate addition of 100 µl of SSM-buffer (50 mM Tris-HCl, pH 8.0; 5 mM $MgCl_2$; 150 mM KCl). The proteoliposome suspension at a 20 mg/ml lipid concentration was diluted 1:20 in SSM-buffer and the mixture was sonicated for 20 seconds. 10 µl of the diluted proteoliposomes were added to the chip before centrifugation at 2,000 × g for 30 minutes. The conductance and capacitance were measured to ensure the quality of the SSM before each measurement. A conductance value below 5 nS, and capacitance between 15 - 35 nF were considered acceptable. Activating buffers (buffer-A) were prepared from a large stock of non-activating buffer (buffer-B: SSM-Buffer) by the addition of the substrate choline or other compounds such as arsenocholine, and acetylcholine at different concentrations ranging between 1 µM to 30 mM. Peak current values were determined for each individual substrate at different concentrations and plotted to calculate EC_{50} values. For the determination of the inhibitory constants of hemicholinium-3 (HC-3), the choline concentration was adjusted to 0.5, 1, 5, 10 mM choline in buffer-A, respectively and measured in the presence of 0.25, 0.5, 1 and 5 mM HC-3 present in buffer-A and buffer-B. Assays with sybodies were performed at a constant concentration of choline at 5 mM in buffer-A and 500 nM sybody in buffer-A and buffer-B as previously described(*48*). Prior to the measurements in presence of sybody, the maximal peak current was determined with 5 mM choline in buffer-A and used to normalise the peak currents in presence of

sybody. Data for each sybody was collected from 3 independent sensor preparations and measured in triplicates. Analysis of the data was performed in OriginPro (OriginLab Corporation) and GraphPad Prism 9 (GraphPad Software).

Protons transport assay. POPE:POPG (3:1) proteoliposomes were thawed and 20 µl of the proteoliposomes were sonicated and diluted to 500 µl with buffer containing 10 mM HEPES, pH 7.3, 10 mM KCl; 90 mM NaCl; 5 mM choline, and 0.75 µM 9-amino-6-chloro-2-methoxycridine (ACMA), before the assay. Time course fluorescence was measured at 20°C using a Jasco Fluorimeter. The change in ACMA fluorescence was detected using an excitation wavelength of 410 nm and an emission wavelength of 480 nm. After equilibration of the system, H^+ and choline influx was initiated by establishing a membrane potential by the addition of the K^+-selective ionophore valinomycin (5 nM). The activity was assessed for 1,200 seconds. The proton gradient was collapsed by the addition of 0.5 µM carbonyl cyanide m-chlorophenyl hydrazone (CCCP). Time courses were repeated at least three times for each individual experiment.

Size-exclusion chromatography coupled to multi-angle light scattering. SEC-MALS measurements of LicB were performed at 18°C in 10 mM Tris-HCl, pH 8.0; 150 NaCl; 0.012% LMNG using a GE Healthcare Superdex 200 Increase 10/300 GL column on an Agilent 1260 high performance liquid chromatography. The column was equilibrated overnight for a stable baseline before data collection. Monitoring of the elution was carried out with a multi wavelength absorbance detector at 280 nm and 254 nm, the Wyatt Heleos II 8+ multiangle light-scattering detector, and a Wyatt Optilab rEX differential refractive index detector. Inter-detector delay volumes, light-scattering detector normalization and broadening corrections were calibrated using a 2 mg/ml bovine serum albumin solution (ThermoPierce) and standard protocols in ASTRA 6 (Wyatt Technologies). Weight-averaged molar mass, elution concentration, and mass distribution of the samples were calculated using the ASTRA 6 software (Wyatt Technologies). The dn/dc for the detergent LMNG was assumed to be 0.146 mg/ml according to experimental data(*85*).

Mutagenesis. Point mutations H43A and R191A were introduced by site-directed mutagenesis using primers(*86*) (**Table S1**). Point mutations Y233A, Y236A, N252A, W17A, W167A and E170A were introduced by cloning using gBlock gene fragments (Integrated DNA Technologies) (**Table S1**).

Sequence-similarity network. A sequence-similarity network of LicB proteins from multiple

612 bacteria species (nodes) was generated using the EFI-EST webserver(*87*). Bacteria species were
613 selected considering that *lic* operon genes encoding LicB and proteins that perform choline
614 activation (LicA and LicC) are present(*88*). Sequences wre visualized with 40% identity and
615 organized by phylum in Cytoscape(*89*). The phylogenetic tree showing the evolutionary
616 relationships among the selected bacteria species was generated with iTOL(*90*).
617
618 **Structural sequence-conservation analysis.** The sequence conservation analysis shown in **Fig.**
619 **10B** was computed using the ConSurf server(*91*). Briefly, LicB homologues displaying at least 35%
620 identity were selected from a protein sequence BLAST search on the NCBI database using *S.*
621 *pneumoniae* LicB protein sequence as a query. We then generated a multiple-sequence alignment
622 using the HHMER algorithm provided by ConSurf, with conservation scores plotted in PyMOL
623 (The PyMOL, Molecular Graphics Systems, Schödinger, LLC)**.**
624
625 **Docking of hemicholinium-3 and acetylcholine.** Docking of hemicholinium-3 and acetylcholine
626 to the LicB structures was done with Autodock Vina(*92*). These molecules were downloaded in the
627 SDF format from the ZINC database(*93*) and converted into a PDBQT format using Open
628 Babel(*94*). Docking was carried out over a search space of 28 Å × 56 Å × 30 Å in the outward open
629 state and 38 Å × 34 Å × 42 Å covering the entire entry pathway to the central cavity.
630
631 **Construction of mutants in *S. pneumoniae*.** Strain VL4243 (*S. pneumoniae* D39V, prsI::PF6-lacI-
632 tetR (gen), bgaA::Plac-licB (tet)) was made as follows. A second copy of *licB* under control of the
633 IPTG-inducible P_{lac} promoter(*95*) was integrated in the genome of parental strain D39V at the *bgaA*
634 locus. Golden Gate assembly of three parts was used. First part is the amplification by PCR using
635 chromosomal DNA of strain VL1998 (lab collection) as template with primers OVL5139 and
636 OVL5623 (**Table S1**). The resulting product contained the upstream homologous region to
637 integrate at the *bgaA* locus, the tetracycline marker (*tet*), P_{lac} and the RBS. The second part is the
638 amplification by PCR of *licB,* without its own RBS, from D39V with primers OVL5624 and
639 OVL5625. The third part is the amplification by PCR using chromosomal DNA of strain VL1998
640 as template with primers OVL5626 and OVL2082 resulting on the downstream homologous region
641 to integrate at the *bgaA* locus. After purification, the three parts were digested and ligated together
642 during an assembly reaction with T4 DNA ligase buffer (Vazyme), T4 DNA ligase (Vazyme) and
643 Eps3I (NEB). The assembly mixture was incubated in a thermocycler (PCR Max) by cycling 25 ×
644 the series 1.5 minutes at 37°C and 3 minutes at 16°C. The sample was then incubated for 5 minutes
645 at 37°C and subsequently incubated for 10 minutes at 80°C. Strain VL333 (prsI::PF6-lacI-tetR

(gen)(*96*)) was transformed with the assembly mixture and transformants were selected using tetracycline (µg/ml). The *bgaA* locus of the resulting strain, VL4243, was confirmed by sequencing. To create seven different point mutations in *licB*, the desired amino acids were changed for alanine in the second copy of *licB* at *bgaA*. Golden Gate assembly was used to amplify two parts per point mutation. The first part is the amplification by PCR of the upstream region of *bgaA::Plac-licB* from VL4243 until the desired point mutation with forward primer OVL2077 and reverse primer for each point mutation, OVL6035 (Y233A), OVL6037 (Y236A), OVL6039 (W17A), OVL6041 (W167A), OVL6043 (E170A), OVL6045 (R191A) or OVL6047 (H43A). The second part is the amplification by PCR of *bgaA::Plac-licB* from VL4243, started at the point mutation location until the downstream homologous region to integrate at the *bgaA* locus. Different forward primers were used for each point mutation, OVL6036 (Y233A), OVL6038 (Y236A), OVL6040 (W17A), OVL6042 (W167A), OVL6044 (E170A), OVL6046 (R191A), OVL6048 (H43A), the reverse primer was identical, OVL2082. After purification, the two parts were digested with Esp3I and ligated together during an assembly reaction with T4 DNA ligase buffer (Vazyme), T4 DNA ligase (Vazyme) and Eps3I (NEB). Strain VL333 was transformed with the assembly mixture with tetracycline selection. The *bgaA* region containing the P_{lac}-*licB* genes of the resulting strains, VL4250 (Y233A), VL4251 (Y236A), VL4252 (W17A), VL4253 (W167A), VL4254 (E170A), VL4255 (R191A), VL4256 (H43A) were confirmed by sequencing.

Transformation efficiency assay. Transformation efficiencies were determined to test whether mutated *licB* alleles would support growth as only copy of *licB* in the pneumococcal genome. Transformation assays were performed by transforming DNA of a *licB::ery* cassette to the strains with both copies of *licB* (without and with point mutation). DNA of *licB::ery* was obtained by amplification by PCR of strain VL4249 (lab collection) with primers OVL5635 and OVL5636. To transform *S. pneumoniae*, cells were grown in C+Y medium (pH 6.8) at 37°C to an OD of 0.1 at 595 nm. Subsequently, cells were treated for 12 minutes at 37°C with synthetic CSP-1 (100 ng /ml) and incubated for 20 minutes at 30°C with the transforming DNA (*licB::ery*). After incubation with the transforming DNA, cells were grown in C+Y medium (pH 6.8) at 37°C for 60 minutes. *S. pneumoniae* transformants were selected by plating, in triplicates, inside Columbia agar supplemented with 4% of defibrinated sheep blood (Thermo Scientific Oxoid) with 0.5 µg/ml erythromycin and 0 or 0.1 mM IPTG. To obtain the viable count, the transformant mix was diluted 1,000 or 10,000 times and plated without induction and selection, in triplicate, inside Columbia agar supplemented with 4% of defibrinated sheep blood. Transformation efficiency in percentage is calculated as the number of transformants divided by the number of total CFUs (viable count).

680

681 ***S. pneumoniae* sybodies susceptibility assays.** Growth assays of unencapsulated *S. pneumoniae*
682 strain VL567 (*cps::chl*) were performed in presence or absence of sybodies-A, -B, -C and -D at
683 three different concentrations. Bacteria were grown in microtiter plates (CytoOne, CC 7672-7596)
684 and incubated at 37°C, without shaking, in a Tecan i-Control infinite 200 PRO. Bacterial growth
685 was monitored by measuring the optical density at 595 nm every 10 minutes during 8 hours.
686 Measurements were performed using three replicates per condition. Strain VL567 was grown in
687 C+Y (pH 6.8) until the optical density at 595 nm reached 0.1. Cells were spun down to remove the
688 media and replaced by fresh C+Y medium. These washed pre-cultures were diluted 20-fold in C+Y
689 without sybody or in presence of the four sybodies at different final concentrations per well.

690

691 ***S. pneumoniae* teichoic acids extraction and analysis.** Cells were grown in 5 ml modified C+Y
692 media(*97*) without choline or yeast containing radiolabeled [^{3}H]-acetylcholine either at the acetyl
693 group or the amino-group at 37°C until the OD reached 0.5 using 600 nm. The cell solution was
694 split in two equal halves to LTA and WTA extraction. For LTA extraction cells were centrifuged
695 at 5,000 × g for 5 minutes and the pellet washed twice with 1 ml buffer 20 mM MES, pH 6.5; 0.5
696 M sucrose; 20 mM MgCl2, before resuspending it in 1 ml of the same buffer. Proteoplasts were
697 generated by the addition of 20 mg/ml lysozyme and 100 units mutanolysin. The mixture was
698 incubated for 30 minutes at 37°C. The protoplasts were pelleted at 5,000 × g for 5 minutes and
699 lysed in ice cold buffer containing 20 mM HEPES, pH 8.0; 100 mM NaCl; 1 mM DTT; 1 mM
700 $MgCl_2$; 1 mM $CaCl_2$; 2 × complete protease inhibitors; 6 µg/ml RNAse A; 6 µg/ml DNAse I.
701 Unbroken spheroplasts were removed by centrifugation at 5,000 × g for 10 minutes. The membrane
702 fraction was collected by ultracentrifugation for 1 hour at 100,000 × g and at 4°C. The pellet was
703 resuspended in 100 µl of buffer containing 50 mM MES, pH 6.5; 150 mM NaCl and the solution
704 was flash frozen and stored at -80°C for further use. For WTA extraction cells were pelleted by
705 centrifugation at 5,000 × g for 5 minutes and resuspended in 1 ml buffer containing 50 mM MES,
706 pH 6.5, before a second centrifugation at 5,000 × g for 5 minutes and resuspension in 1 ml buffer
707 containing 50 mM MES, pH 6.5; 4% (w/v) SDS. The solution was incubated at 100°C for 1 hour.
708 The sacculi were collected with a 5,000 × g centrifugation for 5 minutes and washed with 1 ml
709 buffer containing 50 mM MES, pH 6.5. The sample was centrifuged in a clean tube at 14,000 × g
710 for 5 minutes. The pellet was washed with 1 ml buffer containing 50 mM MES, pH 6.5; 4% (w/v)
711 SDS, twice with 1 ml buffer containing 50 mM MES, pH 6.5; 2% (w/v) NaCl and one in buffer
712 containing 50 mM MES, pH 6.5. The sample was centrifuged at 14,000 × g for 5 minutes,
713 resuspended in 1 ml buffer containing 20 mM Tris-HCl, pH 8.0; 0.5% (w/v) SDS; 20 µg of

proteinase K. The sample was incubated for 4 hours at 50°C while shaking at 1,000 rpm. The pellet was collected by centrifugation at 14,000 × g for 5 minutes and washed with 1 ml buffer containing 50 mM MES, pH 6.5; 2% (w/v) NaCl. The sample was then washed three times with distilled water. The pellet was collected by centrifugation and hydrolyzed in 0.5 ml alkaline solution of 1 N sodium hydroxide. The mixture was incubated for 16 hours at 25°C while shaking at 1,000 rpm. Insoluble material was pelleted by centrifugation at 14,0000 × g for 5 minutes and the supernatant transferred into a clean tube. 125 µl of Tris-HCl, pH 7.8 was added to neutralize the reaction and the sample was flash frozen until further use. The samples were quantified by liquid scintillation counting (TRI-CARB, PerkinElmer).

References

1. F. C. Neuhaus, J. Baddiley, A continuum of anionic charge: structures and functions of D-alanyl-teichoic acids in gram-positive bacteria. *Microbiol Mol Biol Rev* **67**, 686-723 (2003).
2. C. Weidenmaier, A. Peschel, Teichoic acids and related cell-wall glycopolymers in Gram-positive physiology and host interactions. *Nat Rev Microbiol* **6**, 276-287 (2008).
3. S. Brown, J. P. Santa Maria, Jr., S. Walker, Wall teichoic acids of gram-positive bacteria. *Annu Rev Microbiol* **67**, 313-336 (2013).
4. T. J. Silhavy, D. Kahne, S. Walker, The bacterial cell envelope. *Cold Spring Harb Perspect Biol* **2**, a000414 (2010).
5. M. P. Bos, V. Robert, J. Tommassen, Biogenesis of the gram-negative bacterial outer membrane. *Annu Rev Microbiol* **61**, 191-214 (2007).
6. Y. Kamio, H. Nikaido, Outer membrane of Salmonella typhimurium: accessibility of phospholipid head groups to phospholipase c and cyanogen bromide activated dextran in the external medium. *Biochemistry* **15**, 2561-2570 (1976).
7. C. R. Raetz, C. Whitfield, Lipopolysaccharide endotoxins. *Annu Rev Biochem* **71**, 635-700 (2002).
8. J. G. Swoboda, J. Campbell, T. C. Meredith, S. Walker, Wall teichoic acid function, biosynthesis, and inhibition. *Chembiochem* **11**, 35-45 (2010).
9. E. Swiatlo, F. R. Champlin, S. C. Holman, W. W. Wilson, J. M. Watt, Contribution of choline-binding proteins to cell surface properties of Streptococcus pneumoniae. *Infect Immun* **70**, 412-415 (2002).
10. J. N. Weiser, M. Shchepetov, S. T. Chong, Decoration of lipopolysaccharide with phosphorylcholine: a phase-variable characteristic of Haemophilus influenzae. *Infect Immun* **65**, 943-950 (1997).
11. J. N. Weiser *et al.*, Phosphorylcholine on the lipopolysaccharide of Haemophilus influenzae contributes to persistence in the respiratory tract and sensitivity to serum killing mediated by C-reactive protein. *J Exp Med* **187**, 631-640 (1998).
12. S. H. Gillespie, S. Ainscough, A. Dickens, J. Lewin, Phosphorylcholine-containing antigens in bacteria from the mouth and respiratory tract. *J Med Microbiol* **44**, 35-40 (1996).
13. M. Barbier *et al.*, Novel phosphorylcholine-containing protein of Pseudomonas aeruginosa chronic infection isolates interacts with airway epithelial cells. *J Infect Dis* **197**, 465-473 (2008).

14. W. E. Swords *et al.*, Binding of the non-typeable Haemophilus influenzae lipooligosaccharide to the PAF receptor initiates host cell signalling. *Cell Microbiol* **3**, 525-536 (2001).
15. D. R. Cundell, N. P. Gerard, C. Gerard, I. Idanpaan-Heikkila, E. I. Tuomanen, Streptococcus pneumoniae anchor to activated human cells by the receptor for platelet-activating factor. *Nature* **377**, 435-438 (1995).
16. H. Iuchi, J. Ohori, T. Kyutoku, K. Ito, Y. Kurono, Role of phosphorylcholine in Streptococcus pneumoniae and nontypeable Haemophilus influenzae adherence to epithelial cells. *Auris Nasus Larynx* **46**, 513-519 (2019).
17. B. Pang *et al.*, Lipooligosaccharides containing phosphorylcholine delay pulmonary clearance of nontypeable Haemophilus influenzae. *Infect Immun* **76**, 2037-2043 (2008).
18. A. Ring, J. N. Weiser, E. I. Tuomanen, Pneumococcal trafficking across the blood-brain barrier. Molecular analysis of a novel bidirectional pathway. *J Clin Invest* **102**, 347-360 (1998).
19. C. Rosenow *et al.*, Contribution of novel choline-binding proteins to adherence, colonization and immunogenicity of Streptococcus pneumoniae. *Mol Microbiol* **25**, 819-829 (1997).
20. P. Garcia, J. L. Garcia, E. Garcia, R. Lopez, Nucleotide sequence and expression of the pneumococcal autolysin gene from its own promoter in Escherichia coli. *Gene* **43**, 265-272 (1986).
21. J. Yother, D. E. Briles, Structural properties and evolutionary relationships of PspA, a surface protein of Streptococcus pneumoniae, as revealed by sequence analysis. *J Bacteriol* **174**, 601-609 (1992).
22. J. Yother, G. L. Handsome, D. E. Briles, Truncated forms of PspA that are secreted from Streptococcus pneumoniae and their use in functional studies and cloning of the pspA gene. *J Bacteriol* **174**, 610-618 (1992).
23. P. M. Giffard, N. A. Jacques, Definition of a fundamental repeating unit in streptococcal glucosyltransferase glucan-binding regions and related sequences. *J Dent Res* **73**, 1133-1141 (1994).
24. P. Garcia, M. P. Gonzalez, E. Garcia, R. Lopez, J. L. Garcia, LytB, a novel pneumococcal murein hydrolase essential for cell separation. *Mol Microbiol* **31**, 1275-1281 (1999).
25. P. Garcia, M. Paz Gonzalez, E. Garcia, J. L. Garcia, R. Lopez, The molecular characterization of the first autolytic lysozyme of Streptococcus pneumoniae reveals evolutionary mobile domains. *Mol Microbiol* **33**, 128-138 (1999).
26. K. K. Gosink, E. R. Mann, C. Guglielmo, E. I. Tuomanen, H. R. Masure, Role of novel choline binding proteins in virulence of Streptococcus pneumoniae. *Infect Immun* **68**, 5690-5695 (2000).
27. J. Boch, B. Kempf, E. Bremer, Osmoregulation in Bacillus subtilis: synthesis of the osmoprotectant glycine betaine from exogenously provided choline. *J Bacteriol* **176**, 5364-5371 (1994).
28. J. E. Graham, B. J. Wilkinson, Staphylococcus aureus osmoregulation: roles for choline, glycine betaine, proline, and taurine. *J Bacteriol* **174**, 2711-2716 (1992).
29. A. Tomasz, Choline in the cell wall of a bacterium: novel type of polymer-linked choline in Pneumococcus. *Science* **157**, 694-697 (1967).
30. G. C. Whiting, S. H. Gillespie, Investigation of a choline phosphate synthesis pathway in Streptococcus pneumoniae: evidence for choline phosphate cytidylyltransferase activity. *FEMS Microbiol Lett* **143**, 279-284 (1996).

31. A. S. Kharat, A. Tomasz, Drastic reduction in the virulence of Streptococcus pneumoniae expressing type 2 capsular polysaccharide but lacking choline residues in the cell wall. *Mol Microbiol* **60**, 93-107 (2006).
32. X. Fan, H. Goldfine, E. Lysenko, J. N. Weiser, The transfer of choline from the host to the bacterial cell surface requires glpQ in Haemophilus influenzae. *Mol Microbiol* **41**, 1029-1036 (2001).
33. W. Vollmer, A. Tomasz, Identification of the teichoic acid phosphorylcholine esterase in Streptococcus pneumoniae. *Mol Microbiol* **39**, 1610-1622 (2001).
34. X. Fan, C. D. Pericone, E. Lysenko, H. Goldfine, J. N. Weiser, Multiple mechanisms for choline transport and utilization in Haemophilus influenzae. *Mol Microbiol* **50**, 537-548 (2003).
35. S. E. Clark, J. N. Weiser, Microbial modulation of host immunity with the small molecule phosphorylcholine. *Infect Immun* **81**, 392-401 (2013).
36. J. R. Zhang, I. Idanpaan-Heikkila, W. Fischer, E. I. Tuomanen, Pneumococcal licD2 gene is involved in phosphorylcholine metabolism. *Mol Microbiol* **31**, 1477-1488 (1999).
37. A. Eberhardt, L. J. Wu, J. Errington, W. Vollmer, J. W. Veening, Cellular localization of choline-utilization proteins in Streptococcus pneumoniae using novel fluorescent reporter systems. *Mol Microbiol* **74**, 395-408 (2009).
38. D. L. Jack, N. M. Yang, M. H. Saier, Jr., The drug/metabolite transporter superfamily. *Eur J Biochem* **268**, 3620-3639 (2001).
39. S. Schuldiner *et al.*, Small is mighty: EmrE, a multidrug transporter as an experimental paradigm. *News Physiol Sci* **16**, 130-134 (2001).
40. J. Bondy *et al.*, Haemophilus influenzae LicB contributes to lung damage in an aged mice co-infection model. *Microb Pathog* **90**, 1-6 (2016).
41. A. Bazzone, M. Barthmes, K. Fendler, SSM-Based Electrophysiology for Transporter Research. *Methods Enzymol* **594**, 31-83 (2017).
42. T. J. Kurt J. Irgolic, Carlo Kos, William S. McShane and Giuseppe C. Pappalardo, Preparation of trimethyl -2- hydroxyethylarsonium (arsenocholine) compounds *Applied Organometallic Chemistry* **1**, 403-412 (1987).
43. C. Perez *et al.*, Substrate-bound outward-open state of the betaine transporter BetP provides insights into Na+ coupling. *Nat Commun* **5**, 4231 (2014).
44. T. Hoffmann *et al.*, Arsenobetaine: an ecophysiologically important organoarsenical confers cytoprotection against osmotic stress and growth temperature extremes. *Environ Microbiol* **20**, 305-323 (2018).
45. B. Yau, N. H. Hunt, A. J. Mitchell, L. K. Too, BloodBrain Barrier Pathology and CNS Outcomes in Streptococcus pneumoniae Meningitis. *Int J Mol Sci* **19**, (2018).
46. I. Zimmermann *et al.*, Synthetic single domain antibodies for the conformational trapping of membrane proteins. *Elife* **7**, (2018).
47. I. Zimmermann *et al.*, Generation of synthetic nanobodies against delicate proteins. *Nat Protoc* **15**, 1707-1741 (2020).
48. N. Barland, C. Perez, Selection of Transporter-Targeted Inhibitory Nanobodies by Solid-Supported-Membrane (SSM)-Based Electrophysiology. *J Vis Exp*, (2021).
49. C. A. J. Hutter *et al.*, The extracellular gate shapes the energy profile of an ABC exporter. *Nat Commun* **10**, 2260 (2019).
50. R. H. van der Linden *et al.*, Comparison of physical chemical properties of llama VHH antibody fragments and mouse monoclonal antibodies. *Biochim Biophys Acta* **1431**, 37-46 (1999).

51. M. Dumoulin *et al.*, Single-domain antibody fragments with high conformational stability. *Protein Sci* **11**, 500-515 (2002).
52. M. E. Iezzi, L. Policastro, S. Werbajh, O. Podhajcer, G. A. Canziani, Single-Domain Antibodies and the Promise of Modular Targeting in Cancer Imaging and Treatment. *Front Immunol* **9**, 273 (2018).
53. M. C. Trombe, M. A. Laneelle, G. Laneelle, Lipid composition of aminopterin-resistant and sensitive strains of Streptococcus pneumoniae. Effect of aminopterin inhibition. *Biochim Biophys Acta* **574**, 290-300 (1979).
54. H. Tsuchiya *et al.*, Structural basis for amino acid export by DMT superfamily transporter YddG. *Nature* **534**, 417-420 (2016).
55. J. Kim *et al.*, Structure and drug resistance of the Plasmodium falciparum transporter PfCRT. *Nature* **576**, 315-320 (2019).
56. Y. Lee *et al.*, Structure of the triose-phosphate/phosphate translocator reveals the basis of substrate specificity. *Nat Plants* **3**, 825-832 (2017).
57. E. Nji, A. Gulati, A. A. Qureshi, M. Coincon, D. Drew, Structural basis for the delivery of activated sialic acid into Golgi for sialyation. *Nat Struct Mol Biol* **26**, 415-423 (2019).
58. S. Ahuja, M. R. Whorton, Structural basis for mammalian nucleotide sugar transport. *Elife* **8**, (2019).
59. J. L. Parker, R. A. Corey, P. J. Stansfeld, S. Newstead, Structural basis for substrate specificity and regulation of nucleotide sugar transporters in the lipid bilayer. *Nat Commun* **10**, 4657 (2019).
60. J. L. Parker, S. Newstead, Structural basis of nucleotide sugar transport across the Golgi membrane. *Nature* **551**, 521-524 (2017).
61. L. E. Keller, A. S. Rueff, J. Kurushima, J. W. Veening, Three New Integration Vectors and Fluorescent Proteins for Use in the Opportunistic Human Pathogen Streptococcus pneumoniae. *Genes (Basel)* **10**, (2019).
62. D. A. Fidock *et al.*, Mutations in the P. falciparum digestive vacuole transmembrane protein PfCRT and evidence for their role in chloroquine resistance. *Mol Cell* **6**, 861-871 (2000).
63. T. Okuda, T. Haga, Functional characterization of the human high-affinity choline transporter. *FEBS Lett* **484**, 92-97 (2000).
64. C. Perez, C. Ziegler, Mechanistic aspects of sodium-binding sites in LeuT-like fold symporters. *Biol Chem* **394**, 641-648 (2013).
65. N. Juge *et al.*, Plasmodium falciparum chloroquine resistance transporter is a H+-coupled polyspecific nutrient and drug exporter. *Proc Natl Acad Sci U S A* **112**, 3356-3361 (2015).
66. J. L. du Plessis, A. B. Stefaniak, K. P. Wilhelm, Measurement of Skin Surface pH. *Curr Probl Dermatol* **54**, 19-25 (2018).
67. M. Harell, H. Mover-Lev, D. Levy, J. Sade, Gas composition of the human nose and nasopharyngeal space. *Acta Otolaryngol* **116**, 82-84 (1996).
68. B. Y. Kwak *et al.*, Structure and mechanism of CTP:phosphocholine cytidylyltransferase (LicC) from Streptococcus pneumoniae. *J Biol Chem* **277**, 4343-4350 (2002).
69. L. Wang, Y. L. Jiang, J. R. Zhang, C. Z. Zhou, Y. Chen, Structural and enzymatic characterization of the choline kinase LicA from Streptococcus pneumoniae. *PLoS One* **10**, e0120467 (2015).
70. B. T. Kuhn *et al.*, Biotinylation of Membrane Proteins for Binder Selections. *Methods Mol Biol* **2127**, 151-165 (2020).
71. A. Punjani, J. L. Rubinstein, D. J. Fleet, M. A. Brubaker, cryoSPARC: algorithms for rapid unsupervised cryo-EM structure determination. *Nat Methods* **14**, 290-296 (2017).

72. P. B. Rosenthal, R. Henderson, Optimal determination of particle orientation, absolute hand, and contrast loss in single-particle electron cryomicroscopy. *J Mol Biol* **333**, 721-745 (2003).
73. Y. Z. Tan *et al.*, Addressing preferred specimen orientation in single-particle cryo-EM through tilting. *Nat Methods* **14**, 793-796 (2017).
74. P. Emsley, K. Cowtan, Coot: model-building tools for molecular graphics. *Acta Crystallogr D Biol Crystallogr* **60**, 2126-2132 (2004).
75. D. Liebschner *et al.*, Macromolecular structure determination using X-rays, neutrons and electrons: recent developments in Phenix. *Acta Crystallogr D Struct Biol* **75**, 861-877 (2019).
76. T. D. Goddard *et al.*, UCSF ChimeraX: Meeting modern challenges in visualization and analysis. *Protein Sci* **27**, 14-25 (2018).
77. E. F. Pettersen *et al.*, UCSF ChimeraX: Structure visualization for researchers, educators, and developers. *Protein Sci* **30**, 70-82 (2021).
78. B. Heras, J. L. Martin, Post-crystallization treatments for improving diffraction quality of protein crystals. *Acta Crystallogr D Biol Crystallogr* **61**, 1173-1180 (2005).
79. W. Kabsch, Xds. *Acta Crystallogr D Biol Crystallogr* **66**, 125-132 (2010).
80. W. Kabsch, Integration, scaling, space-group assignment and post-refinement. *Acta Crystallogr D Biol Crystallogr* **66**, 133-144 (2010).
81. M. Strong *et al.*, Toward the structural genomics of complexes: crystal structure of a PE/PPE protein complex from Mycobacterium tuberculosis. *Proc Natl Acad Sci U S A* **103**, 8060-8065 (2006).
82. P. A. Karplus, K. Diederichs, Linking crystallographic model and data quality. *Science* **336**, 1030-1033 (2012).
83. A. J. McCoy *et al.*, Phaser crystallographic software. *J Appl Crystallogr* **40**, 658-674 (2007).
84. A. Bazzone, M. Barthmes, Functional Characterization of SLC Transporters Using Solid Supported Membranes. *Methods Mol Biol* **2168**, 73-103 (2020).
85. C. Breyton *et al.*, Assemblies of lauryl maltose neopentyl glycol (LMNG) and LMNG-solubilized membrane proteins. *Biochim Biophys Acta Biomembr* **1861**, 939-957 (2019).
86. T. A. Kunkel, Rapid and efficient site-specific mutagenesis without phenotypic selection. *Proc Natl Acad Sci U S A* **82**, 488-492 (1985).
87. R. Zallot, N. Oberg, J. A. Gerlt, The EFI Web Resource for Genomic Enzymology Tools: Leveraging Protein, Genome, and Metagenome Databases to Discover Novel Enzymes and Metabolic Pathways. *Biochemistry* **58**, 4169-4182 (2019).
88. D. Szklarczyk *et al.*, STRING v11: protein-protein association networks with increased coverage, supporting functional discovery in genome-wide experimental datasets. *Nucleic Acids Res* **47**, D607-D613 (2019).
89. P. Shannon *et al.*, Cytoscape: a software environment for integrated models of biomolecular interaction networks. *Genome Res* **13**, 2498-2504 (2003).
90. I. Letunic, P. Bork, Interactive Tree Of Life (iTOL) v5: an online tool for phylogenetic tree display and annotation. *Nucleic Acids Res* **49**, W293-W296 (2021).
91. A. Ben Chorin *et al.*, ConSurf-DB: An accessible repository for the evolutionary conservation patterns of the majority of PDB proteins. *Protein Sci* **29**, 258-267 (2020).
92. O. Trott, A. J. Olson, AutoDock Vina: improving the speed and accuracy of docking with a new scoring function, efficient optimization, and multithreading. *J Comput Chem* **31**, 455-461 (2010).

93. T. Sterling, J. J. Irwin, ZINC 15--Ligand Discovery for Everyone. *J Chem Inf Model* **55**, 2324-2337 (2015).
94. N. M. O'Boyle *et al.*, Open Babel: An open chemical toolbox. *J Cheminform* **3**, 33 (2011).
95. R. A. Sorg, C. Gallay, L. Van Maele, J. C. Sirard, J. W. Veening, Synthetic gene-regulatory networks in the opportunistic human pathogen Streptococcus pneumoniae. *Proc Natl Acad Sci U S A* **117**, 27608-27619 (2020).
96. X. Liu *et al.*, High-throughput CRISPRi phenotyping identifies new essential genes in Streptococcus pneumoniae. *Mol Syst Biol* **13**, 931 (2017).
97. A. Domenech, J. Slager, J. W. Veening, Antibiotic-Induced Cell Chaining Triggers Pneumococcal Competence by Reshaping Quorum Sensing to Autocrine-Like Signaling. *Cell Rep* **25**, 2390-2400 e2393 (2018).

Acknowledgement

We thank NANION Technologies for technical assistance. We thank the staff at the electron microscopy facility at Biozentrum (BioEM lab) and at the PX beamline of the Swiss Light Source (SLS). We thank Tim Sharpe from the Biophysics facility at Biozentrum for SEC-MALS data analysis and Xiaochun Li Blatter for assistance in cell expressions. Work in the Perez lab is supported by the Swiss National Science Foundation (SNSF) (PP00P3_170607), the Helmut Horten Stiftung (HHS), and NANION Research Grant Initiative. Work in the Veening lab is supported by the SNSF (project grants 31003A_172861 and 310030_192517), SNSF JPIAMR grant (40AR40_185533), SNSF NCCR 'AntiResist' (51NF40_180541) and ERC consolidator grant 771534-PneumoCaTChER. Work in the Seeger lab is supported by the SNSF (project grant 310030_188817) and a ERC consolidator grant (no. 772190).

Author Contributions

N.B. performed purifications, crystallization experiments, and functional assays. N.B. and C.P. prepared samples for cryo-EM, processed X-ray and cryo-EM data, built and validated the models. A.R. performed complementation and growth assays under supervision from J.W.-V. G.C. produced samples for sybodies selection. C.A.J.H., and G.C. performed sybodies selection under supervision from M.A.S. G.C. established WTA and LTA extraction assays and N.B. performed extraction experiments. C.P. and N.B. wrote the manuscript with input from all authors. C.P. conceived the project.

Author Information

Competing interests: None declared.

Data and materials availability: Electron microscopy density maps and atomic models have been deposited in the EMDB and PDB, respectively, with accession codes EMD-13268 and PDB 7PAF. Atomic coordinates for the reported crystal structure have been deposited in the PDB under accession code 7B0K.

Figures

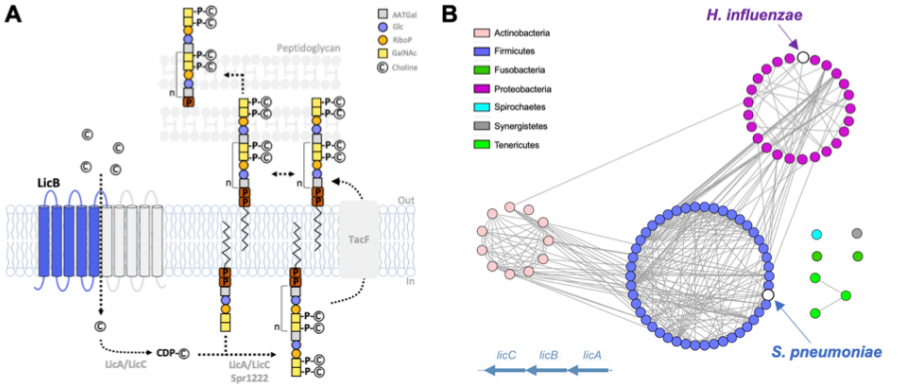

Figure 1. Phosphocholine decoration of teichoic acids and conservation of LicB across divergent bacteria phyla. A. Pathway for phosphocholine decoration of teichoic acids (TA) in *S. pneumoniae*. Choline is imported by LicB and activated by LicA and LicC, before being covalently attached as phosphocholine to TA, which are later exposed at the cell wall. Inverted repeats are shown in blue and gray. **B**. Sequence similarity network of bacteria species (nodes) where *lic* operon genes encoding proteins involved in choline uptake (LicB) and activation (LicA and LicC) are conserved. Edges between nodes correspond to an identity of at least 40% among LicB proteins. Sequences are organized according to bacteria phylum (see Fig. S1). *S. pneumoniae* and *H. influenzae* are indicated.

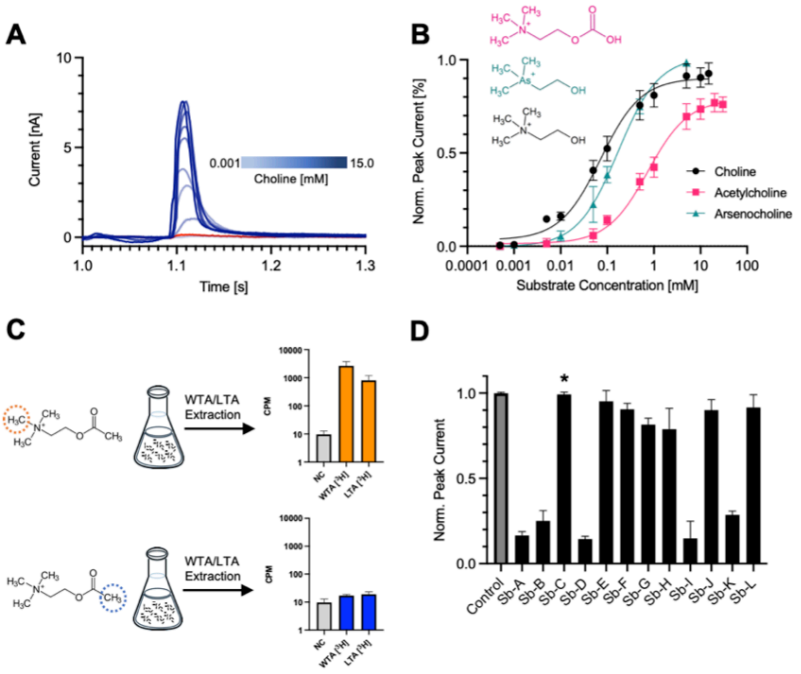

Figure 2. LicB displays promiscuous activity towards choline-like molecules. A. SSM-electrophysiology recordings of choline transport in LicB proteoliposomes. Currents recorded between 1-1.3 seconds after addition of choline are shown in blue. Recordings with protein-free liposomes in presence of 5mM choline is shown in red. **B**. Determination of EC_{50} values for choline, arsenocholine and acetylcholine based on SSM recording as shown in A and Fig. S2. **C**. Wall teichoic acids (WTA) and lipoteichoic acids (LTA) extraction from *S. pneumoniae* cells grown in presence of [^{3}H]-acetylcholine radioactively labeled at different positions indicated by dotted circles. Histograms show the [^{3}H] radioactivity from extracted WTA and LTA. NC, negative control performed with non-radioactive acetylcholine. **D**. Normalized amplitudes of SSM-currents measured in presence of sybodies A to L (500 nM), under 5 mM choline transport conditions based on data shown in Fig. S3. The asterisk denotes Sybody-C, which was used for structural studies. n=3-4 biological replicates, n=2-3 technical replicates, for all experiments.

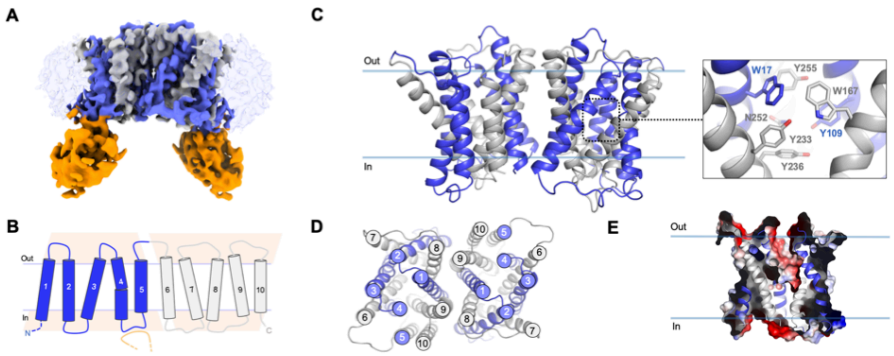

Figure 3. Cryo-EM structure of outward-open *S. pneumoniae* LicB in lipid nanodiscs. A. Cryo-EM density of LicB homodimer in nanodiscs with bound sybody at 3.75 Å. Inverted repeats, TM1-5 and TM6-10, in each protomer are colored in blue and grey, respectively. Sybody is colored in orange. The nanodisc is shown as transparent light blue. **B**. Topology of LicB highlighting the inverted antiparallel repeats shown as pink trapezoids. The CDR3 region of the sybody interacting with the loop connecting TM4 and TM5 is shown in orange. **C**. LicB homodimer and central cavity residues. **D**. Top view of LicB homodimer. **E**. Surface electrostatic potential representation of LicB showing the central cavity opening to the extracellular side of the membrane.

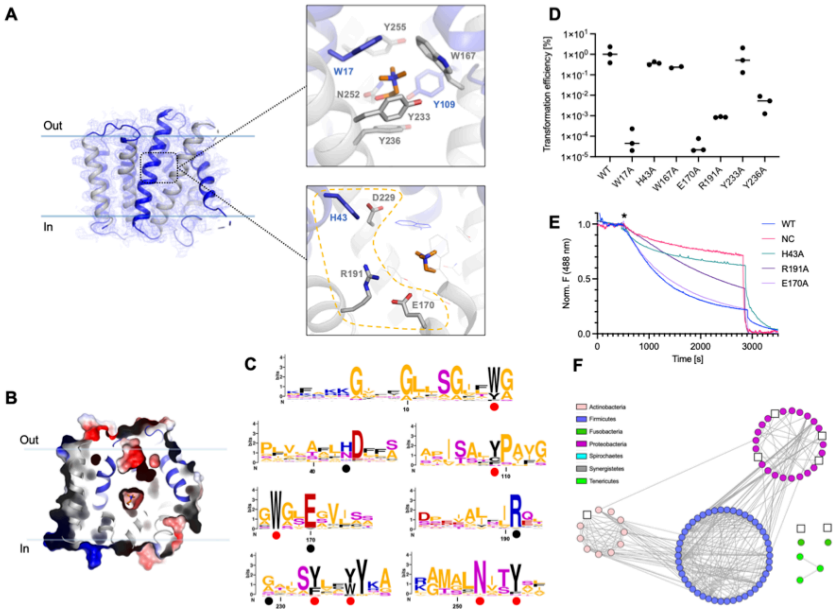

Figure 4. Crystal structure of choline-bound occluded *S. pneumoniae* LicB. A. LicB and *2Fo-Fc* electron density map contoured at 1.0 σ. Inverted repeats, TM1-5 and TM6-10, are indicated in blue and grey, respectively. (*Top*) Choline is shown with carbons colored in orange. (*Bottom*) Charged residues in the vicinity of the choline binding site. **B**. Surface electrostatic potential representation of LicB showing the central cavity closed to both sides of the membrane. Choline is shown in orange. **C**. Sequence logos of the regions containing the choline binding residues (red dots) and charged residues around the central cavity (black dots). Sequences are from LicB proteins analyzed in Fig. 1B (see Fig. S1). The y axis denotes positional information in bits. **D**. Transformation efficiency assays of *S. pneumoniae* D39V Δ*licB* cells complemented with WT *Plac-licB* or variants (n=3, biological replicates). **E**. Proton transport assay with WT LicB and variants in proteoliposomes. Representative time courses are shown (n=3, biological replicates). H^+ influx was induced by establishing a membrane potential upon addition of the potassium ionophore valinomycin (star). The proton gradient was collapsed by the addition of CCCP at about 3000 seconds. NC indicates negative control (protein-free liposomes). **F**. Sequence similarity network as in Fig. 1B, showing bacteria species where residues E170 and R191 are not conserved (white squares, see Fig. S1).

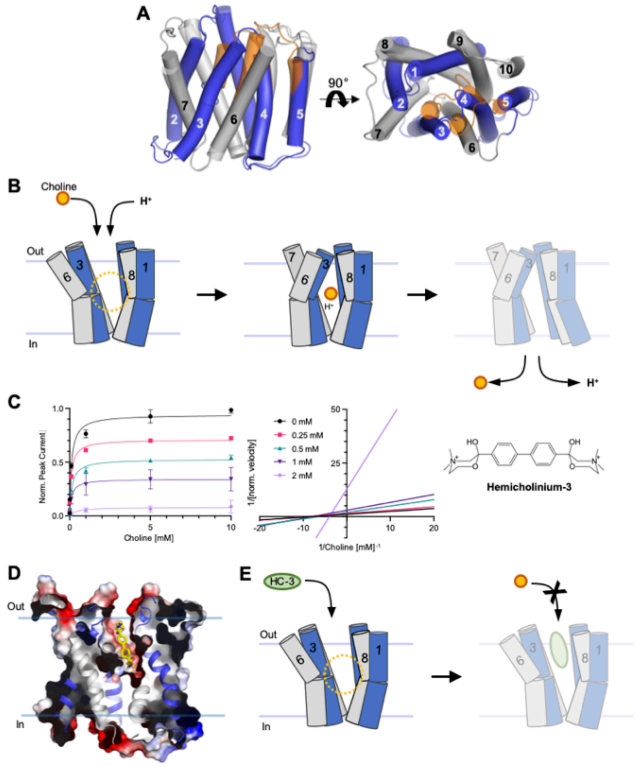

Figure 5. Alternating access model of choline import and inhibition by HC-3. A. Superposition of outward-open and occluded structures of LicB. Inverted repeats, TM1-5 and TM6-10, are indicated in blue and grey, respectively. Helices that undergo large conformational changes are shown in orange in the occluded state. **B**. Schematic of the proposed transport cycle depicting the movements of TM3 and TM6 that close the extracellular entry pathway, whereas the predicted movements of TM1 and TM8 open the cytoplasmic exit pathway. Choline (orange) and protons enter the binding cavity in the outward-open state. **C**. (*Left*) Inhibition of LicB by HC-3 measured by SSM-electrophysiology (K_i=518 ± 31 µM). (*Right*) Lineweaver-Burk plot showing that HC-3 is a non-competitive inhibitor of LicB. Norm. velocity indicates normalization of maximum currents amplitude. **D**. Surface electrostatic potential representation of outward-open LicB showing a HC-3 molecule docked in the extracellular entry pathway. **E**. Schematic of the proposed model of inhibition by HC-3 (green). HC-3 blocks the extracellular entry pathway hindering the access of choline to the central binding site.

Tables

Table 1: Cryo-EM data collection, refinement, and validation statistics

	LicB:Sybody-C in nanodiscs (PDB ID 7PAF, EMD-13268)
Data collection and processing	
Microscope	Glacios TEM
Camera	Gatan K3 GIF
Magnification	46,000
Voltage (kV)	200
Electron exposure (e–/Å^2)	50
Defocus range (μm)	-0.5to -3
Pixel size (Å)	0.878
Symmetry imposed	C2
Initial particle images (no.)	3,113,507
Final particle images (no.)	78,649
Map resolution (Å)	3.75
FSC threshold	0.143
Map resolution range (Å)	3.0-5.0
Refinement	
Model resolution (Å)	3.9
FSC threshold	0.5
Map sharpening b-factor (Å^2)	-75.8
EMRinger score (LicB:Sybody)	2.59
EMRinger score (LicB)	3.25
Model composition	
Non-hydrogen atoms	6272
Protein residues	818
B-factors (Å^2)	
Protein	45.19
R.m.s. deviations	
Bond lengths (Å)	0.006
Bond angles (°)	0.768
Validation	
MolProbity score	2.05
Clashscore	17.08
Poor rotamers (%)	0.00
Ramachandran plot	
Favored (%)	95.43
Allowed (%)	4.32
Disallowed (%)	0.25

Table 2: X-ray data collection and refinement statistics

Data collection	**LicB (PDB ID 7B0K)**
Wavelength (Å)	1.000031
Space group	C 1 2 1
Unit cell:	
a/b/c (Å)	128.90/43.44/126.82
α/β/γ (°)	90.0/120.43/90.0
Resolution (Å)	13-3.8
Completeness (%)	86.8(37.2) [98.9(97.2)]
No. measured reflections	18226(690) [20849 (2305)]
No. unique reflections	5593(196) [7167(694)]
I/σI	4.7(2.3) [2.05(1.2)]
R-meas (%)	14.6(67.7) [23.1(144.7)]
$CC_{1/2}$ (%)	99.6(85.1) [99.5(66.3)]
Refinement	
R_{work}/R_{free} (%)	29.69/31.97
R.m.s.d. Bonds (Å)	0.002
R.m.s.d. Angles (°)	0.605
Ramachandran plot:	
Outliers (%)	0.0
Allowed (%)	7.84
Favored (%)	92.16
Average *B*-factor (Å^2)	107.0

Values in brackets are before anisotropic truncation
Values in parentheses are for the last resolution shell
Rmerge = $\Sigma_{hkl}\Sigma_i |I_i(hkl) - \langle I(hkl)\rangle| / \Sigma_{hkl}\Sigma_i I_i(hkl)$

Supplementary Materials for

Mechanistic basis of choline import involved in teichoic acids and lipopolysaccharide modification

Natalie Bärland, Anne-Stéphanie Rueff, Gonzalo Cebrero, Cedric A.J. Hutter, Markus A. Seeger, Jan-Willem Veening, Camilo Perez*

*Corresponding author. Email: camilo.perez@unibas.ch

This PDF file includes:

Supplementary Text
Figs. S1 to S12
Tables S1

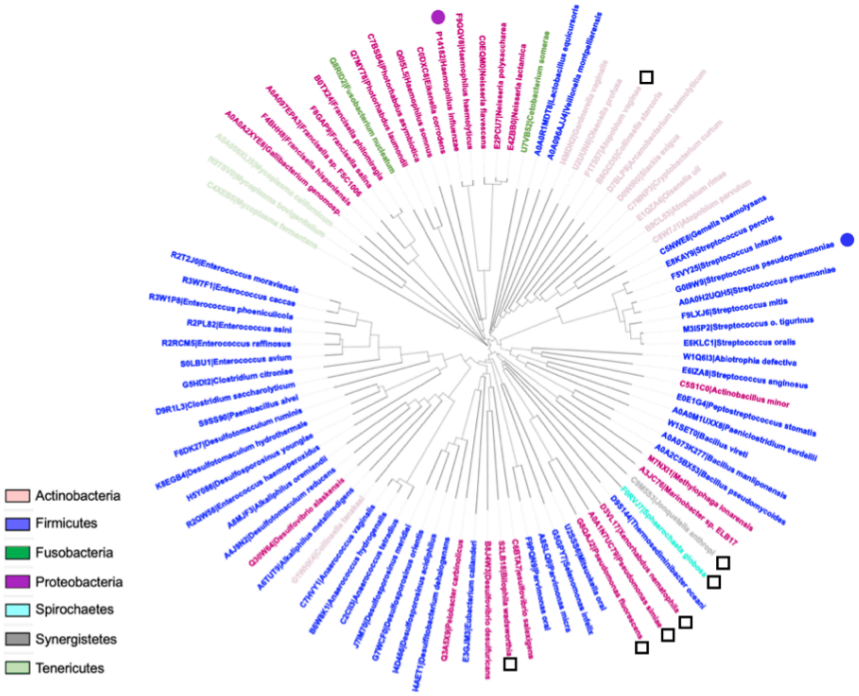

Fig. S1. LicB is conserved across divergent bacteria phyla.

Phylogenetic tree of bacteria species across multiple phyla where *lic* operon genes involved in choline uptake (*licB*) and activation (*licA* and *licC*) are conserved. Phyla are depicted by colors according to the inset. *S. pneumoniae* and *H. influenzae* are indicated by blue and magenta dots. White squares show bacteria species where residues E170 and R191 are not conserved (see Fig. 4).

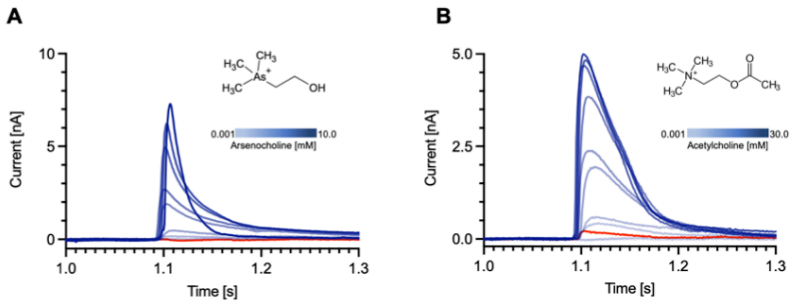

Fig. S2. LicB displays promiscuous selectivity towards arsenocholine and acetylcholine.
SSM-electrophysiology recordings of currents measured during application of arsenocholine (**A**) or acetylcholine (**B**) are indicated by blue curves. Protein-free liposomes traces measured in presence of 5 mM arsenocholine (**A**) or 30mM acetylcholine (**B**) are shown in red. The amplitude of the peak currents were used for determination of EC_{50} values as shown in Fig. 2B.

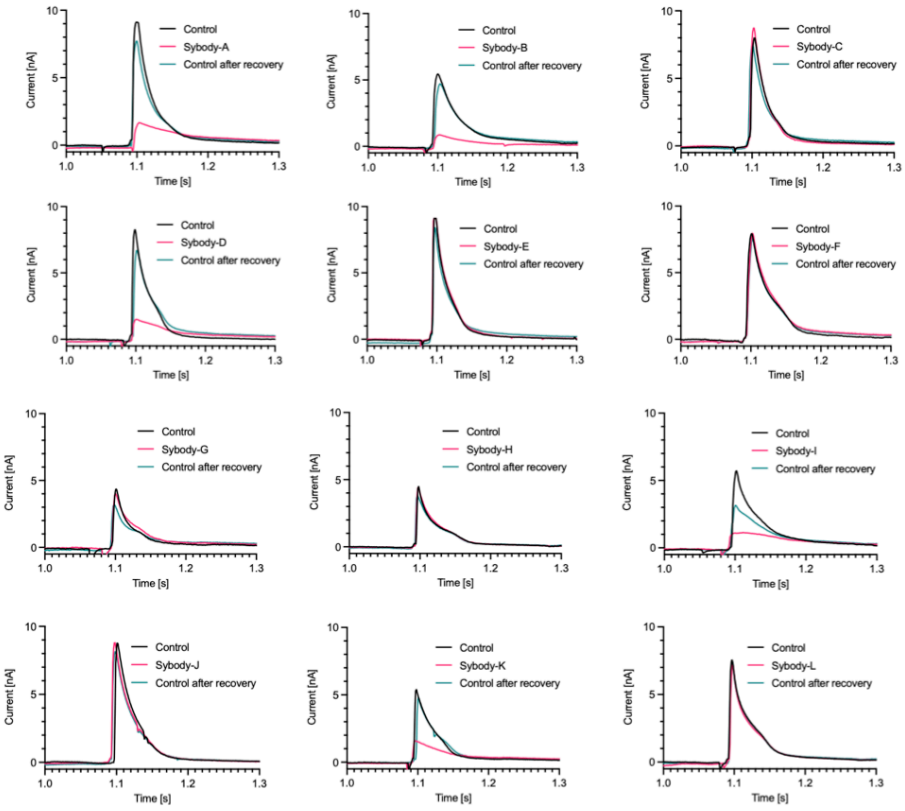

Fig. S3. SSM-electrophysiology recordings of LicB choline transport in presence of sybodies.
Representative recordings of currents measured during application of 5 mM choline in absence of sybodies are shown in black (control). The same experiment but in presence of 500 nM of sybodies are shown in pink, whereas recordings after unbinding of sybodies are shown in green. The amplitudes of the peak currents (pink traces) were used for the generation of the histogram shown in Fig. 2D.

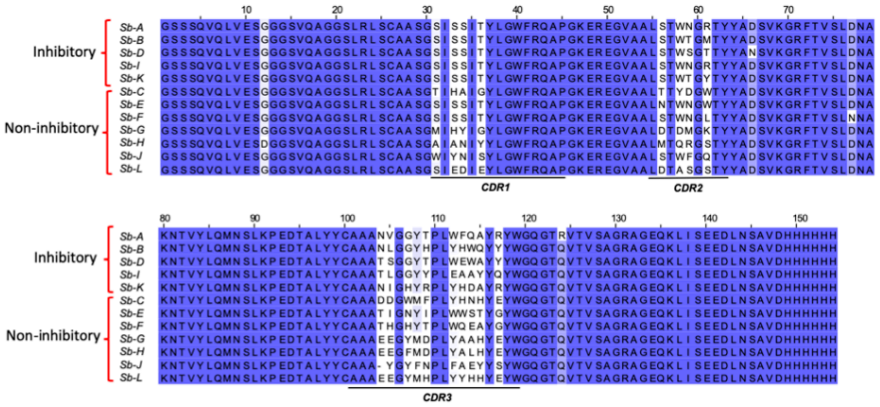

Fig. S4. Sequence conservation alignment of sybodies characterized by SSM-electrophysiology.

Inhibitory and non-inhibitory sybodies are grouped together. All sybodies belong to the convex library, which display a long CDR3 region.

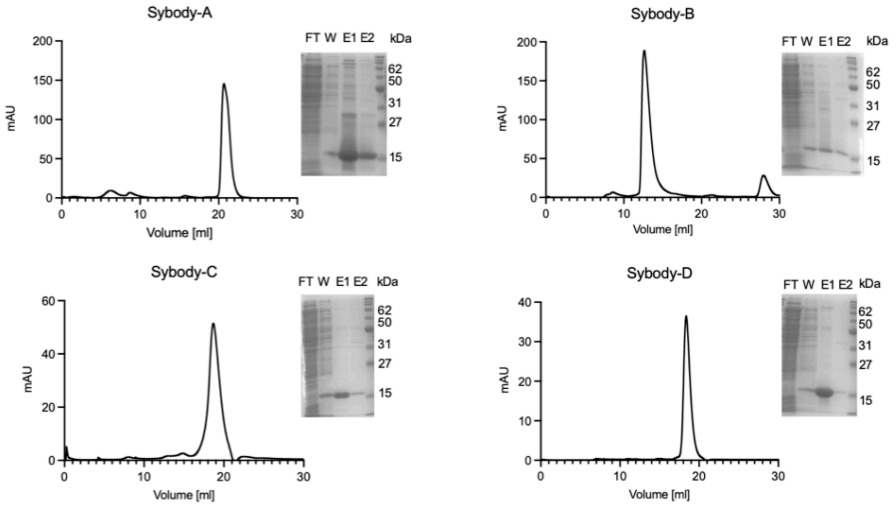

Fig. S5. Purification of sybodies A, B, C and D.

(*Left*) Size exclusion profiles using a Superdex 200 Increase 10/300 column. (*Right*) SDS-PAGE of samples from different steps of sybodies purification. FT, flow through. W, washing of column. E1 and E2, two steps elution.

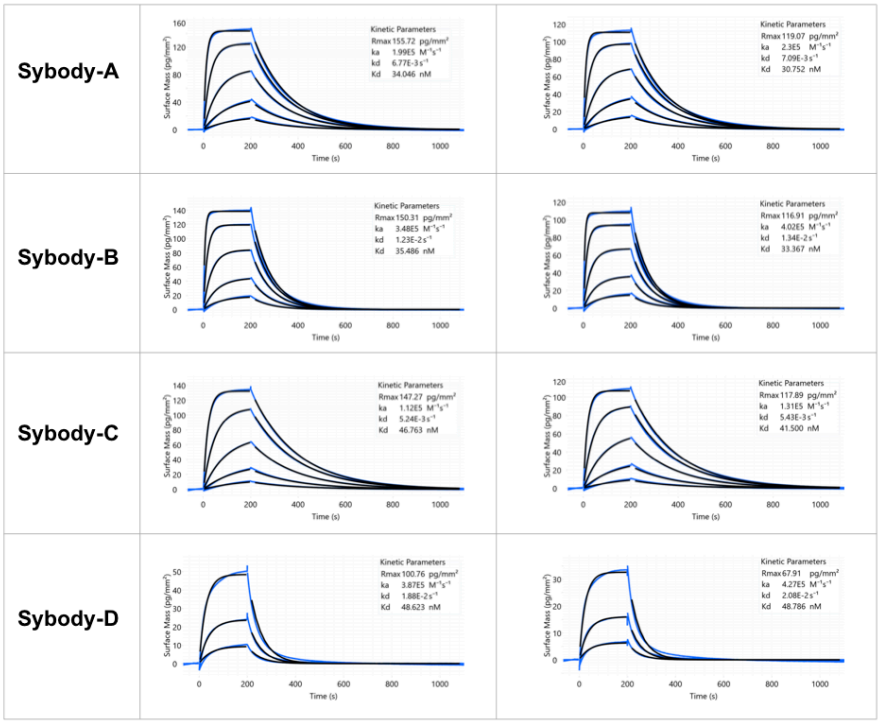

Fig. S6. Determination of binding affinity of Sybodies to LicB by grating-coupled interferometry (GCI).

The four sybodies were injected at 5, 15, 45, 135 and 405 nM concentrations in absence (*left*) or presence of 5 mM choline (*right*). Data are shown in blue and fitting curves in black. Data were fitted using a Langmuir 1:1 model.

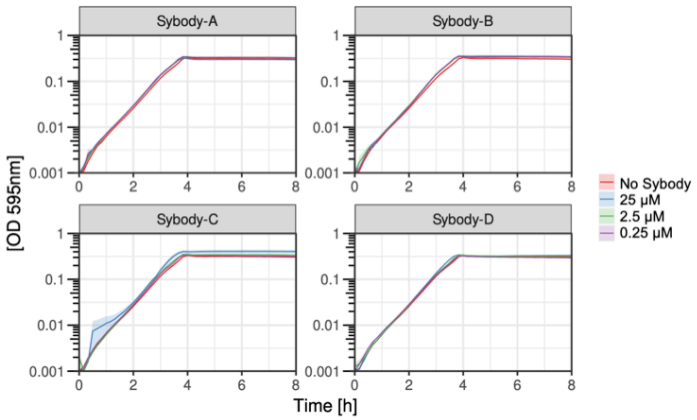

Fig. S7. *S. pneumoniae* growth in presence of sybodies.

Growth curves of unencapsulated *S. pneumoniae* in presence of sybodies targeting LicB in C+Y media supplemented with choline. Three different concentrations of sybodies were tested in comparison with growth without sybody. An average of three replicates and standard error of the mean are plotted.

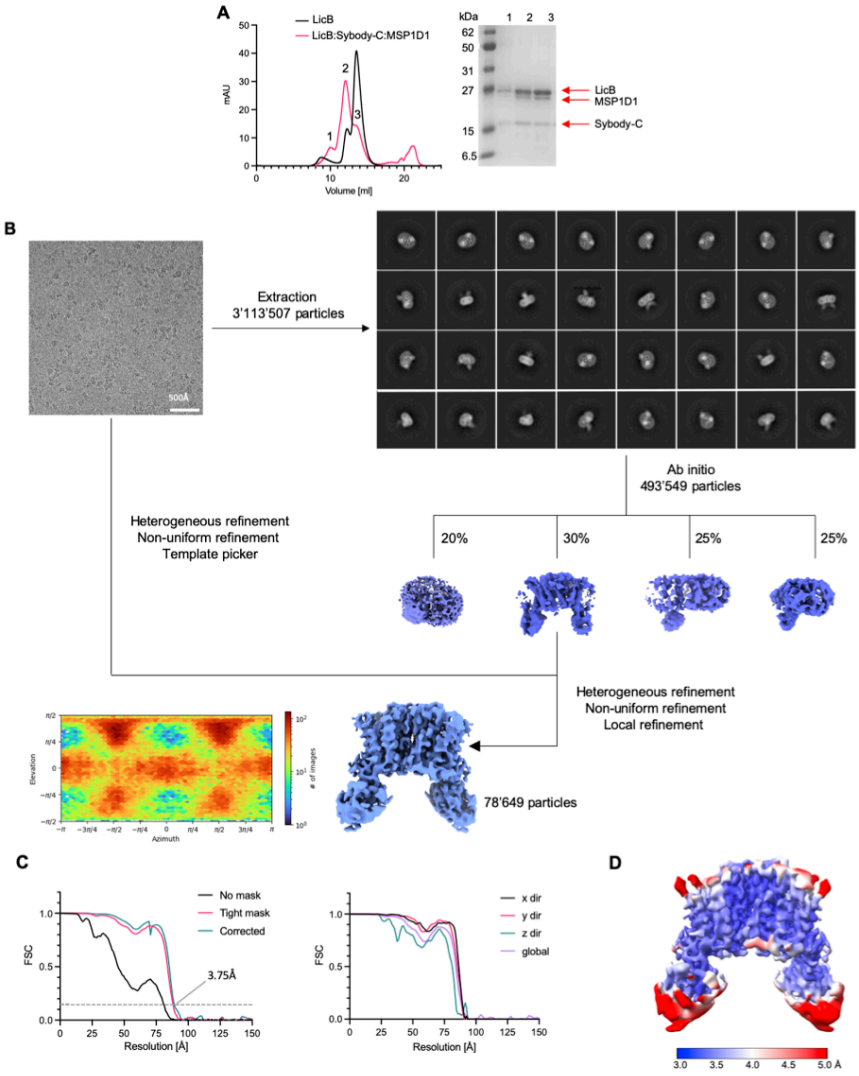

Fig. S8. Cryo-EM reconstruction of LicB-Sybody-C complex in lipid nanodiscs. A. Size exclusion chromatography profiles of LicB and LicB:Sybody-C complex reconstituted in nanodiscs in a Superdex 200 Increase 10/300 column. SDS-PAGE of the three main peaks of the red trace is shown. **B**. Representative micrograph of the complex acquired with a Glacios TEM

equipped with a K3 camera. The data processing workflow shows 2D classes of LicB:Sybody-C:MSP1D1 after particle extraction and multiple rounds of 2D classification and ab initio reconstruction performed with four classes. The particle classes with best protein-like features were used for further rounds of 3D classification, non-uniform refinement, and template generation. The selected particles were later used for a new round of particle picking. Further processing led to a new optimized set of particles used as an input for iterative heterogeneous, non-uniform, and local refinement rounds with C2-symmetry, which yielded a map at a resolution of 3.75 Å. The heatmap displays the number of particles for a given viewing angle. **C**. (*Left*) FSC plots of masked and unmasked maps calculated by cryoSPARC v.3.2.0. Dashed line indicates a 0.143 cut-off. (*Right*) Directional and global FSC plots calculated by the 3DFSC server. The directional FSC curves providing an estimation of anisotropy of the dataset are shown for directions x, y, and z. **D**. Final 3D reconstruction of the LicB:Sybody-C complex colored according to the local resolution, estimated in cryoSPARC v.3.2.0.

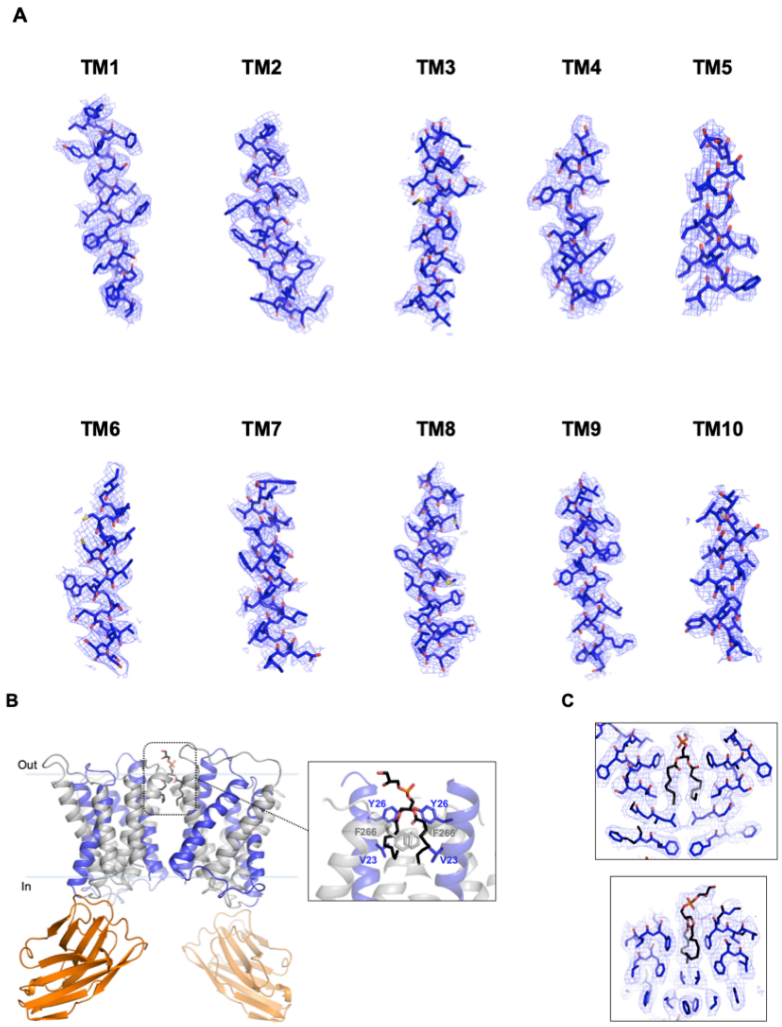

Fig. S9. Cryo-EM densities of LicB segments.

A. Sections of the cryo-EM density superimposed on the refined structure of LicB. **B**. Side view of the LicB homodimer and bound Sybodies. Inverted repeats TM1-5 and TM6-10 in blue and grey, respectively. Sybody-C is shown in orange. The inset shows a putative POPG lipid molecule present at the dimer interface between both protomers. Surrounding residues are shown. **C**. Cryo-EM density (mesh) superimposed on the POPG lipid and surrounding residues.

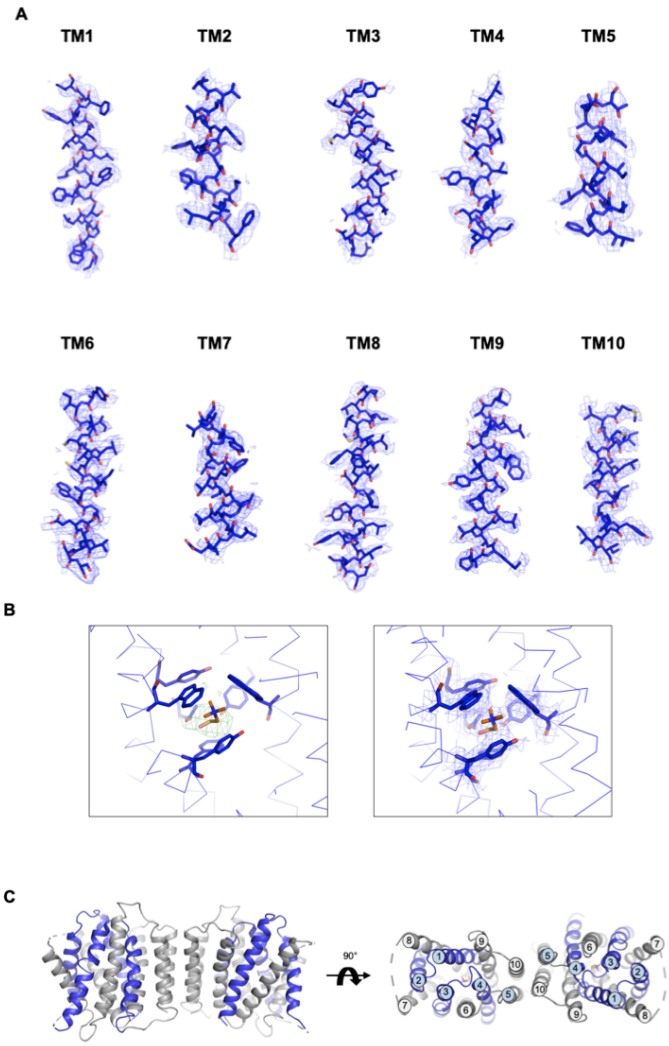

Fig. S10. Crystal structure of LicB.

A. *2Fo-Fc* electron density map of individual TM segments of LicB at 1.0 σ level. **B**. (*Left*) *Fo-Fc* map at 3.0 σ level showing a positive peak at the choline binding site. (*Right*) *2Fo-Fc* electron density map of choline and coordinating residues after refinement. **C**. Packing of two LicB molecules in the crystal lattice, resembling the arrangement of dimers in other DMT transporters.

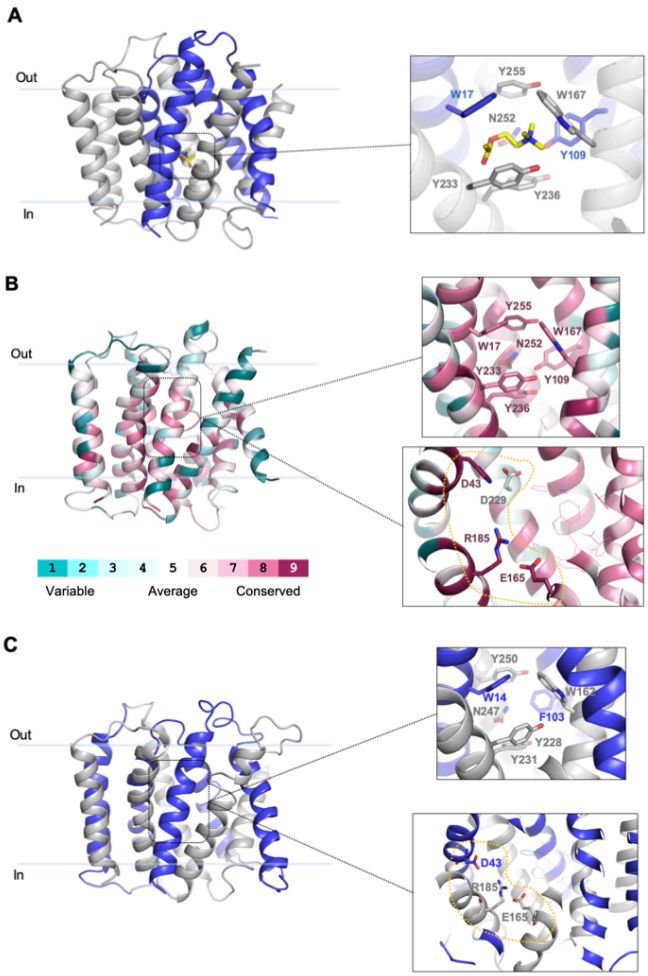

Fig. S11. Docking of acetylcholine and conservation analysis of residues at the choline binding pocket and surrounding charged residues.

A. Docking of acetylcholine in LicB central cavity. Acetylcholine is shown in yellow. **B**. Sequence conservation analysis. A multiple sequence alignment of LicB homologues sharing more than 35% identity was generated and residues in the LicB structure were colored by sequence conservation (ConSurf server). (*Top*) Residues at the Choline binding site. (*Bottom*) Charged residues close to the choline binding site. C. Homology model of *H. influenza* LicB. (*Top*) Residues at the Choline binding. (*Bottom*) Charged residues close to the choline binding site.

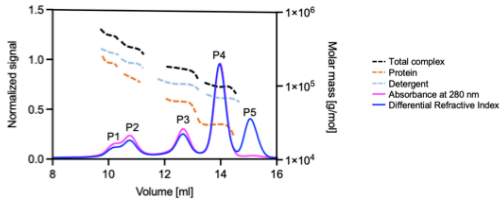

Peak	Molecular weight [kDa]			Interpretation
	Total	Detergent	Protein	
P1	561	329	232	Hexamer
P2	421	257	164	Tetramer
P3	206	131	75	Dimer
P4	125	88	37	Monomer
P5	67	66	1	Empty micelles

Fig. S12. Size exclusion chromatography with multi-angle light scattering (SEC-MALS) analysis of purified LicB in detergent micelles.

Size exclusion profile is plotted as normalized signal and MALS apparent molecular masses of the protein in buffer, detergent in buffer and the total complex with dotted lines (right axis). The molecular weights are summarized in the table with the apparent masses of empty micelles (P5), the monomer (P4, main population), dimer (P3), tetramer (P2) and hexamer (P1).

Table S1.

Oligos used in this study.

Strain	Genotype	Reference
D39V	WT strain of clinical isolate, Serotype 2, parent strain for all strains used in this study unless described	Domenech et al., 2018
VL333	*prs1::PF6-lacI-tetR (gen)*	Sorg et al., 2020
VL1998	*prs1::PF6-lacI (gen), bgaA::Plac-dCas9sp (tet)*	Liu et al., 2017
VL4243	*prsI::PF6-lacI-tetR (gen), bgaA::Plac-licB (tet)*	This study
VL4249	*prsI::PF6-lacI-tetR (gen), bgaA::Plac-licB (tet), zip::Ptet-licB (spc), licB::ery*	Veening collection
VL4250	*prsI::PF6-lacI-tetR (gen), bgaA::Plac-licB-Y233A (tet)*	This study
VL4251	*prsI::PF6-lacI-tetR (gen), bgaA::Plac-licB-Y236A (tet)*	This study
VL4252	*prsI::PF6-lacI-tetR (gen), bgaA::Plac-licB-W17A (tet)*	This study
VL4253	*prsI::PF6-lacI-tetR (gen), bgaA::Plac-licB-W167A (tet)*	This study
VL4254	*prsI::PF6-lacI-tetR (gen), bgaA::Plac-licB-E170A (tet)*	This study
VL4255	*prsI::PF6-lacI-tetR (gen), bgaA::Plac-licB-R191A (tet)*	This study
VL4256	*prsI::PF6-lacI-tetR (gen), bgaA::Plac-licB-H43A (tet)*	This study
Oligo	**Sequence**	**Reference**
R191A_ for	GAAGCCCTCTTAATCGCTCAAGTAACTTCG	This study
R191A_ rev	CGAAGTTACTTGAGCGATTAAGAGGGCTTC	This study
H43A_ for	GTGGCTGCAACTGCTGATTTTTTGAGCATC	This study
H43A_ rev	GATGCTCAAAAAATCAGCAGTTGCAGCCAC	This study
Y233A (gBlock)	GATCCTCAATTGCTAGGTCTCATGATTGTTTTTGCAGCCTTTGATATGATT TCCGCGTTGGCTTATTATATCGCTATCAATCGCTTGCAACCAGCCAAGGCT ACAGGCTTGAACGTGAGCTATGTAGTATGGACGGTCTTGTTTGCAGTTGTT ITCTTGGGTGCACCGCTAGATATGCTGACCATTATGACGTCACTTGTCGTC ATTGCTGGAGTTTATATTATTATTAAAGAATAAGGATCCGATCCT	This study
Y236A (gBlock)	GATCCTCAATTGCTAGGTCTCATGATTGTTTTTGCAGCCTTTGATATGATT TCCTACTTGGCTGCGTATATCGCTATCAATCGCTTGCAACCAGCCAAGGCT ACAGGCTTGAACGTGAGCTATGTAGTATGGACGGTCTTGTTTGCAGTTGTT ITCTTGGGTGCACCGCTAGATATGCTGACCATTATGACGTCACTTGTCGTC ATTGCTGGAGTTTATATTATTATTAAAGAATAAGGATCCGATCCT	This study
N252A (gBlock)	GATCCTCAATTGCTAGGTCTCATGATTGTTTTTGCAGCCTTTGATATGATT TCCTACTTGGCTTATTATATCGCTATCAATCGCTTGCAACCAGCCAAGGCT ACAGGCTTGGCGGTGAGCTATGTAGTATGGACGGTCTTGTTTGCAGTTGTT ITCTTGGGTGCACCGCTAGATATGCTGACCATTATGACGTCACTTGTCGTC ATTGCTGGAGTTTATATTATTATTAAAGAATAAGGATCCGATCCT	This study
W17A (gBlock)	GATCCTCATATGAAAAGTAAAAACGGAGTTCCTTTTGGCCTTCTCTCAGGT ATTTTCGCGGGCTTGGGTCTAACGGTTAGTGCTTATATCTTTTCGATTTTTA CAGATTTGTCACCCTTTGTGGTGGCTGCAACTCATGATTTTTTGAGCATCT TTATCTTACTAGCTTTTCTCTTGGTAAAAGAAGGGAAAGTTCGCCTCTCAA ITTTCTTAAATATTCGCAATGTCAGTGTTATCATCGGAGCCTTGCTAGCGA TCCT	This study
W167A (gBlock)	GATCCTGCTAGCAGGCCCTATCGGTATGCAGGCCAATCTTTATGCAGTTA AGTATATCGGAAGTTCTTTAGCTTCATCTGTATCGGCTATTTACCCTGCGA ITTCAGTTCTATTGGCTTTCTTCTTTTTGAAGCACAAGATTTCGAAAAATA CTGTATTTGGGATTGTCTTGATTATTGGAGGGATTATTGCTCAGACCTATA AGGTTGAACAGGTTAATTCTTTCTACATTGGGATTCTTTGTGCTTTGGTTT GTGCTATTGCAGCGGGAAGTGAGAGTGTTCTTAGCTCTTTTGCCATGGAA AGTGAATTGAGTGAAATCGAAGCCCTCTTAATCCGTCAAGTAACTTCGTT CTTGTCCTATCTTGTGATTGTGCTCTTCTCTCATCAGTCATTTACTGCAGTA GCCAATGGACAATTGGATCCT	This study
E170A (gBlock)	GATCCTGCTAGCAGGCCCTATCGGTATGCAGGCCAATCTTTATGCAGTTA AGTATATCGGAAGTTCTTTAGCTTCATCTGTATCGGCTATTTACCCTGCGA ITTCAGTTCTATTGGCTTTCTTCTTTTTGAAGCACAAGATTTCGAAAAATA CTGTATTTGGGATTGTCTTGATTATTGGAGGGATTATTGCTCAGACCTATA AGGTTGAACAGGTTAATTCTTTCTACATTGGGATTCTTTGTGCTTTGGTTT GTGCTATTGCATGGGGAAGTGCGAGTGTTCTTAGCTCTTTTGCCATGGAA AGTGAATTGAGTGAAATCGAAGCCCTCTTAATCCGTCAAGTAACTTCGTT CTTGTCCTATCTTGTGATTGTGCTCTTCTCTCATCAGTCATTTACTGCAGTA GCCAATGGACAATTGGATCCT	This study
OVL2077	ATTCCTTCTTAACGCCCCAAGTTC	This study
OVL2082	GTCTTCTTTTTTACCTTTAGTAAC	This study
OVL5139	ITAATTCCTTCTTAACGCCCCAAGT	This study

OVL5623	AGCTGTCGTCTCGATAGATCCTTTCTCCTCTTTAGATCTTTTGAATTCGCGGCCG	This study
OVL5624	AGCTGTCGTCTCGCTATGAAAAGTAAAAACGGAGTTCCTTTTGGCCTTCTCTCAG	This study
OVL5625	AGCTGTCGTCTCGCTTATTCTTTAATAATAATATAAACTCCAGCAATGACGACA	This study
OVL5626	AGCTGTCGTCTCGtaaGTCGACCTCGAGACTAGTCAAGGTCGGCAATTCTGCAGTA	This study
OVL5635	AACTCTTTCGACAAATGCGCATCGTCTATCTGAAAATAAC	This study
OVL5636	GAAAATGCTATCCAAATGAT	This study
OVL6035	TAAGGGCGTCTCGCGGAAATCATATCAAAGGCTGCAAAA	This study
OVL6036	TAAGGGCGTCTCCTCCGCATTGGCTTATTATATCGCTATCA	This study
OVL6037	AGTGGTCGTCTCGGCAGCCAAGTAGGAAATCATATCAAAGGCTGCAAAAACAATC	This study
OVL6038	AGTGGTCGTCTCGCTGCATATATCGCTATCAATCGCTTGCAACCAGCCAAGGCTA	This study
OVL6039	GGAATGCGTCTCGGCGAAAATACCTGAGAGAAGGCCAAAAGGAAC	This study
OVL6040	GGAATGCGTCTCGTCGCAGGCTTGGGTCTAACGGTTAGTGCTTAT	This study
OVL6041	GCCATACGTCTCGGCTGCAATAGCACAAACCAAAGCACAGAGAAT	This study
OVL6042	GCCATACGTCTCCCAGCAGGAAGTGAGAGTGTTCTTAGCTCCTTT	This study
OVL6043	CATCCACGTCTCGGCACTTCCCCATGCAATAGCACAAACCAAAGC	This study
OVL6044	CATCCACGTCTCCGTGCAAGTGTTCTTAGCTCCTTTGCTATGGAA	This study
OVL6045	GACAACCGTCTCCGCGATTAAGAGGGCTTCGATTTCACTCAGTTC	This study
OVL6046	GACAACCGTCTCCTCGCACAAGTGACTTCGTTCTTGTCCTATCTT	This study
OVL6047	CTCCTACGTCTCCGCAGTTGCAGCCACCACAAAGGGTGACAAATC	This study
OVL6048	CTCCTACGTCTCCCTGCAGATTTTTTGAGCATCTTTATCTTACTA	This study

3.2 Selection of Transporter-Targeted Inhibitory Nanobodies by Solid-Supported-Membrane (SSM)-Based Electrophysiology

Natalie Bärland[1], Camilo Perez[1]

[1] Biozentrum, University of Basel

Contribution Natalie Bärland: Study design, sample preparation, conduction of experiment, data acquisition, data analysis, writing manuscript.

Journal: Journal of Visualized Experiments: JoVE.

jove

Selection of Transporter-Targeted Inhibitory Nanobodies by Solid-Supported-Membrane (SSM)-Based Electrophysiology

Natalie Bärland[1], **Camilo Perez**[1]

[1] Biozentrum, University of Basel

Corresponding Author

Camilo Perez
camilo.perez@unibas.ch

Citation

Bärland, N., Perez, C. Selection of Transporter-Targeted Inhibitory Nanobodies by Solid-Supported-Membrane (SSM)-Based Electrophysiology. *J. Vis. Exp.* (171), e62578, doi:10.3791/62578 (2021).

Date Published

May 3, 2021

DOI

10.3791/62578

URL

jove.com/video/62578

Abstract

Single domain antibodies (nanobodies) have been extensively used in mechanistic and structural studies of proteins and they pose an enormous potential as tools for developing clinical therapies, many of which depend on the inhibition of membrane proteins such as transporters. However, most of the methods used to determine the inhibition of transport activity are difficult to perform in high-throughput routines and depend on labeled substrates availability thereby complicating the screening of large nanobody libraries. Solid-supported membrane (SSM) electrophysiology is a high-throughput method, used for characterizing electrogenic transporters and measuring their transport kinetics and inhibition. Here we show the implementation of SSM-based electrophysiology to select inhibitory and non-inhibitory nanobodies targeting an electrogenic secondary transporter and to calculate nanobodies inhibitory constants. This technique may be especially useful for selecting inhibitory nanobodies targeting transporters for which labeled substrates are not available.

Introduction

Antibodies are composed of two identical heavy chains and two light chains that are responsible for the antigen binding. Camelids have heavy-chain only antibodies that exhibit similar affinity for their cognate antigen compared to conventional antibodies[1,2]. The single variable domain (VHH) of heavy-chain only antibodies retain the full antigen-binding potential and has been shown to be very stable[1,2]. These isolated VHH molecules or "nanobodies" have been implemented in studies related to membrane proteins biochemistry as tools for stabilizing conformations[3,4], as inhibitors[5,6], as stabilization agents[7], and as gadgets for structure determination[8,9,10]. Nanobodies can be generated by the immunization of camelids for the pre-enrichment of B-cells that encode target-specific nanobodies and subsequent isolation of B cells, followed by cloning of the nanobody library and selection by phage display[11,12,13]. An alternate way to generate nanobodies is based on *in vitro* selection methods that rely on the construction of

libraries and selection by phage display, ribosome display, or yeast display[14,15,16,17,18,19,20]. These *in vitro* methods require large library sizes but benefit from avoiding animal immunization and favor the selection of nanobodies targeting proteins with relatively low stability.

The small size of nanobodies, their high stability and solubility, strong antigen affinity, low immunogenicity, and relatively easy production, make them strong candidates for the development of therapeutics[21,22,23]. In particular, nanobodies inhibiting the activity of multiple membrane proteins are potential assets for clinical applications[5,24,25,26]. In the case of membrane transporters, to evaluate whether a nanobody has inhibitory activity, it is necessary to develop an assay that allows the detection of transported substrates and/or co-substrates. Such assays usually involve labeled molecules or the design of substrate-specific detection methods, which may lack a universal application. Furthermore, the identification of inhibitory nanobodies generally requires the screening of large numbers of binders. Thus, a method that can be used in a high-throughput mode and that does not rely on labeled substrates is essential for this selection.

SSM-based electrophysiology is an extremely sensitive, highly time-resolved technique that allows the detection of movement of charges across membranes (e.g., ion binding/transport)[27,28]. This technique has been applied to characterize electrogenic transporters, which are difficult to study using other electrophysiology techniques due to the relative low turnover of these proteins[29,30,31,32,33,34,35]. SSM electrophysiology does not require the use of labeled substrates, it is suitable for high-throughput screening, and either proteoliposomes or membrane vesicles containing the transporter of interest can be used. Here, we demonstrate that SSM-based electrophysiology can be used to classify transporter-targeted nanobodies with inhibitory and non-inhibitory properties. As a proof-of-principle, we describe the reconstitution of a bacterial choline transporter into liposomes, followed by detailed steps for immobilization of proteoliposomes on the SSM sensors. We next describe how to perform SSM-based electrophysiology measurements of choline transport and how to determine the half-maximal effective concentration (EC_{50}). We then show how to use SSM-based electrophysiology to screen multiple nanobodies and to identify inhibitors of choline transport. Finally, we describe how to determine the half maximal inhibitory concentrations (IC_{50}) of selected inhibitory nanobodies.

Protocol

1. Membrane protein reconstitution

1. Mix 3 mL of *E. coli* polar lipids with 1 mL of phosphatidylcholine in a round bottom flask under a ventilated hood.
2. Dry the lipid mixture for 20 min under vacuum using a rotary evaporator and a water bath at 37 °C to remove chloroform. If needed, dry further under nitrogen or argon gas.
3. Using TS buffer (20 mM Tris-HCl pH 8.0, 150 mM NaCl) containing 2 mM β-mercaptoethanol, resuspend lipids to 25 mg/mL.
4. Aliquot lipids in 500 µL aliquots, flash freeze in liquid nitrogen, and store at -80 °C.
5. Thaw one 500 µL aliquot of lipids and dilute 1:1 using TS buffer containing 2 mM β-mercaptoethanol.
6. Extrude the lipid suspension 15 times using a 400 nm membrane.

7. Dilute the lipid suspension to have a final lipid concentration of 4.4 mg/mL.
8. Add n-dodecyl-β-D-maltoside (DDM) to have a final concentration of 0.2% and leave it rotating for 1 h at 200 rpm at room temperature (RT).
9. Add the purified protein to the lipids using a lipid-to-protein ratio between 1:10 and 1:100 (w:w).
   NOTE: The ratio needs to be adjusted depending on the strength of the signal detected in SSM-electrophysiology measurements of substrate transport (see below). To obtain larger signals, use smaller lipid-to-protein ratios.
10. Incubate the mixture rotating at 200 rpm for 1 h at RT.
11. Add 30 mg/mL of polystyrene adsorbent beads, pre-washed in TS buffer.
    NOTE: Add polystyrene beads stepwise.
12. Incubate the beads-lipids mixture for 30 min at RT under slow stirring.
13. To remove the beads, let the beads-lipids mixture stand so that the beads settle down. Transfer the solution to a new tube and leave the beads behind. Add 30 mg/mL of fresh polystyrene adsorbent beads to the separated lipid mixture.
14. Incubate the mixture for 1 h at 4 °C under slow stirring.
15. Separate the beads from the mixture as described in step 1.13 and add 30 mg/mL of fresh polystyrene adsorbent beads.
16. Incubate the mixture for 16 h at 4 °C.
17. Separate the beads from the mixture as described in step 13 and add 30 mg/mL of fresh polystyrene adsorbent beads.
18. Incubate the mixture for 2 h at 4 °C for a fourth and final wash.
19. Centrifuge at 110,000 x *g* for 30 min at 4 °C.
20. Wash the pellet with 500 µL of TS buffer containing 2 mM β-mercaptoethanol.
21. Centrifuge again at 110,000 x *g* for 30 min at 4 °C.
22. Resuspend the pellet to a final lipid concentration of 25 mg/mL in TS buffer with 2 mM β-mercaptoethanol.
23. Estimate the protein concentration using an in-gel or amido black assay[36].
24. Aliquot the proteoliposomes, flash freeze in liquid nitrogen, and store at -80 °C.

2. Chip preparation

1. Fill a single sensor chip with 50-100 µL of 0.5 mM 1-octadecanethiol solution (resuspended in isopropanol).
2. Incubate the chip with the solution for 30 min at RT.
3. Remove the thiol solution by tapping the chip on a tissue.
4. Rinse the sensor 3 times with 5 mL of pure isopropanol.
5. Rinse the sensor 3 times with 5 mL of double distilled water.
6. Dry the sensor by tapping on a tissue paper.
7. Apply 1.5 µL of 7.5 µg/µL 1,2-diphytanoyl-sn-glycero-3-phosphocholine (lipids dried in a rotatory evaporator and resuspended in n-decane).
8. Immediately after, fill the sensor with 50 µL of non-activating SSM buffer, which does not contain the substrate. This will lead to a spontaneous formation of the SSM layer.
   NOTE: The SSM buffer should be optimized beforehand to determine optimal conditions that have low

background noise. A general buffer containing 30 mM HEPES pH 7.4, 5 mM $MgCl_2$, 140 mM NaCl, can be used as a starting point. The SSM buffer without the substrate is used for washing before and after the measurement (non-activating buffer). To avoid buffer mismatch, use the non-activating buffer to prepare the buffer containing the substrate (activating buffer). The substrate can be added either directly as a powder or in a small volume from a high concentration stock to avoid dilutions.

9. Thaw proteoliposomes from step 1.24 at RT.
10. Dilute proteoliposomes between 1:5 and 1:100 (proteoliposomes:buffer, (v:v)) in the non-activating SSM buffer (here 1:20).
11. Sonicate proteoliposomes for 20-30 s or 3 times for 10 s, placing on ice in between sonication, if necessary. Here a water bath sonicator at 45 kHz was used.
12. Apply 5-10 µL of the diluted sonicated proteoliposomes sample on the surface of the sensor without touching it.
13. Centrifuge the chips with the solution at RT for 30 min using a speed between 2,000 and 3,000 x *g*.
    NOTE: Use 50 mL tubes with a flat bottom. Carefully place the sensor chips upright using tweezers. 6-well plates and a centrifuge with a plate holder can also be used.
14. Use the sensor chips on the same day.

3. Measuring the solute transportation: determination of saturation conditions

NOTE: As proof-of-principle, these experiments were performed using a bacterial choline transporter reconstituted in liposomes following the protocol described above. The step-by-step process of determining saturating conditions of the substrate choline prior to the measurement of inhibition by nanobodies is shown here.

1. Prepare 1-2 L of the non-activating SSM buffer.
   NOTE: Prepare and use the same SSM buffer stock for all activating and non-activating buffers throughout all measurements.
2. Take 10 clean tubes and transfer 10 mL of the non-activating SSM buffer into each.
3. Add the substrate into the tubes from step 3.2 using a series of concentrations around the expected half maximum concentration (here 15, 10, 5, 1, 0.5, 0.1, 0.05, 0.01, 0.005, 0.001 mM of choline) to prepare the activating SSM buffers. Use a high concentration stock to avoid dilutions.
4. Switch on the SSM machine.
5. Start the SSM software and let the machine initialize automatically. Set the saving path for data and confirm by hitting the **OK** button. Select the standard **Initial Cleaning Protocol** in the **workflow** options and click **Run**.
6. Mount the proteoliposome coated chip on the socket, move the arm to lock the chip, and close the mounted chip with the cap.
7. Select the program **CapCom** in the workflow and let it **Run** to determine the conductivity and capacitance. Confirm that the conductivity is below 5 nS and the capacitance is between 15 and 35 nF before using it for the measurement.
   NOTE: A capacitance value of 15-35 nF and conductance below 5 nS are recommended by the manufacturer when using a 3 mm chip.

8. Transfer the activating solutions into vials and position the buffers in the probe sampler.

9. Transfer the non-activating buffer into a reservoir and position it next to the chip holder at the reservoir position on the right.

10. Create a protocol for the workflow using a sequence of non-activating (B), activating (A), and non-activating (B) solutions (B-A-B sequence) and a loop that performs three measurements and moves to the next activating buffer for all 10 buffers prepared in step 3.3. Use the default flow rate at 200 µL/s using 1 s - 1 s - 1 s flow times for the B-A-B sequence. Click **Play** to start the measurement.

    NOTE: A typical experiment consists of the sequential flow of non-activating (B), activating (A), and non-activating (B) solutions (written as B-A-B; see **Figure 1A**). The immobilized proteoliposomes on the sensor will be washed with the solutions. Therefore, the B-A solution exchange generates a substrate concentration gradient, which drives the electrogenic transport reaction.

11. Save the protocol and let the workflow run by clicking on the **Play** button. Perform the same type of experiment but using protein-free liposomes. This is highly important as it would show the intensity of background currents. This should be considered when analyzing data of electrogenic transport measured with proteoliposomes (**Figure 1C**).

12. Use any preferred software for data analysis to plot the measured current versus time. Read out the peak current manually, or if using the software, use the function for peak height estimation in the range of the addition of the activating buffer.

13. Plot the peak current against the substrate concentration to determine the EC_{50} of the substrate via the nonlinear regression (**Figure 1B,C**). Read out the lowest concentration at which the peak current reaches a maximum value, this concentration corresponds to saturating conditions.

    NOTE: It is important to consider that the number of proteoliposomes that remain immobilized varies from chip-to-chip. This variation is evident as the peak currents at identical measurement conditions will show different amplitudes. Therefore, it is necessary to normalize the current amplitudes of measurements performed on each chip separately before comparing measurements among different chip preparations.

4. Serial classification of inhibitory and non-inhibitory nanobodies

NOTE: This section shows how to measure choline transport in the presence of nanobodies that bind specifically to the bacterial choline transporter. Smaller peak currents in the presence of nanobodies indicate transport inhibition. Non-inhibitory nanobodies will not impact substrate transport, i.e., no decrease of the peak current signal.

1. Prepare 1-2 L of non-activating SSM buffer.

2. Transfer 50 mL of the non-activating SSM buffer into a clean tube. Add the substrate choline to a final concentration of 5 mM (saturating conditions). Use this for a positive control measurement.

3. Transfer 10 mL of the non-activating SSM buffer into a clean tube. Add the substrate choline to a final concentration of 5 mM (saturating conditions) and add nanobody to a final concentration of 500 nM.

4. Repeat step 4.3 for each nanobody to prepare the activating solutions.

   NOTE: If the purified nanobodies are resuspended in a different buffer than the SSM buffer, their addition to the activating and non-activating buffers will lead to a buffer mismatch. A buffer mismatch should be avoided since it can lead to high noise. Exchanging the buffer of the purified nanobodies with the SSM buffer can help to avoid this issue. Furthermore, using nanobody concentrations that allow to reach saturating conditions is recommended. Considering that the binding constants of nanobodies are generally below 100 nM, a nanobody concentration of 500 nM is recommended for this experiment. However, it is important to pre-screen for optimal concentrations.

5. Start the SSM machine and measure the capacitance and conductivity of the proteoliposome coated chip as described in steps 3.4-3.7.

6. Transfer the activating solution without a nanobody into a vial and place the buffer in the probe sampler. Transfer the non-activating buffer without a nanobody into a reservoir and position it in the probe sampler.

7. Transfer the activating solutions containing nanobodies into vials and position the buffers in the probe sampler. Transfer the non-activating buffers containing nanobodies into vials and position the buffers in the probe sampler.

8. Create a protocol for the workflow using a sequence of non-activating (B), activating (A), and non-activating (B) solutions (B-A-B sequence).

9. Create a loop that performs the following: three measurements of the B-A-B sequence using buffers without nanobody, two measurements of the B-A-B sequence with buffers containing a nanobody, 120 s delay time for incubation with the nanobody, then 3 measurements of the B-A-B sequence with buffers containing the nanobody.

10. Save the workflow and let it run by clicking the **Play** button.

    NOTE: This workflow will measure the initial conditions of the transport without inhibition by running the B-A-B protocol 3 times using non-activating (B) and activating buffers (A) without the nanobody (**Figure 1B,C**), followed by the measurement of the nanobody effect on the transport by running the B-A-B protocol 5 times with the non-activating and activating buffers containing nanobodies (**Figure 2A**). The second order binding kinetics dictate the interaction of nanobodies and their target proteins. Therefore, it is important to use a time delay in the B-A step in order to give enough time for nanobodies to bind to transporters in proteoliposomes on the chip. Optimal times depend on the nanobody concentration i.e., at lower concentrations longer times are required. The first two measurements are required to adapt the system to the new conditions and the second run should be performed after a delay time of 120 s. Only the following three measurements should be used for data analysis.

11. Create a new protocol for the workflow using a sequence of non-activating (B), activating (A), and non-activating (B) solutions (B-A-B sequence) and a loop of 5 measurements to wash out the reversibly bound nanobody.

    NOTE: Optionally, include an incubation step to allow dissociation of nanobodies with slow kinetics.

12. Save the workflow and let it run by clicking the **Play** button.

13. Compare the last peak current of the measurements with the initial substrate-only measurement in step 4.10. The nanobody has been successfully washed out and the initial conditions have been reestablished if the peak current reaches the initial value, otherwise repeat steps 4.12-4.13 or change to a new chip.
14. Repeat steps 4.6-4.13 and use individual chips for each nanobody screen (**Figure 2C**) or repeat with multiple nanobodies using the same chip (**Figure 2D**).
15. Use any preferred software for data analysis to plot the measured current versus time. Read out the peak current manually, or if available, in the used software, automatically select the function for peak height estimation in the range of the addition of the activation buffer.
16. Normalize the peak current in presence of the nanobody, based on the preceding substrate-only measurement. Plot the peak currents in a histogram and compare the peak currents of the substrate only measurements to the peak currents measured in the presence of nanobodies (**Figure 2C,D**) to identify inhibitory nanobodies.
    NOTE: Normalization of the determined peak currents of each individual run with a nanobody should be performed considering the peak current in the absence of the nanobody from the preceding measurement. Also, since the number of proteoliposomes that remain immobilized vary from chip-to-chip, it is important to normalize the current amplitudes of measurements performed on each chip separately before comparing measurements among different chip preparations.

5. IC_{50} measurement with inhibitory nanobodies

NOTE: After identifying inhibitory nanobodies, it is possible to determine their half maximal inhibitory concentration (IC_{50}). This is done by measuring the transport of choline at constant concentration, while varying concentrations of the inhibitory nanobody.

1. Prepare 1-2 L of the non-activating SSM buffer.
2. Transfer 50 mL of the non-activating SSM buffer into a clean tube. Add the substrate choline to a final concentration of 5 mM (saturating conditions). Use this as the activating solution for positive control.
3. Take 8 clean tubes and add 5 mL of the non-activating solution into each. Add the substrate choline to a final concentration of 5 mM (saturating conditions). Add the inhibitory nanobody to the tubes at concentrations in the expected IC_{50} range (here 500 nM - 1 nM).
4. Take 8 clean tubes and add 10 mL of the non-activating solution into each. Add inhibitory nanobody to each tube individually at the same concentration as in step 5.3. This corresponds to the non-activating buffer.
   NOTE: This will generate a series of activating and non-activating buffer pairs at different concentrations of the same inhibitory nanobody.
5. Start the SSM setup and measure the capacitance and conductivity of the proteoliposome coated chip as described in steps 3.4-3.7.
6. Transfer the activating solution without nanobody into a vial and place it in the probe sampler. Transfer the non-activating buffer without nanobody into a reservoir and position it at the reservoir position next to the chip holder on the right.
7. Transfer the activating solutions containing nanobodies into vials and position the buffers in the probe sampler. Transfer the non-activating buffers containing

nanobodies into vials and position the buffers in the probe sampler.

8. Create a protocol for the workflow using a sequence of non-activating (B), activating (A), and non-activating (B) solutions (B-A-B sequence). Include a loop to measure each concentration 2 times, incubate for 120 s and measure 3 more times. The workflow will start with the positive control of substrate-only followed by the lowest concentration of the nanobody. Each nanobody measurement will be followed by a subsequent measurement of the positive control with substrate-only to restore the initial peak amplitude, before moving to the next higher nanobody concentration.

   NOTE: The second order kinetics dictate the binding of nanobodies. Therefore, it is important to use a time delay in the B-A step. Optimal times depend on the nanobody concentration i.e., at lower concentrations longer times are required; here 120 s was used with satisfactory results.

9. Use any preferred software for data analysis to plot the measured current versus time. Read out the peak current manually, or if using software, select the function for the peak height estimation in the range of the addition of the activation buffer (**Figure 3A**). Plot the peak currents against the nanobody concentration to determine the IC_{50} via non-linear regression (**Figure 3B**).

   NOTE: Normalize the current amplitudes of measurements performed for each individual chip before comparing measurements among different chip preparations.

6. Cleaning of sensors

1. Rinse the single sensor chips after use with 10 mL of distilled water.
2. Dry the chip by tapping it on a tissue paper.
3. Fill the sensor cavity of the chip with 100 µL of pure isopropanol and incubate for 10 min at RT.
4. Place a cotton swab in pure isopropanol and incubate for 1-3 min.
5. Use the presoaked cotton swabs and gently rotate on the sensor's surface without pressure to remove residues.
6. Rinse the sensor with 5 mL of pure isopropanol.
7. Rinse the sensor with 10 mL of distilled water.
8. Dry the sensor by tapping the chip on a tissue.
9. Let the sensor dry overnight at RT, and store at RT under dry conditions.

   NOTE: Sensors can be re-used up to 4-5 times when cleaned and stored properly.

Representative Results

SSM-based electrophysiology has been extensively used for the characterization of electrogenic transporters. In the protocol presented here, we show how to use SSM-based electrophysiology to classify nanobodies targeting a secondary transporter (here a bacterial choline symporter) based on their inhibitory and non-inhibitory properties. One of the most useful features of this technique is that it allows for the high-throughput screening of multiple buffer conditions. This particular characteristic is beneficial for the analysis of nanobody libraries, which after the selection of binders can be constituted from a few to dozens of nanobodies. In a standard experiment, a stable lipid monolayer is assembled on a sensor chip. After applying the proteoliposomes preparation containing the choline transporter, a check for good conductivity and capacitance is performed as this is essential for the success of the experiment. In case that the integrity of

the membrane is compromised during an experiment, which is easily observed due to the high noise background currents, changing to a new chip is recommended as recovering low noise conditions is rather difficult. In general, we have observed very good reproducibility among measurements of transport and inhibition by nanobodies when using different chips.

To decide about the substrate concentration to be used during a screening of nanobodies, electrogenic transport was first measured under different substrate concentrations to determine EC_{50} (**Figure 1B,C**). A substrate concentration that corresponds to saturating conditions was selected (**Figure 1C**). This substrate concentration was then kept constant in all activating buffers. For this particular example, we selected 5 mM choline.

For the screening of nanobodies, the nanobody must be added to both non-activating and activating buffers. When nanobodies were added to only the activating buffer, it was not possible to observe inhibition of the electrogenic transport. We speculate that this is due to an incomplete occupation of all nanobody binding sites in the transporter population on the chip, thereby revealing the importance of pre-incubation with nanobodies in non-activating conditions. To ensure that all sites are likely to be occupied, a time delay step was included during the application of the first non-activating buffer step to allow the saturation of nanobody binding sites on the transporter population. Incubation times ranging from 2-60 min have been tested with reproducible results. Keep in mind that optimal times of incubation depend on the nature of the nanobody binder and its concentration during the experiment (as well as the concentration of transporter in proteoliposomes on the chip). Therefore, it is recommended to try different incubation times. In any case, as a rule of thumb, the lower the nanobody concentration, the longer the incubation time required. We tested incubation times of 2 min, 20 min, 30 min, and 60 min for different nanobodies but did not detect further transport inhibition.

The effect of inhibitory nanobodies on electrogenic transport is visualized from the decrease of peak currents amplitudes (**Figure 2A,C,D**). Non-inhibitory nanobodies, on the other hand, do not affect peak currents. After running the washing protocol to allow nanobodies unbinding, a recovery of 80 to 95% of the initial peak current amplitude was observed (**Figure 2A,C,D**). We have performed a similar experiment but in the presence of liposomes without the transporter protein. When changing from non-activating to activating conditions, no significant artifact currents was introduced by nanobodies present in these buffers (**Figure 2B**). Running this control experiment is recommended as it is important to know whether changes in peak currents arise from artifacts or not.

After the selection of nanobodies with inhibitory properties, we determined IC_{50} values for individual nanobodies (**Figure 3A,B**). For this particular experiment, it is recommended to start with a low concentration of nanobodies and then move towards high concentration during the assay. The calculation of the inhibition for each concentration was then performed by comparing peak currents measured before and after the application of nanobody. To avoid unspecific binding of nanobodies to surfaces, which can be particularly problematic when using low nanobody concentrations, it is advised to follow a similar protocol to that described by Kermani et al.[37], where 50 µg/mL of bovine serum albumin was added to the buffers, preventing this deleterious effect. Adding detergents such as Tween or Triton for this purpose should be avoided as these would dissolve lipid membranes.

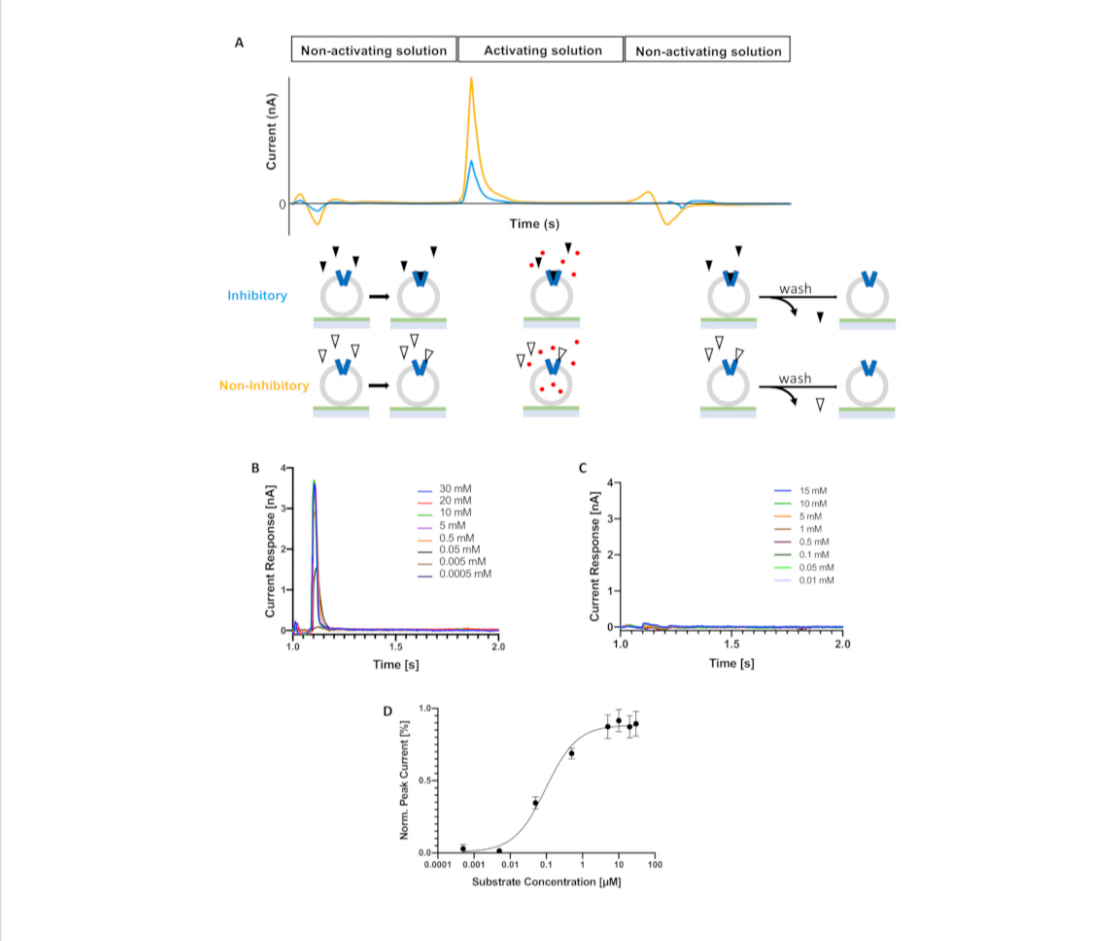

Figure 1: SSM-based electrophysiology. (**A**) Protocol for transient currents measurement. A non-activating solution is replaced by an activating solution followed by the flow of non-activating solution to restore initial conditions. During the first step, nanobodies bind to the transporter. When switching to the activating solution, the substrate gradient drives the electrogenic transport (orange curve). In the presence of an inhibitory nanobody, the peak current shows a smaller amplitude (blue curve). After finishing the protocol and running solutions without nanobody (wash), unbinding of nanobodies occurs. In the schematic, proteoliposomes with reconstituted protein (blue) are immobilized on the SSM sensor. Triangles and red circles represent nanobodies and substrate, respectively. (**B**) Electrogenic choline transport in the absence of nanobodies. Peak currents measured during activating conditions are shown for different substrate concentrations. (**C**) Representative measurement of currents during activating conditions in the absence of transporter protein at different

substrate concentrations. (**D**) Plot of substrate concentration versus peak currents amplitude. The EC_{50} determined was 95 ± 11 µM choline. Error bars indicate standard deviation (n=3 biological replicates, n=3 technical replicates). Please click here to view a larger version of this figure.

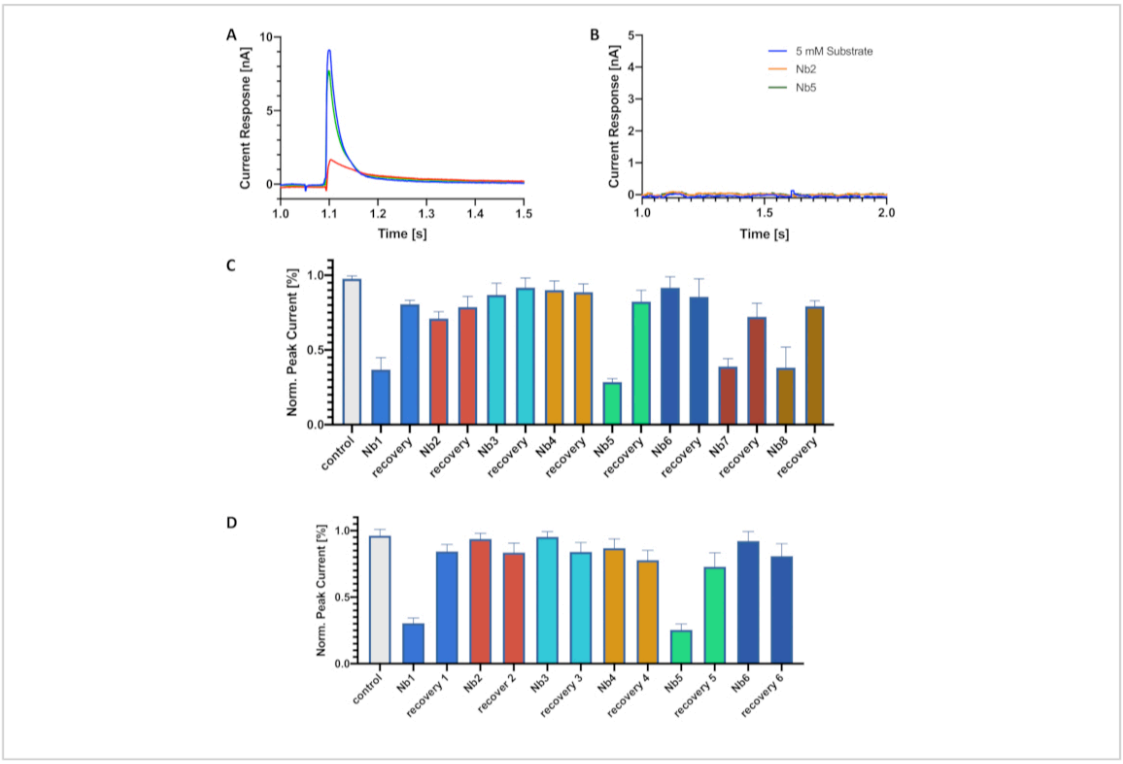

Figure 2: Screening and classification of inhibitory and non-inhibitory nanobodies. (**A**) Electrogenic choline transport in the presence of a nanobody. Peak currents measured during activating conditions are shown in the absence of nanobody (blue), in the presence of an inhibitory nanobody (red), and after nanobody unbinding (green). (**B**) Measurement of currents during activating conditions in the absence of transporter protein. Traces show recordings in the absence of nanobody (blue), in the presence of an inhibitory nanobody (green), and in the presence of a non-inhibitory nanobody (red). (**C,D**). Histograms showing peak currents measured during activating conditions in the presence of nanobodies and after nanobody unbinding (recovery). Panel **C** shows the results of measurements using individual chips per nanobody. Panel **D** shows the results from a serial measurement using one chip. Nanobodies are indicated as Nb. Error bars indicate the standard deviation (n=3 biological replicates, n=2 technical replicates). Please click here to view a larger version of this figure.

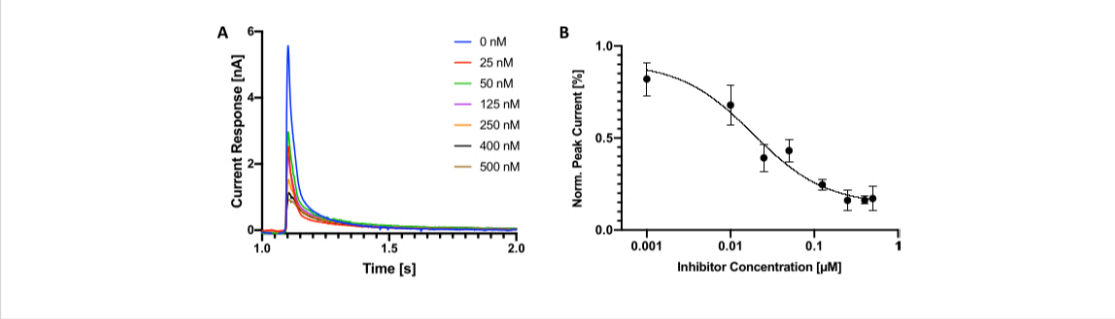

Figure 3: Determination of IC_{50} of an inhibitory nanobody. (**A**) Electrogenic choline transport and inhibition by a nanobody. Peak currents measured during activating conditions are shown for different nanobody concentrations. (**B**) Plot of peak currents amplitude vs nanobody concentration from a serial measurement with an inhibitory nanobody. The IC_{50} determined was 18 ± 2 nM. Error bars indicate the standard deviation (n=3 biological replicates, n=3 technical replicates). Please click here to view a larger version of this figure.

Discussion

The technique presented here classifies nanobodies with inhibitory and non-inhibitory properties targeting electrogenic transporters. Assessing the substrate transport is possible due to the detection of the movement of charges through the transporter embedded in the membrane of proteoliposomes. Some of the critical steps during the setup of an experiment are reconstitution of active protein in liposomes, preparation of stable monolayers on SSM chips, and recovering of initial conditions after the application of the wash protocol to remove bound nanobody molecules. Once the membrane protein is reconstituted at an appropriate lipid-to-protein ratio, a general SSM protocol can be established using the native substrate. It is crucial to perform control experiments using protein-free liposomes to reveal noise currents that would need to be subtracted from the currents measured using proteoliposomes. However, if noise currents are too large, we recommend trying protein reconstitution using different lipids, or screen for buffer conditions that minimize these deleterious signals. After successfully establishing conditions for an SSM assay, screening of nanobodies can be performed. A very useful option that may help in faster screening of nanobodies is to perform high-throughput assays using a single SSM sensor chip. This reduces the time of manipulation of chips and buffers and reduces the costs. However, because during this type of assay multiple nanobodies are applied sequentially, it is important to ensure that the applied nanobody can be washed away after the measurement. A stringent washing cycle may need to be implemented to unbind some nanobodies in case that reduced peak current amplitudes are detected in the absence of nanobody. We recommend using, as the starting point, the washing conditions described here. If increasing the washing volume or the number of cycles does not help, individual chips would need to be used to screen each nanobody separately. In all the cases examined here, the binding of nanobodies was reversible and a high-throughput protocol could be applied. In our experimental setup, we could not recover the full

amplitude of the initial peak current after measurements with nanobodies (**Figure 1A; Figure 2C,D**). However, in most cases, the magnitude of the peak currents recovered ranged between 80 and 95% of the amplitude measured before applying nanobodies (**Fig. 2C,D**). We speculate that this could be a consequence of washing away a fraction of the proteoliposomes adhered to the chip, or due to slow kinetics of unbinding of some inhibitory nanobodies, or a combination of both. In either case, it was still possible to continue assaying further nanobodies as electrogenic transport was measurable. This is shown in **Figure 2D**, where we screened six nanobodies using a single chip preparation.

The high-throughput characteristic is one of the most significant advances of the method presented. In addition, in contrast to other approaches, this method allows for the selection of inhibitory nanobodies targeting electrogenic transporters for which labeled substrates are not available. A fast identification of inhibitory nanobodies can help to speed up the research aiming to identify novel applications of nanobodies as drugs. Their apparent advantages compared to similar therapies such as antibody treatments are numerous, starting with a smaller size which helps them propagate further into tissues or cells, to their low production costs and high stability.

SSM-based electrophysiology has been used in the past for the characterization of electrogenic transporters in membrane vesicles[29,38]. These types of experiments are advantageous as they do not depend on the protein purification and reconstitution protocols. We speculate that performing the selection of inhibitory nanobodies using membrane vesicles is feasible. This would help to reduce costs and avoid manipulations of purified proteins.

SSM-based electrophysiology is a strong technique to screen for nanobody inhibitors of multiple membrane proteins that exhibit electrogenic transport. We envision that SSM-based electrophysiology will become an important tool for the selection of inhibitory nanobodies and other antibodies with potential clinical applications.

Disclosures

The authors declare no competing financial interests.

Acknowledgments

We thank Cedric A. J. Hutter and Markus A. Seeger from the Institute of Medical Microbiology at the University of Zurich, and Gonzalo Cebrero from Biozentrum of the University of Basel for collaboration in the generation of synthetic nanobodies (sybodies). We thank Maria Barthmes and Andre Bazzone from NANION Technologies for technical assistance. This work was supported by the Swiss National Science Foundation (SNSF) (PP00P3_170607 and NANION Research Grant Initiative to C.P.).

References

1. Braden, B. C., Goldman, E. R., Mariuzza, R. A., Poljak, R. J. Anatomy of an antibody molecule: structure, kinetics, thermodynamics, and mutational studies of the antilysozyme antibody D1.3. *Immunology Reviews.* **163**, 45-57 (1998).
2. Hamers-Casterman, C. et al. Naturally occurring antibodies devoid of light chains. *Nature.* **363**, 446-448 (1993).
3. Perez, C. et al. Structural basis of inhibition of lipid-linked oligosaccharide flippase PglK by a conformational nanobody. *Science Reports.* **7**, 46641 (2017).

4. Grahl, A., Abiko, L.A., Isogai, S., Sharpe, T., Grzesiek, S. A high-resolution description of beta1-adrenergic receptor functional dynamics and allosteric coupling from backbone NMR. *Nature Communication.* **11**, 2216 (2020).
5. Schenck, S. et al. Generation and characterization of anti-VGLUT nanobodies acting as inhibitors of transport. *Biochemistry.* **56**, 3962-3971 (2017).
6. Mireku, S. A., Sauer, M. M., Glockshuber, R., Locher, K.P. Structural basis of nanobody-mediated blocking of BtuF, the cognate substrate-binding protein of the Escherichia coli vitamin B12 transporter BtuCD. *Science Reports.* **7**, 14296 (2017).
7. Manglik, A., Kobilka, B. K., Steyaert, J. Nanobodies to study G protein-coupled receptor structure and function. *Annual Reviews of Pharmacology Toxicology.* **57**, 19-37 (2017).
8. Rasmussen, S. G. et al. Structure of a nanobody-stabilized active state of the beta(2) adrenoceptor. *Nature*. **469**, 175-80 (2011).
9. Jiang, X. et al. Crystal structure of a LacY-nanobody complex in a periplasmic-open conformation. *Proceeding of the National Academy of Science U. S. A.* **113**, 12420-12425 (2016).
10. Geertsma, E. R. et al. Structure of a prokaryotic fumarate transporter reveals the architecture of the SLC26 family. *Nature Structural Molecular Biology*. **22**, 803-808 (2015).
11. Harmsen, M. M., De Haard, H. J. Properties, production, and applications of camelid single-domain antibody fragments. *Applied Microbiology and Biotechnology.* **77**, 13-22 (2007).
12. Pardon, E. et al. A general protocol for the generation of nanobodies for structural biology. *Nature Protocols.* **9**, 674-93 (2014).
13. Nguyen, V. K., Desmyter, A., Muyldermans, S. Functional heavy-chain antibodies in Camelidae. *Advances in Immunology.* **79**, 261-296 (2001).
14. Zimmermann, I. et al. Synthetic single domain antibodies for the conformational trapping of membrane proteins. *Elife.* **7**, e34317(2018).
15. McMahon, C. et al. Yeast surface display platform for rapid discovery of conformationally selective nanobodies. *Nature Structural Molecular Biology.* **25**, 289-296 (2018).
16. Olichon, A., de Marco, A. Preparation of a naive library of camelid single domain antibodies. *Methods in Molecular Biology.* **911**, 65-78 (2012).
17. Moutel, S. et al. NaLi-H1: A universal synthetic library of humanized nanobodies providing highly functional antibodies and intrabodies. *Elife*. **5**, e16228 (2016).
18. Yan, J., Li, G., Hu, Y., Ou, W., Wan, Y. Construction of a synthetic phage-displayed nanobody library with CDR3 regions randomized by trinucleotide cassettes for diagnostic applications. *Journal of Translational Medicine*. **12**, 343 (2014).
19. Sabir, J. S. et al. Construction of naive camelids VHH repertoire in phage display-based library. *Comptes Rendus Biologies*. **337**, 244-249 (2014).
20. Yau, K. Y. et al. Selection of hapten-specific single-domain antibodies from a non-immunized llama ribosome display library. *Journal of Immunology Methods*. **281**, 161-175 (2003).

21. van der Linden, R.H. et al. Comparison of physical chemical properties of llama VHH antibody fragments and mouse monoclonal antibodies. *Biochimica et Biophysica Acta.* **1431**, 37-46 (1999).
22. Dumoulin, M. et al. Single-domain antibody fragments with high conformational stability. *Protein Science.* **11**, 500-515 (2002).
23. Iezzi, M. E., Policastro, L., Werbajh, S., Podhajcer, O., Canziani, G. A. Single-domain antibodies and the promise of modular targeting in cancer imaging and treatment. *Frontiers in Immunology.* **9**, 273 (2018).
24. Yu, X. et al. Nanobodies derived from camelids represent versatile biomolecules for biomedical applications. *Biomaterials Science.* **8**, 3559-3573 (2020).
25. Jahnichen, S. et al. CXCR4 nanobodies (VHH-based single variable domains) potently inhibit chemotaxis and HIV-1 replication and mobilize stem cells. *Proceedings of the National Academy of Science U. S. A.* **107**, 20565-70 (2010).
26. Nguyen, V. S. et al. Inhibition of type VI secretion by an anti-TssM llama nanobody. *PLoS One.* **10**, e0122187 (2015).
27. Bazzone, A., Barthmes, M., Fendler, K. SSM-Based Electrophysiology for Transporter Research. *Methods in Enzymology.* **594**, 31-83 (2017).
28. Schulz, P., Garcia-Celma, J. J., Fendler, K. SSM-based electrophysiology. *Methods.* **46**, 97-103 (2008).
29. Barthmes, M., Liao, J., Jiang, Y., Bruggemann, A., Wahl-Schott, C. Electrophysiological characterization of the archaeal transporter NCX_Mj using solid supported membrane technology. *Journal of General Physiology.* **147**, 485-96 (2016).
30. Watzke, N., Diekert, K., Obrdlik, P. Electrophysiology of respiratory chain complexes and the ADP-ATP exchanger in native mitochondrial membranes. *Biochemistry.* **49**, 10308-10318 (2010).
31. Zuber, D. et al. Kinetics of charge translocation in the passive downhill uptake mode of the Na+/H+ antiporter NhaA of Escherichia coli. *Biochim Biophys Acta.* **1709**, 240-250 (2005).
32. Garcia-Celma, J. J., Smirnova, I. N., Kaback, H. R., Fendler, K. Electrophysiological characterization of LacY. *Proceedings of the National Academy of Science U. S. A.* **106**, 7373-7378 (2009).
33. Bazzone, A., Madej, M. G., Kaback, H. R., Fendler, K. pH regulation of electrogenic sugar/H+ symport in MFS sugar permeases. *PLoS One.* **11**, e0156392 (2016).
34. Williamson, G. et al. A two-lane mechanism for selective biological ammonium transport. *Elife.* **9**, e57183 (2020).
35. Mirandela, G. D., Tamburrino, G., Hoskisson, P. A., Zachariae, U., Javelle, A. The lipid environment determines the activity of the Escherichia coli ammonium transporter AmtB. *FASEB Journal.* **33**, 1989-1999 (2019).
36. Kaplan, R. S., Pedersen, P. L. Determination of microgram quantities of protein in the presence of milligram levels of lipid with amido black 10B. *Annals of Biochemistry.* **150**, 97-104 (1985).
37. Kermani, A. A. et al. The structural basis of promiscuity in small multidrug resistance transporters. *Nature Communication.* **11**, 6064 (2020).
38. Weitz, D. et al. Functional and structural characterization of a prokaryotic peptide transporter with features similar

to mammalian PEPT1. *Journal of Biological Chemistry.* **282**, 2832-9 (2007).

3.3 Fast Small-Scale Membrane Protein Purification and Grid Preparation for Single-Particle Electron Microscopy

Natalie Bärland[1], Camilo Perez[1]

[1] Biozentrum, University of Basel

Contribution: Contribution of study design, conduction of proof of concept experiment, data acquisition and analysis, writing manuscript.

Journal: Expression, Purification, and Structural Biology of Membrane Proteins, Humana, New York, NY. Part in Methods of Molecular Biology book series.

Chapter 18

Fast Small-Scale Membrane Protein Purification and Grid Preparation for Single-Particle Electron Microscopy

Natalie Bärland and Camilo Perez

Abstract

The ongoing development of single-particle cryo-electron microscopy (cryo-EM) is leading to fast data acquisition, data processing, and protein structure elucidation. Quick and reliable methods to go from protein purification and optimization to grid preparation will significantly improve the reach and power of cryo-EM. Such methods would particularly constitute a tremendous advantage in structural biology of membrane proteins, whose published structures stay still far behind the number of soluble protein structures. Here we describe a fast, low-cost, and user-friendly method for the purification and cryo-EM analysis of a recombinant membrane protein. This method minimizes the amount of starting material and manipulation steps needed to go from purification to grid preparation, and could potentially be expanded to other membrane protein purification systems for its direct application in structure determination by single-particle cryo-EM.

Key words Membrane proteins, Affinity-chromatography, Small-scale purification, Single-particle electron microscopy, Negative staining-EM, Cryo-EM

1 Introduction

The study of the structure and function of membrane proteins, which make up to nearly a third of the genome in eubacteria, archaea, and eukaryotes [1], is paved with multiple challenges. Membrane proteins have a broad variety of functions as transporters, channels, receptors, or enzymes, and are targeted by more than 50% of the marketed drugs [2, 3]. Recent developments in the field of single-particle cryo-EM have boosted the number of elucidated membrane protein structures. Higher sensitivity of direct detectors [4, 5], phase plates for contrast enhancement [6], implementation of graphic processor units for accelerated calculations [7], refined algorithms, and simplified software [8–10] speed up processes involved in data acquisition and processing. The bottleneck in high-throughput structural biology remains to be sample

Camilo Perez and Timm Maier (eds.), *Expression, Purification, and Structural Biology of Membrane Proteins*, Methods in Molecular Biology, vol. 2127, https://doi.org/10.1007/978-1-0716-0373-4_18,

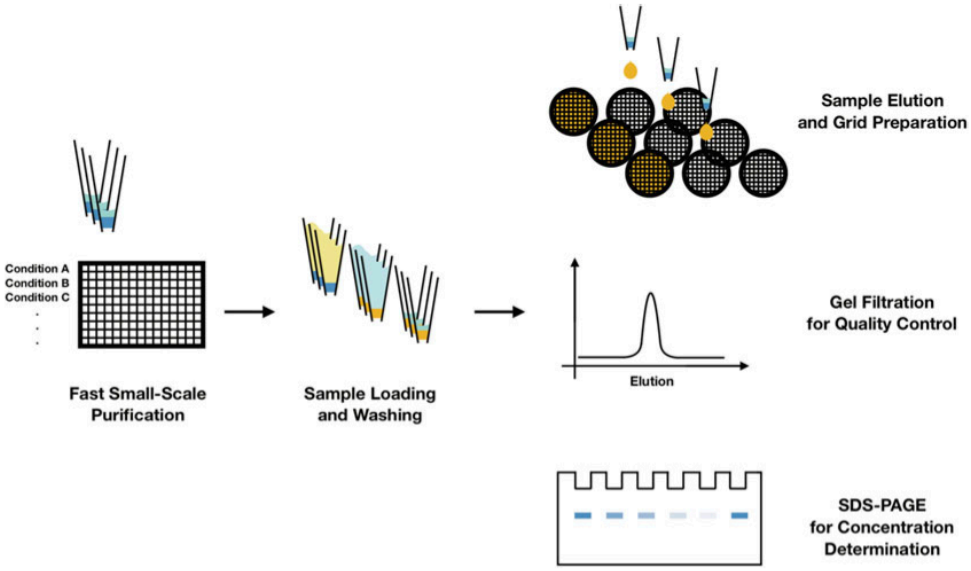

Fig. 1 Principle of the fast small-scale purification for single-particle EM (FASSP-EM) methodology. Low amounts of solubilized membrane protein[s] are distributed in a 96-well plate. Affinity chromatography using PureSpeed™ IMAC tips allows for quick protein loading and washing. The protein(s) of interest can be directly eluted on a glow-discharged grid for analysis by single-particle EM, analyzed via gel filtration and/or SDS-PAGE

preparation including refined methods in protein purification and grid preparation [11–14].

To meet the need of fast sample production of recombinant membrane proteins with minimal material usage and reduced cost, we present a fast small-scale method that uses PureSpeed™ IMAC tips and 96-well plates for purification, parallel buffer condition screening, and grid preparation for application to single-particle EM (Fig. 1). The advantage of parallelized purification is that it allows screening multiple stabilizing agents (e.g., detergents, protein binders, additives) and fast assessment of conditions targeted to trap particular conformations, and it facilitates working with multiple protein targets at the same time. In the current protocol, as *proof of principle* we perform the purification and EM analysis of a membrane protein linked to a poly-histidine tag. However, the method could be extended to purification of proteins with other affinity tags. The membrane protein studied here corresponds to the ATP-binding cassette (ABC) flippase PglK, a 130 kDa protein from *Campylobacter jejuni* [15].

2 Materials

2.1 Membrane Preparation and Purification

1. Centrifuge Sorvall LYNX 6000 (Thermo Fisher).
2. Microfluidizer LM10 (Microfluidics).
3. Rotor 70 Ti (Beckmann Coulter).
4. Rotor Fiberlite F9-6 × 1000 LEX Fixed Angle Rotor (Thermo Fisher).
5. Ultracentrifuge Optima XE-90 (Beckmann Coulter).
6. PureSpeed™ IMAC Tips 1 ml with 80 µl resin bed volume (Mettler Toledo).
7. Pyrex Dounce tissue grinder 40 ml (SciLabware).
8. Cell solubilisation buffer (CS), 50 mM Tris–HCl pH 8.0, 500 mM NaCl, 7 mM β-mercaptoethanol, 0.5 mM PMSF.
9. Membrane resuspension buffer (MR), 50 mM Tris–HCl pH 8.0, 500 mM NaCl, 7 mM β-mercaptoethanol.
10. Equilibration buffer (EQ), 50 mM Tris–HCl pH 8.0, 500 mM NaCl, 20 mM imidazole pH 8.0, 10% glycerol, 0.016% DDM, 7 mM β-mercaptoethanol.
11. Solubilisation buffer (SB), 50 mM Tris–HCl pH 8.0, 500 mM NaCl, 20 mM imidazol pH 8.0, 15% glycerol, 1% DDM, 1% $C_{12}E_8$, 7 mM β-mercaptoethanol.
12. Washing buffer (WB-1), 50 mM Tris–HCl pH 8.0, 500 mM NaCl, 50 mM imidazole pH 8.0, 10% glycerol, 0.016% DDM, 7 mM β-mercaptoethanol.
13. Washing buffer (WB-2), 50 mM Tris–HCl pH 8.0, 500 mM NaCl, 50 mM imidazole pH 8.0, 2% glycerol, 0.016% LMNG, 7 mM β-mercaptoethanol.
14. Elution buffer (EL), 50 mM Tris–HCl pH 8.0, 500 mM NaCl, 50 mM imidazole pH 8.0, 0.016% LMNG, 7 mM β-mercaptoethanol.

2.2 Electron Microscopy

1. FEI Talos TEM 200 kV transmission electron microscope (TEM) (FEI).
2. Lacey carbon grid mesh 400 copper grids (Electron Microscopy Sciences).
3. Leica EM GP plunge freezer (Leica Microsystems).
4. Tecnai G2 Spirit 120 kV TEM (FEI).
5. TG100/400 copper palladium rectangular mesh TEM carbon-coated grids.
6. Whatman™ Grade 556 dry pads (GE Healthcare).
7. Whatman™ Grade 1 circles (GE Healthcare).
8. 2% Uranyl acetate, kept away from light.

2.3 Software for Data Analysis

1. CTF4 [16].
2. ImageJ [17].
3. Relion 3.0 [8].
4. Origin (OriginLab Corp).

3 Methods

Protocols for expression need to be optimized separately. Samples and buffers should be pre-cooled at 4 °C. It is recommended to carry out the purification at 4 °C. Data acquisition for single-particle EM and data processing will not be discussed here.

3.1 Membrane Preparation and Purification of Recombinant Membrane Protein

1. Resuspend cell pellet in CS buffer using 8 ml buffer per 1 g cell dry weight. Let the solution stir at 4 °C until it is fully homogenized.
2. Disrupt cells using a Microfluidizer at 10,000 bar. Let the homogenized solution pass two times to break all cells.
3. Spin the disrupted cells at 4400 × *g* for 30 min at 4 °C in a pre-cooled rotor.
4. Spin the supernatant at 142,400 × *g* for 30 min at 4 °C.
5. Resuspend the pellet containing the membranes in MR buffer using 1 ml buffer for 1 g initial cell dry weight.
6. Aliquot membranes by 2.5 ml and flash freeze with liquid nitrogen. Store at −80 °C until further use.
7. Solubilize membranes in 6 ml SB buffer by stirring at 4 °C for 2 h.
8. Spin the solubilized sample at 29,600 × *g* and recover the supernatant.
9. Equilibrate a 1 ml PureSpeed™ IMAC tip with 80 µl resin volume with 2 × 1 ml equilibration buffer (*see* **Note 1**).
10. Load 2 × 1 ml supernatant on the equilibrated tip.
11. Wash two times with 1 ml WB-1.
12. Wash two times with 1 ml WB-2 (*see* **Note 2**).
13. Elute with 130 µl elution buffer by pipetting up and down four times. This facilitates to recover higher protein amounts (*see* **Note 3**) (Fig. 2a).
14. **Steps 9–13** can be carried out in parallel for other protein samples using a multichannel pipette or done individually with a regular pipette.

3.2 Determination of Protein Concentration

Due to the high absorbance of imidazole at 280 nm, using standard spectroscopy methods for the determination of protein

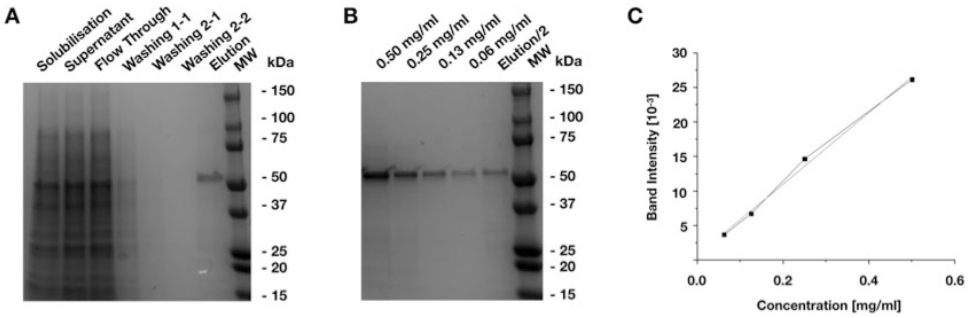

Fig. 2 SDS-PAGE analysis and protein concentration determination of FASSP-EM-purified PglK. (**a**) Gels were loaded with 7.5 μl of eluted PglK premixed with 2.5 μl of 4× loading dye. The standard molecular weight (MW) is indicated. The lane containing the eluted sample exhibits a strong band between 50 and 75 kDa, representing the expected molecular weight of the PglK monomer (65 kDa). (**b**) SDS-PAGE of PglK at known concentrations was used to generate a calibration curve. Elution corresponds to a twofold dilution of the eluted sample. (**c**) Plot of concentration against band intensity determined with ImageJ. The red line indicates a linear fit. The concentration estimated for the eluted protein is 0.4 mg/ml

concentration in the eluate is not recommended. To estimate protein concentration, we use SDS-PAGE and analysis with ImageJ to generate a calibration curve.

1. Prepare 10 μl protein dilutions of protein at known concentration [0.5 and 0.01 mg/ml] to use as standards for SDS-PAGE analysis. Load dilutions on the same gel as the eluted samples from the purification (Fig. 2b).
2. Take a picture of the gel for analysis in ImageJ and first adjust brightness and contrast in the drop-down menu Image > Adjust > Brightness/Contrast.
3. Select the first protein band on the gel with the rectangular tool and in the drop-down menu select Analyze > Gels > Select First Lane.
4. Move new rectangle to the next protein band and select Analyze > Gels > Select Next Lane. Repeat for all protein bands.
5. Select Analyze > Gels > Plot Lanes to calculate the profile of the density on the image and draw a baseline with the line tool to have a closed area.
6. Calculate the areas enclosed with the magic wand tool by clicking inside the profiles.
7. Plot the band intensities against the concentration of the protein in your program of choice and perform a linear fit (Fig. 2c).
8. Estimate protein concentration in the eluate using the calibration curve equation derived from the previous step.

3.3 Negative Staining EM

1. Prepare a series of dilutions of the eluted protein between 1:10 and 1:50 to be used for preparation of negative staining grids.
2. Load 5 μl of protein sample on a glow-discharged carbon-coated mesh 400 palladium grid and incubate for 1 min.
3. Wash three times with 20 μl ddH2O and blot with filter paper (*see* **Note 4**).
4. Wash one time with 5 μl 2% uranyl acetate and blot with filter paper.
5. Stain with 5 μl 2% uranyl acetate, incubate for 10–15 s, and blot with filter paper.
9. Examine grids and collect images in a transmission electron microscope (Fig. 3a, b). In this case we used a Tecnai G2 Spirit 120 kV TEM.

3.4 Plunge Freezing of Purified Sample for Cryo-EM Analysis

1. Start up the Leica plunge freezer according to the manual and cool down the instrument with liquid nitrogen and the plunge freezing bath with liquid ethane. Place a new Whatman blotting paper grade 1 and adjust the settings to 80% humidity in the chamber.
2. Place a freshly glow-discharged Lacey carbon grid on the Leica tweezers.
3. Apply 5 μl of the non-diluted protein purified with PureSpeed™ IMAC tips on a Lacey grid (*see* **Note 5**).
4. Adjust the tweezers on the Leica plunge freezer, transfer it into the chamber, blot for 3 s, and plunge freeze the grid.
5. Store the grid in a grid box in liquid nitrogen before usage or mount directly on a cryo-holder for screening and data collection at a TEM (Fig. 3c). In this case we used a FEI Talos TEM 200 kV TEM.

4 Notes

1. For the purification with the PureSpeed™ IMAC tips a 96 deep well plate can be used to distribute the protein sample and the different buffers in 1 ml aliquots using a multichannel pipet.
2. The second washing step is only necessary in the case of buffer or detergent exchange and can be excluded for other protein purifications. In the case of PglK the detergent DDM was exchanged for LMNG.
3. The elution volume can be further decreased to achieve a higher concentration in the sample.
4. The eluted sample should have less than 0.1% glycerol; otherwise it will produce artifacts after staining with uranyl acetate or

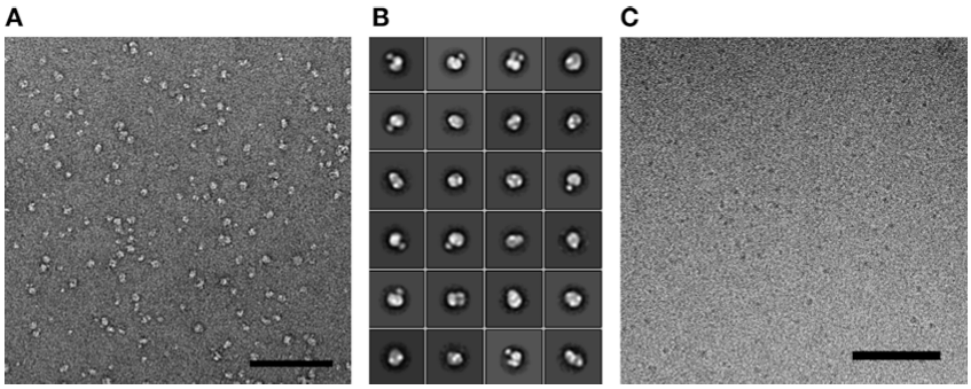

Fig. 3 EM analysis of purified protein. (**a**) Negative staining image of PglK purified with PureSpeed™ IMAC tips and diluted 1:35 times for staining with 2% uranyl acetate. Image was taken at a magnification of 105,000 and a pixel size of 5.6 Å. Black bar in the inset indicates 100 nm. (**b**) Selection of representative classes of a two-dimensional (2D) classification. Particles were picked automatically and 2D classified using Relion 3.0. No CTF correction was performed. (**c**) Cryo-EM micrograph of PglK in ice on a Lacey grid. The scale bar indicates a size of 100 nm. The image was recorded with a FEI Ceta 16 M Pixel CMOS camera at a magnification of 120,000× and a pixel size of 1.26 Å

freezing in liquid ethane. A high glycerol concentration will otherwise increase the signal-to-noise ratio in the recorded images. If the sample contains a high amount of glycerol, washing steps of up to ten times before staining with uranyl acetate can help.

5. It might be useful to prepare a small series of dilutions between 1:3 and 1:5 if the concentration is too high. If the protein concentration is on the other hand too low one can use an equilibrated concentrator for small volumes to concentrate the eluted sample to half or quarter of the volume.

Acknowledgments

We thank the staff at the BioEM Lab and Nano Imaging Lab of the University of Basel. This work was supported by the Swiss National Science Foundation (SNSF) (PP00P3_170607).

References

1. Wallin E, Von Heijne G (1998) Genome-wide analysis of integral membrane proteins from eubacterial, archaean, and eukaryotic organisms. Protein Sci 7:1029–1038
2. Arinaminpathy Y, Khurana E, Engelman DM, Gerstein MB (2009) Computational analysis of membrane proteins: the largest class of drug targets. Drug Discov Today 14:1130–1135
3. Oprea TI, Bologa CG, Brunak S et al (2018) Unexplored therapeutic opportunities in the human genome. Nat Rev Drug Discov 17:317

4. Faruqi AR, McMullan G (2018) Direct imaging detectors for electron microscopy. Nucl Instrum Methods Phys Res A 878:180–190
5. Song B, Lenhart J, Flegler VJ et al (2019) Capabilities of the Falcon III detector for single-particle structure determination. Ultramicroscopy 203:145–154
6. Li K, Sun C, Klose T et al (2019) Sub-3 Åapoferritin structure determined with full range of phase shifts using a single position of volta phase plate. J Struct Biol 206:225–232
7. Kimanius D, Forsberg BO, Scheres S, Lindahl E (2016) Accelerated cryo-EM structure determination with parallelisation using GPUs in RELION-2. Elife 5. https://doi.org/10.7554/eLife.18722
8. Zivanov J, Nakane T, Forsberg BO et al (2018) New tools for automated high-resolution cryo-EM structure determination in RELION-3. Elife 7:e42166
9. Punjani A, Rubinstein JL, Fleet DJ, Brubaker MA (2017) cryoSPARC: algorithms for rapid unsupervised cryo-EM structure determination. Nat Methods 14:290
10. Grant T, Rohou A, Grigorieff N (2018) cisTEM, user-friendly software for single-particle image processing. Elife 7:e35383
11. Schmidli C, Albiez S, Rima L et al (2019) Microfluidic protein isolation and sample preparation for high resolution cryo-EM. Proc Natl Acad Sci U S A 116 (30):15007–15012. bioRxiv 556068
12. Arnold SA, Albiez S, Opara N et al (2016) Total sample conditioning and preparation of nanoliter volumes for electron microscopy. ACS Nano 10:4981–4988
13. Stark H, Chari A (2016) Sample preparation of biological macromolecular assemblies for the determination of high-resolution structures by cryo-electron microscopy. Microscopy 65:23–34
14. Thompson RF, Walker M, Siebert CA et al (2016) An introduction to sample preparation and imaging by cryo-electron microscopy for structural biology. Methods 100:3–15
15. Perez C, Gerber S, Boilevin J et al (2015) Structure and mechanism of an active lipid-linked oligosaccharide flippase. Nature 524:433–438. https://doi.org/10.1038/nature14953
16. Rohou A, Grigorieff N (2015) CTFFIND4: fast and accurate defocus estimation from electron micrographs. J Struct Biol 192:216–221. https://doi.org/10.1016/j.jsb.2015.08.008
17. Abràmoff MD, Magalhães PJ, Ram SJ (2004) Image processing with ImageJ. Biophoton Int 11:36–42

4 Discussion and outlook

4.1 Characterization of the essential choline importer LicB

As *S. pneumoniae* remains to be a global threat and bacterial infections by MDR strains are nowhere near in decreasing numbers[28,29], a better understanding of the process connected to bacterial invasion and pathogenesis is crucial in order to find novel drug targets and develop drugs. This Gram-positive human pathogen *S. pneumoniae* has a unique set of phosphorylcholine modified teichoic acids which equips the bacterium with a very specific way to invade and colonize host cells[72,108]. Targeting LicB, the essential importer for the substrate choline, which is crucial for the supply of the teichoic acid modification, for its inhibition by antimicrobial compounds may help to tackle this pathogen that can carry MDR genes and can be challenging to eliminate with conventional antibiotics. Additionally, other pathogens that reside in the mucosal surface, like the Gram-negative *H. influenzae* use a similar pathway of host invasion and pathogenesis by phosphorylcholine modified LPS[106], where choline is also imported by LicB or a homologous protein[79]. The presence of the *lic* operon in those and other pathogens shows the essential role of phosphorylcholine modification across different bacterial phyla, including Gram-positive and Gram-negative bacteria.

The analysis of the obtained structures of the LicB transporter in its outward facing state and in its substrate bound, occluded state, together with the functional characterization provide a detailed understanding of the transport mechanisms. The choline bound structure allows the localization of the binding pocket together with the residues involved in coordinating the substrate. Residues W17, Y109, W167, Y233 and Y255 form an aromatic box around the trimethylammonium group of choline and stabilize the positive charge of the substrate by pi-electrons (**Figure 18A**). The hydroxyl end of choline is coordinated by Y236 and N252 in the binding pocket. Comparison of the central cavity of LicB to the homology model of LicB from *H. influenzae* shows the presence of aromatic and charged residues at the same

positions, therefore it is likely that choline binds there accordingly. The outward facing state of the transporter represents the conformation where the binding cavity, which is mostly negatively charged, is accessible to the substrate from the exterior.

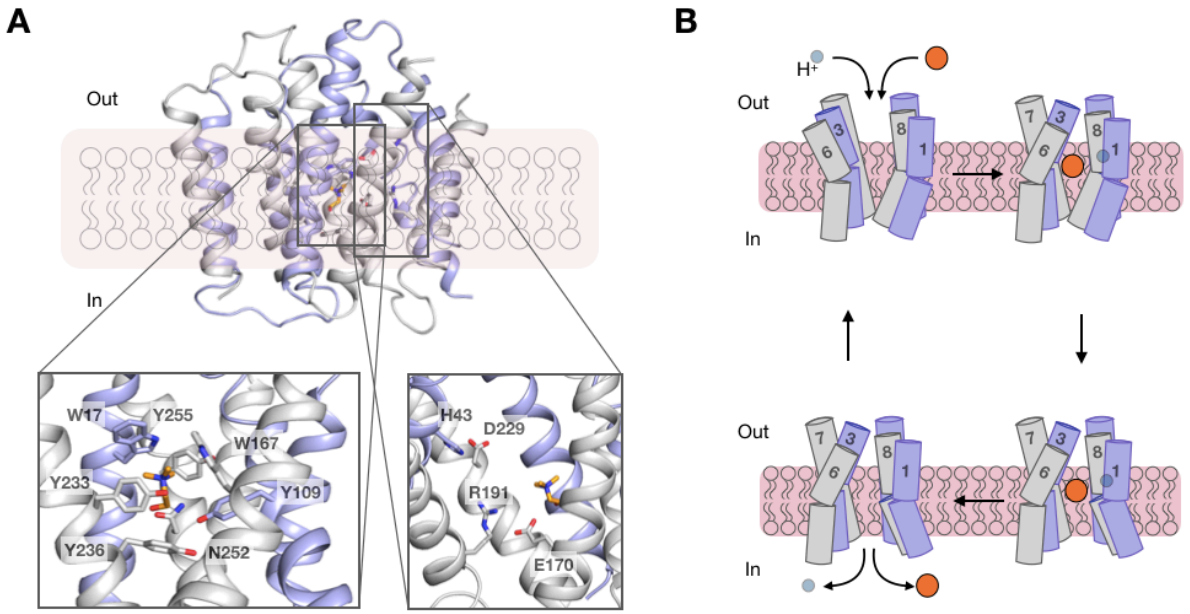

Figure 18: Binding pocket, proton-coupling residues and transport cycle of LicB. ***A.*** *Substrate bound and occluded structure of LicB. Inverted repeats TM1-TM5 and TM6-TM10 are colored in grey and blue, respectively. Choline is depicted in orange. The left bottom inset shows residues involved in coordinating choline binding. The right bottom shows residues involved in proton-coupling* ***B.*** *Schematics of transport cycle as predicted based on the outward facing and occluded structures. Choline is depicted as an orange sphere and a proton as a blue sphere.*

As shown by fluorescence based transport assays with a proton sensitive fluorophore, the energy for the transport is provided from a proton gradient. Due to a mostly acidic environment in the nasopharynx, the place where the pathogen is residing, the proton gradient must be inward directed and protons access the transporter at the same time as choline. Substrate and proton binding induce conformational changes with the most prominent movement of TM3 and TM6 before entering the occluded state. Due to the typical topology of two inverted repeats in all members of the DMT superfamily[173], it is possible to speculate that there will be a

symmetrical movement of the corresponding helices TM1 and TM8 when the transporter is facing the cytoplasm for substrate and proton release (Figure 18B).

Transport assays of proton flux on LicB mutated variants show that residues R191, H43 and E170 are important for proton coupling, of which R191 and E170 are highly conserved residues, and mutating those to alanine diminishes activity. PfCRT, a chloroquine resistant transporter from *P. falciparum* which also belongs to the DMT superfamily[258], exhibits the highest similarity to LicB. As for LicB, the binding cavity of this transporter, has an electronegative surface. Furthermore, PfCRT was shown to use proton-motive force for the efflux of chloroquine and has similar charged residues, as in LicB, that are possibly involved in protonation and deprotonation to facilitate transport[311]. A superposition of the outward open structures of LicB and PfCRT with an r.m.s.d. of 2.6 Å shows charged residues located at the same position in the central cavity of $H43_{LicB}/H97_{PfCRT}$, $E170_{LicB}/D137_{PfCRT}$, $R191_{LicB}/R231_{PfCRT}$ and $D229_{LicB}/D326_{PfCRT}$ (Figure 19A).

Many methods for the characterization of the transport by membrane proteins are prone to artifacts in the signals arising from the presence of detergent micelles or lipids in the buffer. SSM-electrophysiology has proven to be the most reliable and reproducible method to study electrogenic transport of choline and derivatives via LicB reconstituted into liposomes. The SSM-electrophysiology experiments show that choline, with a determined EC_{50} of 47 ± 15 µM, is not the only recognized and imported substrate for LicB. Additionally, arsenocholine (EC_{50} =170 ± 9 µM) and acetylcholine (EC_{50} =740 ± 84 µM) are recognized by the transporter. The extraction of WTA and LTA from *S. pneumoniae* grown in choline-reduced media supplemented with radiolabeled [^{3}H]-acetylcholine at the acetyl group or the amino group additionally provides evidence that choline derivatives can not only be imported, but also modified in order to provide phosphorylcholine, or phosphorylcholine-like moieties. Those teichoic acids that were extracted from *S. pneumoniae* grown in media supplemented with acetylcholine radiolabeled at the amino group exhibited radioactivity opposed to acetylcholine radiolabeled at the acetyl group. Acetylcholine

must be therefore modified or broken down into smaller parts, where the part of the acetyl group is not present after its modification and attachment to the teichoic acids.

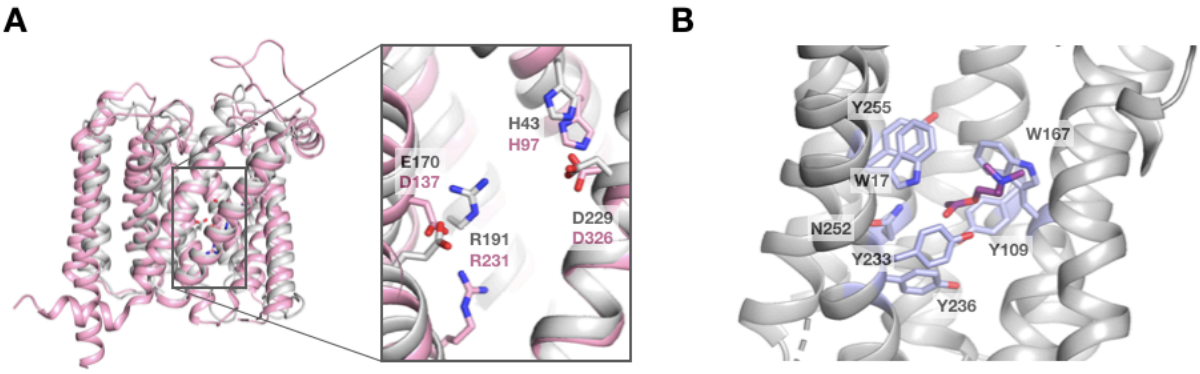

***Figure 19**: Proton-coupling residues in LicB and PfCRT and acetylcholine in the binding pocket **A.** Superposition and structural similarity of LicB (grey) and PfCRT (pink). The inset shows putative proton coupling residues from LicB depicted in grey and similar residues in close proximity in PfCRT depicted in pink. **B.** Acetylcholine docked with Autodock Vina into the outward open structure of LicB. Residues involved in the coordination of choline are depicted as sticks and can accommodate acetylcholine.*

This finding of a promiscuous substrate recognition, import and catabolization for the synthesis of chemically activated phosphorylcholine shows a potential for adaptation to the environmental availability of choline. This gives *S. pneumoniae* a more extensive survival capability where derivatives of choline like arsenocholine or acetylcholine can be imported and used for the modification of teichoic acids to replace or mimic phosphorylcholine. This ensures the ability of the bacteria to maintain its functions though the interactions with choline binding host receptors or CBPs for invasion and pathogenesis. Although the half maximal effective concentration for acetylcholine is lower than for choline, the naturally available high concentration of acetylcholine close to the neuronal cleft[312] might be sufficient to provide the bacteria with this alternative substrate, during the invasion of the brain. On the other hand, it might be possible that proteins are present that hydrolyze acetylcholine before it is either imported or after it enters the cytoplasm. SSM-electrophysiology and docking of acetylcholine clearly show that this alternative

substrate can be accommodated in the binding cavity of LicB by the same residues that are involved in choline binding (**Figure 19B**).

4.2 SSM electrophysiology for the selection of inhibitory nanobodies

The bottleneck for the cascade of invasion, adherence and virulence in *S. pneumoniae* and several other human pathogens harbored in the nasopharynx is connected to phosphorylcholine moieties of the teichoic acids or LPS[79,110,113,313-316]. Those are only synthesized if the bacteria are able to acquire exogenous choline or can import and modify compounds that can substitute or mimic choline, as described above for *S. pneumoniae* and acetylcholine. There is only one transporter known in *S. pneumoniae* that imports choline[72]. Gene deletion for the LicB transporter has shown to result in non-viability of the bacteria[317] and hence blocking or inhibiting the choline importer LicB should show similar effects of non-viability. This presents LicB as an optimal drug target against infections caused by *S. pneumoniae*. However, inhibitors of LicB must be unique binders that don not interact with other proteins, like abundant choline importers in human cells.

Nanobodies are the single variable domains of the heavy chain only antibodies that can be found in camelids[318,319]. They are important tools for structural biology of membrane proteins and are utilized for stabilizing conformations, for structure determinations as scaffolds or as inhibitors[245,246]. Nanobodies cannot only be generated by the immunization of camelids, but through *in vitro* based methods via phage or yeast display[246,320-322]. They carry great potential as inhibitors for therapeutic use because they are easier to produce, more stable, smaller than antibodies and are less toxic than chemical compounds[323-325]. Not all generated nanobodies inhibit the activity of the target protein and a screening method is required if those need to be identified. Most biophysical and biochemical screening methods like isothermal titration calorimetry[326], surface plasmon resonance[327] or microscale thermophoresis[328] rely on labelling compounds or interact with the detergent micelle which is prone to produce signal artefacts. SSM-electrophysiology on the other hand allows a

reproducible high-throughput screening of electrogenic transport[214,218]. The presented method of nanobody selection via SSM-electrophysiology enables to screen for inhibitory nanobodies and can be applied for all kinds of electrogenic transporters. Since the binding is reversible it is additionally possible to use a chip coated with proteoliposomes to screen several nanobodies for a high throughput. To unbind the nanobody, washing steps are crucial and it is important to normalize the peak current between measurements for data analysis. With the presented method the bottleneck is therefore not the screening but rather the expression and purification of the target protein and the nanobodies. The advantages using SSM-electrophysiology are a high throughput, good reproducibility, low sample consumption and a very low SNR.

In the case of LicB, hemicholinium-3 (HC-3) shows inhibitory effects, but it will not be possible to use this chemical compound as a drug against *S. pneumoniae*. HC-3 is not selectively blocking the pathogenic transporter LicB but is known to inhibit other choline importers that are abundant in human cells and is therefore toxic[329-331]. The sybodies on the other hand were selected specifically against LicB with unique epitopes interacting with the transporter. The selected inhibitory sybodies therefore carry a lesser potential for the interaction with human cells and could enable future studies for the treatment of pneumococcal infections. As they are unable to penetrate the native barrier of the pneumococcal capsule, the surface layer with PG, WTAs and LTAs, a suitable delivery vector needs to be found for a successful treatment. Conventional antibiotics are alternations of chemical compounds that act through the same mechanism of inhibition, by blocking ribosomal subunits to inhibit bacterial protein synthesis, inhibit cell wall synthesis or PG synthesis[332]. Due to the antibiotics crisis with fewer novel antimicrobial compounds being developed[333], novel drugs are in need. The application of nanobodies as antimicrobials immensely increases possible drug targets and offers a more dynamic and versatile toolset for drug development to battle MDR bacteria, in cancer therapy[323] and many more[325].

4.3 Dimerization of LicB and other DMT superfamily members

Dimerization of membrane transporters has been observed for many cases and over two thirds of membrane proteins of known structures are present in an oligomeric state[334,335]. To date, oligomerization or dimerization of membrane proteins cannot easily be predicted and the study of dimer formation, stabilization and energy costs in lipidic environments are the focus of current transporter studies[336,337]. The outward facing structure of LicB in nanodiscs is a dimer where the interface is formed by TM1, TM8 and TM9 which are stabilized by a lipid. Similarly, other DMT members have been observed to form dimers such as CST, TPT and Vrg4 transporters[186,189,338]. However, the dimer interface of those transporters (**Figure 10**) is different from the one in nanodisc reconstituted LicB and rather resembles the interface that is formed on the LicB crystal. Dimers or oligomers that can be observed in crystals are possibly artificial oligomers, since their formation is forced through supersaturation and addition of precipitating agents. Their physiological relevance therefore needs to be confirmed by biophysical methods.

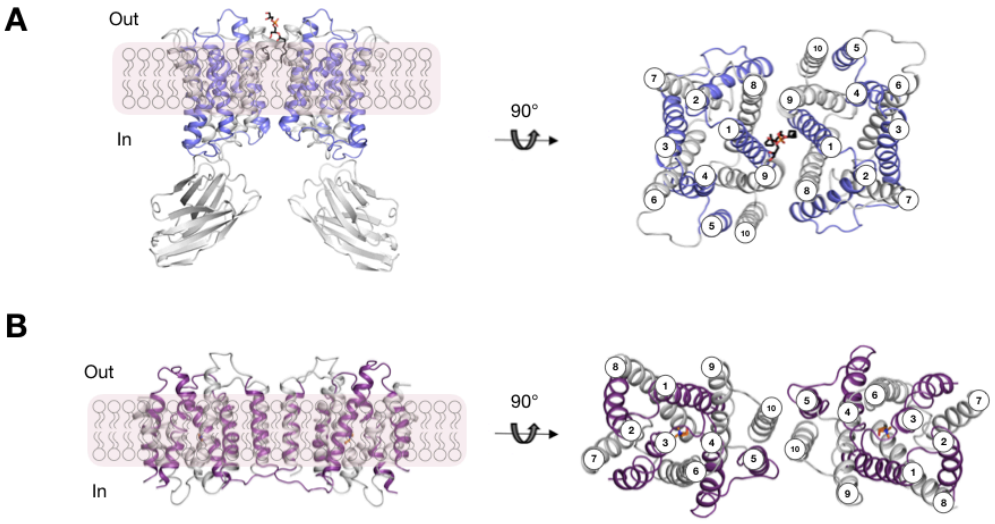

***Figure 20**: Dimer interfaces in LicB. **A.** Dimer of nanodisc reconstituted LicB bound to a sybody. Inverted repeats of TM1-TM5 and TM6-TM10 are colored in grey and blue, respectively. Side view and top view are shown. A lipid is present at the interface between TM1, TM8 and TM9 and depicted in black. **B.** Putative dimer interface of LicB from crystallized protein. The interface is formed by TM5 and TM10. Inverted repeats of TM1-TM5 and TM6-TM10 are colored in grey and violet, respectively and choline is shown in orange.*

Comparison of the interfaces of the DMT transporter dimers to the interface formed in the LicB crystal (Figure 20) reveals their resemblance with the interface formed by TM5 and TM10. Mutation studies in Vrg4 show that dimer formation has no effect on the affinity of the substrate but allows a faster cycling of the transport. Lipids must play a central role for the formation of LicB dimers because the prominent species in detergent is its monomeric form. Future studies on the dimerization of LicB and DMT transporters will provide a better understanding of the physiological relevance of the dimer in the membrane, if it is energetically preferred due to membrane curvatures or important for affinity, the transport cycle or stability.

4.4 Small scale purification for single particle cryo-EM

Single particle cryo-EM has recently become one of the most popular methods of choice for structural studies of membrane proteins[223,253]. Membrane proteins are highly abundant and make up nearly a third of the genome across all living organisms[339]. They play an integral role as drug targets in pharmaceutical applications[223,340,341]. More than 50% of the drugs that are currently available on the market are targeting membrane proteins, however the number of membrane proteins with known structure is very far behind those for soluble proteins[342]. One of the bottlenecks for the study of membrane proteins is the challenge to purify large amounts of pure membrane protein sample due to lower thermal stability[223]. The strengths of single particle cryo-EM is that it requires a very small amount of protein in a native buffer composition that can be directly applied on the EM grid[251-253]. The described method for the fast small-scale membrane protein purification and grid preparation offers a fast and parallelized way to prepare protein samples in different buffer compositions. For a successful application, it is recommended to optimize the purification of the protein beforehand and use the parallelized method to screen additional buffer compositions, additives, substrates and inhibitors, in order to trap different conformational states. This method offers a minimal sample consumption for the purification of the protein in different compositions and offers direct application

for grid preparation and screening within one day. This method can be applied to any poly-histidine tagged soluble or membrane protein.

5 References

1 Fleming, A. On the antibacterial action of cultures of a penicillium, with special reference to their use in the isolation of B. influenzae. 1929. Bull World Health Organ 79, 780-790 (1929).

2 Abraham, E. P. et al. Further observations on penicillin. The Lancet 238, 177-189 (1941).

3 Katz, L. & Baltz, R. H. Natural product discovery: past, present, and future. Journal of Industrial Microbiology and Biotechnology 43, 155-176 (2016).

4 Waksman, S. A., Schatz, A. & Reynolds, D. M. Production of antibiotic substances by actinomycetes. Annals of the New York Academy of Sciences 48, 73-86 (1946).

5 Newman, D. J. & Cragg, G. M. Natural products as sources of new drugs from 1981 to 2014. Journal of natural products 79, 629-661 (2016).

6 Andersson, D. I., Jerlström-Hultqvist, J. & Näsvall, J. Evolution of new functions de novo and from preexisting genes. Cold Spring Harbor perspectives in biology 7, a017996 (2015).

7 Morar, M. & Wright, G. D. The genomic enzymology of antibiotic resistance. Annual review of genetics 44, 25-51 (2010).

8 Björkman, J., Nagaev, I., Berg, O., Hughes, D. & Andersson, D. I. Effects of environment on compensatory mutations to ameliorate costs of antibiotic resistance. Science 287, 1479-1482 (2000).

9 Salverda, M. L., Koomen, J., Koopmanschap, B., Zwart, M. P. & de Visser, J. A. G. Adaptive benefits from small mutation supplies in an antibiotic resistance enzyme. Proceedings of the National Academy of Sciences 114, 12773-12778 (2017).

10 Le Roux, F. & Blokesch, M. Eco-evolutionary dynamics linked to horizontal gene transfer in Vibrios. Annual review of microbiology 72, 89-110 (2018).

11 Letten, A. D., Hall, A. R. & Levine, J. M. Using ecological coexistence theory to understand antibiotic resistance and microbial competition. Nature Ecology & Evolution 5, 431-441 (2021).

12 Larsson, D. & Flach, C.-F. Antibiotic resistance in the environment. Nature Reviews Microbiology, 1-13 (2021).

13 Sengupta, S., Chattopadhyay, M. K. & Grossart, H. P. The multifaceted roles of antibiotics and antibiotic resistance in nature. Front Microbiol 4, 47, doi:10.3389/fmicb.2013.00047 (2013).

14 Piddock, L. J. The crisis of no new antibiotics--what is the way forward? Lancet Infect Dis 12, 249-253, doi:10.1016/S1473-3099(11)70316-4 (2012).

15 Spellberg, B. & Gilbert, D. N. The future of antibiotics and resistance: a tribute to a career of leadership by John Bartlett. Clin Infect Dis 59 Suppl 2, S71-75, doi:10.1093/cid/ciu392 (2014).
16 Goossens, H., Ferech, M., Vander Stichele, R., Elseviers, M. & Group, E. P. Outpatient antibiotic use in Europe and association with resistance: a cross-national database study. The Lancet 365, 579-587 (2005).
17 Riedel, S. et al. Antimicrobial use in Europe and antimicrobial resistance in Streptococcus pneumoniae. European journal of clinical microbiology & infectious diseases 26, 485-490 (2007).
18 Hollis, A. & Ahmed, Z. Preserving antibiotics, rationally. New England Journal of Medicine 369, 2474-2476 (2013).
19 Weinstein, R. A. Controlling antimicrobial resistance in hospitals: infection control and use of antibiotics. Emerging infectious diseases 7, 188 (2001).
20 Collignon, P., Beggs, J. J., Walsh, T. R., Gandra, S. & Laxminarayan, R. Anthropological and socioeconomic factors contributing to global antimicrobial resistance: a univariate and multivariable analysis. The Lancet Planetary Health 2, e398-e405 (2018).
21 Payne, D. J., Gwynn, M. N., Holmes, D. J. & Pompliano, D. L. Drugs for bad bugs: confronting the challenges of antibacterial discovery. Nature reviews Drug discovery 6, 29-40 (2007).
22 Xu, Q., Pichichero, M. E., Casey, J. R. & Zeng, M. Novel type of Streptococcus pneumoniae causing multidrug-resistant acute otitis media in children. Emerging infectious diseases 15, 547 (2009).
23 Pelton, S. I. et al. Emergence of 19A as virulent and multidrug resistant Pneumococcus in Massachusetts following universal immunization of infants with pneumococcal conjugate vaccine. The Pediatric infectious disease journal 26, 468-472 (2007).
24 Orihuela, C. J. et al. Laminin receptor initiates bacterial contact with the blood brain barrier in experimental meningitis models. J Clin Invest 119, 1638-1646, doi:10.1172/JCI36759 (2009).
25 Yahiaoui, R. Y. et al. Prevalence and antibiotic resistance of commensal Streptococcus pneumoniae in nine European countries. Future Microbiol 11, 737-744, doi:10.2217/fmb-2015-0011 (2016).
26 Cillóniz, C., Garcia-Vidal, C., Ceccato, A. & Torres, A. in Antimicrobial Resistance in the 21st Century 13-38 (Springer, 2018).
27 Bogaert, D., De Groot, R. & Hermans, P. W. Streptococcus pneumoniae colonisation: the key to pneumococcal disease. Lancet Infect Dis 4, 144-154, doi:10.1016/S1473-3099(04)00938-7 (2004).

28 Weisfelt, M., van de Beek, D., Spanjaard, L., Reitsma, J. B. & de Gans, J. Clinical features, complications, and outcome in adults with pneumococcal meningitis: a prospective case series. Lancet Neurol 5, 123-129, doi:10.1016/S1474-4422(05)70288-X (2006).
29 van de Beek, D., de Gans, J., Tunkel, A. R. & Wijdicks, E. F. Community-acquired bacterial meningitis in adults. N Engl J Med 354, 44-53, doi:10.1056/NEJMra052116 (2006).
30 Organization, W. H. Antimicrobial resistance: global report on surveillance. (World Health Organization, 2014).
31 Mm, H. D. B. A resistant pneumococcus. Lancet 2, 264-265 (1967).
32 Appelbaum, P. et al. Streptococcus pneumoniae resistant to penicillin and chloramphenicol. The Lancet 310, 995-997 (1977).
33 Jacobs, M. R. et al. Emergence of multiply resistant pneumococci. New England Journal of Medicine 299, 735-740 (1978).
34 Waxman, D. J. & Strominger, J. L. Penicillin-binding proteins and the mechanism of action of beta-lactam antibiotics. Annual review of biochemistry 52, 825-869 (1983).
35 Menninger, J. R. Mechanism of inhibition of protein synthesis by macrolide and lincosamide antibiotics. Journal of basic and clinical physiology and pharmacology 6, 229-250 (1995).
36 Bambeke, F., Reinert, R. R., Appelbaum, P. C., Tulkens, P. M. & Peetermans, W. E. Multidrug-resistant Streptococcus pneumoniae infections. Drugs 16, 2355-2382 (2007).
37 Draghi, D., Jones, M., Sahm, D. & Tillotson, G. Geographically-based evaluation of multidrug resistance trends among Streptococcus pneumoniae in the USA: findings of the FAST surveillance initiative (2003–2004). International journal of antimicrobial agents 28, 525-531 (2006).
38 Whitney, C. G. et al. Increasing prevalence of multidrug-resistant Streptococcus pneumoniae in the United States. New England Journal of Medicine 343, 1917-1924 (2000).
39 Kam, K. M. et al. Emergence of multiple-antibiotic-resistant Streptococcus pneumoniae in Hong Kong. Antimicrobial agents and chemotherapy 39, 2667-2670 (1995).
40 Lynch, J. P. & Zhanel, G. G. in Seminars in Respiratory and Critical Care Medicine. 210-238 (© Thieme Medical Publishers).
41 Fedson, D. S. et al. Pneumococcal vaccine after 15 years of use: another view. Archives of internal medicine 154, 2531-2535 (1994).
42 Eskola, J. & Anttila, M. Pneumococcal conjugate vaccines. The Pediatric infectious disease journal 18, 543-551 (1999).

43 Schuchat, A. et al. Progress in vaccine-preventable and respiratory infectious diseases—first 10 years of the CDC National Center for Immunization and Respiratory Diseases, 2006–2015. Emerging infectious diseases 24, 1178 (2018).
44 Brotherton, A. L. & Shah, R. Recent updates to the advisory committee on immunization practices recommendations for pneumococcal and herpes zoster vaccination. RI Med J 103, 34-37 (2020).
45 Cilloniz, C., Menendez, R., Garcia-Vidal, C., Pericas, J. M. & Torres, A. Defining Community-Acquired Pneumonia as a Public Health Threat: Arguments in Favor from Spanish Investigators. Med Sci (Basel) 8, doi:10.3390/medsci8010006 (2020).
46 Gram, C. Ueber die isolirte Farbung der Schizomyceten in Schnitt-und Trockenpraparaten. Fortschritte der Medicin 2, 185-189 (1884).
47 Silhavy, T. J., Kahne, D. & Walker, S. The bacterial cell envelope. Cold Spring Harb Perspect Biol 2, a000414, doi:10.1101/cshperspect.a000414 (2010).
48 Mitchell, P. Approaches to the analysis of specific membrane transport. Biological structure and function 2, 581-599 (1961).
49 Raetz, C. R. & Whitfield, C. Lipopolysaccharide endotoxins. Annu Rev Biochem 71, 635-700, doi:10.1146/annurev.biochem.71.110601.135414 (2002).
50 Nikaido, H. Molecular basis of bacterial outer membrane permeability revisited. Microbiology and molecular biology reviews 67, 593-656 (2003).
51 Kamio, Y. & Nikaido, H. Outer membrane of Salmonella typhimurium: accessibility of phospholipid head groups to phospholipase c and cyanogen bromide activated dextran in the external medium. Biochemistry 15, 2561-2570, doi:10.1021/bi00657a012 (1976).
52 Neuhaus, F. C. & Baddiley, J. A continuum of anionic charge: structures and functions of D-alanyl-teichoic acids in gram-positive bacteria. Microbiol Mol Biol Rev 67, 686-723, doi:10.1128/mmbr.67.4.686-723.2003 (2003).
53 Wang, L., Wang, Q. & Reeves, P. R. in Endotoxins: Structure, Function and Recognition 123-152 (Springer, 2010).
54 Reeves, P. & Wang, L. Genomic organization of LPS-specific loci. Pathogenicity islands and the evolution of pathogenic microbes, 109-135 (2002).
55 Achtman, M. & Pluschke, G. Clonal analysis of descent and virulence among selected Escherichia coli. Annual Reviews in Microbiology 40, 185-210 (1986).
56 Pluschke, G., Mayden, J., Achtman, M. & Levine, R. Role of the capsule and the O antigen in resistance of O18: K1 Escherichia coli to complement-mediated killing. Infection and immunity 42, 907-913 (1983).

57 Fischer, W. in New comprehensive biochemistry Vol. 27 199-215 (Elsevier, 1994).
58 Lambert, P. A., Hancock, I. C. & Baddiley, J. Occurrence and function of membrane teichoic acids. Biochimica et biophysica acta 472, 1-12 (1977).
59 Wicken, A. & Knox, K. W. Lipoteichoic acids: a new class of bacterial antigen. Science 187, 1161-1167 (1975).
60 Armstrong, J., Baddiley, J., Buchanan, J., Carss, B. & Greenberg, G. 882. Isolation and structure of ribitol phosphate derivatives (teichoic acids) from bacterial cell walls. Journal of the Chemical Society (Resumed), 4344-4354 (1958).
61 Baddiley, J. in Federation proceedings. 1084-1088.
62 Weidenmaier, C. & Peschel, A. Teichoic acids and related cell-wall glycopolymers in Gram-positive physiology and host interactions. Nat Rev Microbiol 6, 276-287, doi:10.1038/nrmicro1861 (2008).
63 Weidel, W. & Pelzer, H. BAGSHAPED MACROMOLECULES--A NEW OUTLOOK ON BACTERIAL CELL WALLS. Adv Enzymol Relat Areas Mol Biol 26, 193-232 (1964).
64 Peschel, A. et al. Inactivation of the dlt Operon inStaphylococcus aureus confers sensitivity to defensins, protegrins, and other antimicrobial peptides. Journal of Biological Chemistry 274, 8405-8410 (1999).
65 van der Es, D., Hogendorf, W. F., Overkleeft, H. S., van der Marel, G. A. & Codée, J. D. Teichoic acids: synthesis and applications. Chemical Society Reviews 46, 1464-1482 (2017).
66 Naumova, I. B. et al. Cell wall teichoic acids: structural diversity, species specificity in the genus Nocardiopsis, and chemotaxonomic perspective. FEMS microbiology reviews 25, 269-283 (2001).
67 Schneewind, O. & Missiakas, D. Lipoteichoic acids, phosphate-containing polymers in the envelope of gram-positive bacteria. Journal of bacteriology 196, 1133-1142 (2014).
68 Reichmann, N. T. & Gründling, A. Location, synthesis and function of glycolipids and polyglycerolphosphate lipoteichoic acid in Gram-positive bacteria of the phylum Firmicutes. FEMS microbiology letters 319, 97-105 (2011).
69 Ganfield, M. & Pieringer, R. A. The biosynthesis of nascent membrane lipoteichoic acid of Streptococcus faecium (S. faecalis ATCC 9790) from phosphatidylkojibiosyl diacylglycerol and phosphatidylglycerol. Journal of Biological Chemistry 255, 5164-5169 (1980).

70 Swoboda, J. G., Campbell, J., Meredith, T. C. & Walker, S. Wall teichoic acid function, biosynthesis, and inhibition. Chembiochem 11, 35-45, doi:10.1002/cbic.200900557 (2010).
71 Winstel, V., Xia, G. & Peschel, A. Pathways and roles of wall teichoic acid glycosylation in Staphylococcus aureus. International Journal of Medical Microbiology 304, 215-221 (2014).
72 Denapaite, D., Brückner, R., Hakenbeck, R. & Vollmer, W. Biosynthesis of teichoic acids in Streptococcus pneumoniae and closely related species: lessons from genomes. Microbial drug resistance 18, 344-358 (2012).
73 FISCHER, W. Pneumococcal lipoteichoic and teichoic acid. Microbial Drug Resistance 3, 309-325 (1997).
74 Seo, H. S., Cartee, R. T., Pritchard, D. G. & Nahm, M. H. A new model of pneumococcal lipoteichoic acid structure resolves biochemical, biosynthetic, and serologic inconsistencies of the current model. Journal of bacteriology 190, 2379-2387 (2008).
75 Aanensen, D. M., Mavroidi, A., Bentley, S. D., Reeves, P. R. & Spratt, B. G. Predicted functions and linkage specificities of the products of the Streptococcus pneumoniae capsular biosynthetic loci. Journal of bacteriology 189, 7856-7876 (2007).
76 Song, J.-H. et al. Identification of essential genes in Streptococcus pneumoniae by allelic replacement mutagenesis. Molecules & Cells (Springer Science & Business Media BV) 19 (2005).
77 Baur, S., Marles-Wright, J., Buckenmaier, S., Lewis, R. J. & Vollmer, W. Synthesis of CDP-activated ribitol for teichoic acid precursors in Streptococcus pneumoniae. Journal of bacteriology 191, 1200-1210 (2009).
78 Tomasz, A. Choline in the cell wall of a bacterium: novel type of polymer-linked choline in Pneumococcus. Science 157, 694-697, doi:10.1126/science.157.3789.694 (1967).
79 Fan, X., Pericone, C. D., Lysenko, E., Goldfine, H. & Weiser, J. N. Multiple mechanisms for choline transport and utilization in Haemophilus influenzae. Mol Microbiol 50, 537-548, doi:10.1046/j.1365-2958.2003.03703.x (2003).
80 Eberhardt, A., Wu, L. J., Errington, J., Vollmer, W. & Veening, J. W. Cellular localization of choline-utilization proteins in Streptococcus pneumoniae using novel fluorescent reporter systems. Mol Microbiol 74, 395-408, doi:10.1111/j.1365-2958.2009.06872.x (2009).
81 Whiting, G. C. & Gillespie, S. H. Incorporation of choline into Streptococcus pneumoniae cell wall antigens: evidence for choline kinase activity. FEMS microbiology letters 138, 141-145 (1996).

82 Kwak, B. Y. et al. Structure and mechanism of CTP:phosphocholine cytidylyltransferase (LicC) from Streptococcus pneumoniae. J Biol Chem 277, 4343-4350, doi:10.1074/jbc.M109163200 (2002).
83 Whiting, G. C. & Gillespie, S. H. Investigation of a choline phosphate synthesis pathway in Streptococcus pneumoniae: evidence for choline phosphate cytidylyltransferase activity. FEMS Microbiol Lett 143, 279-284, doi:10.1111/j.1574-6968.1996.tb08493.x (1996).
84 Zhang, J. R., Idanpaan-Heikkila, I., Fischer, W. & Tuomanen, E. I. Pneumococcal licD2 gene is involved in phosphorylcholine metabolism. Mol Microbiol 31, 1477-1488, doi:10.1046/j.1365-2958.1999.01291.x (1999).
85 Waldow, F. et al. Attachment of phosphorylcholine residues to pneumococcal teichoic acids and modification of substitution patterns by the phosphorylcholine esterase. Journal of Biological Chemistry 293, 10620-10629 (2018).
86 Kovács, M. et al. A functional dlt operon, encoding proteins required for incorporation of d-alanine in teichoic acids in gram-positive bacteria, confers resistance to cationic antimicrobial peptides in Streptococcus pneumoniae. Journal of bacteriology 188, 5797-5805 (2006).
87 McCann, J. C., Hudes, M. & Ames, B. N. An overview of evidence for a causal relationship between dietary availability of choline during development and cognitive function in offspring. Neuroscience & Biobehavioral Reviews 30, 696-712 (2006).
88 Derbyshire, E. & Obeid, R. Choline, neurological development and brain function: A systematic review focusing on the first 1000 days. Nutrients 12, 1731 (2020).
89 Zeisel, S. H. Choline: needed for normal development of memory. Journal of the American College of Nutrition 19, 528S-531S (2000).
90 Akison, L. K., Kuo, J., Reid, N., Boyd, R. N. & Moritz, K. M. Effect of choline supplementation on neurological, cognitive, and behavioral outcomes in offspring arising from alcohol exposure during development: a quantitative systematic review of clinical and preclinical studies. Alcoholism: Clinical and Experimental Research 42, 1591-1611 (2018).
91 Leermakers, E. T. et al. Effects of choline on health across the life course: a systematic review. Nutrition reviews 73, 500-522 (2015).
92 Gámiz, F. & Gallo, M. A Systematic Review of the Dietary Choline Impact on Cognition from a Psychobiological Approach: Insights from Animal Studies. Nutrients 13, 1966 (2021).
93 Blusztajn, J. K., Slack, B. E. & Mellott, T. J. Neuroprotective actions of dietary choline. Nutrients 9, 815 (2017).

94 Lockman, P. & Allen, D. The transport of choline. Drug development and industrial pharmacy 28, 749-771 (2002).
95 Meyer, E., Engel, D. & Cooper, J. Acetylation and phosphorylation of choline following high or low affinity uptake by rat cortical synaptosomes. Neurochemical research 7, 749-759 (1982).
96 Barker, L. & Mittag, T. Comparative studies of substrates and inhibitors of choline transport and choline acetyltransferase. Journal of Pharmacology and Experimental Therapeutics 192, 86-94 (1975).
97 Yamamura, H. & Snyder, S. HIGH AFFINITY TRANSPORT OF CHOLINE INTO SYNAPTOSOMES OF RAT BRAIN 1. Journal of neurochemistry 21, 1355-1374 (1973).
98 Ojiakor, O. & Rylett, R. Modulation of sodium-coupled choline transporter CHT function in health and disease. Neurochemistry international, 104810 (2020).
99 Hedtke, V. & Bakovic, M. Choline transport for phospholipid synthesis: An emerging role of choline transporter-like protein 1. Experimental Biology and Medicine 244, 655-662 (2019).
100 Landfald, B. & Strøm, A. R. Choline-glycine betaine pathway confers a high level of osmotic tolerance in Escherichia coli. Journal of bacteriology 165, 849-855 (1986).
101 Lamark, T. et al. DNA sequence and analysis of the bet genes encoding the osmoregulatory choline—glycine betaine pathway of Escherichia coli. Molecular microbiology 5, 1049-1064 (1991).
102 Tøndervik, A. & Strøm, A. R. Membrane topology and mutational analysis of the osmotically activated BetT choline transporter of Escherichia coli. Microbiology 153, 803-813 (2007).
103 Weiser, J. N., Goldberg, J. B., Pan, N., Wilson, L. & Virji, M. The phosphorylcholine epitope undergoes phase variation on a 43-kilodalton protein in Pseudomonas aeruginosa and on pili of Neisseria meningitidis and Neisseria gonorrhoeae. Infection and immunity 66, 4263-4267 (1998).
104 Weiser, J. N. et al. Phosphorylcholine on the lipopolysaccharide of Haemophilus influenzae contributes to persistence in the respiratory tract and sensitivity to serum killing mediated by C-reactive protein. J Exp Med 187, 631-640, doi:10.1084/jem.187.4.631 (1998).
105 Garcia, P., Garcia, J. L., Garcia, E. & Lopez, R. Nucleotide sequence and expression of the pneumococcal autolysin gene from its own promoter in Escherichia coli. Gene 43, 265-272, doi:10.1016/0378-1119(86)90215-5 (1986).
106 Weiser, J. N., Shchepetov, M. & Chong, S. T. Decoration of lipopolysaccharide with phosphorylcholine: a phase-variable characteristic of Haemophilus

influenzae. Infect Immun 65, 943-950, doi:10.1128/IAI.65.3.943-950.1997 (1997).
107 Badger, E. The structural specificity of choline for the growth of type III pneumococcus. Journal of Biological Chemistry 153, 183-191 (1944).
108 Hakenbeck, R., Madhour, A., Denapaite, D. & Brückner, R. Versatility of choline metabolism and choline-binding proteins in Streptococcus pneumoniae and commensal streptococci. FEMS microbiology reviews 33, 572-586 (2009).
109 Gehre, F. et al. Essential role of choline for pneumococcal virulence in an experimental model of meningitis. Journal of internal medicine 264, 143-154 (2008).
110 Iuchi, H., Ohori, J., Kyutoku, T., Ito, K. & Kurono, Y. Role of phosphorylcholine in Streptococcus pneumoniae and nontypeable Haemophilus influenzae adherence to epithelial cells. Auris Nasus Larynx 46, 513-519, doi:10.1016/j.anl.2018.11.003 (2019).
111 Cundell, D. R., Gerard, N. P., Gerard, C., Idanpaan-Heikkila, I. & Tuomanen, E. I. Streptococcus pneumoniae anchor to activated human cells by the receptor for platelet-activating factor. Nature 377, 435-438, doi:10.1038/377435a0 (1995).
112 Swords, W. E. et al. Non-typeable Haemophilus influenzae adhere to and invade human bronchial epithelial cells via an interaction of lipooligosaccharide with the PAF receptor. Molecular microbiology 37, 13-27 (2000).
113 Gosink, K. K., Mann, E. R., Guglielmo, C., Tuomanen, E. I. & Masure, H. R. Role of novel choline binding proteins in virulence of Streptococcus pneumoniae. Infect Immun 68, 5690-5695, doi:10.1128/iai.68.10.5690-5695.2000 (2000).
114 GARCÍA, J. L., SÁNCHEZ-BEATO, A. R., MEDRANO, F. J. & LÓPEZ, R. Versatility of choline-binding domain. Microbial Drug Resistance 4, 25-36 (1998).
115 Giffard, P. M. & Jacques, N. A. Definition of a fundamental repeating unit in streptococcal glucosyltransferase glucan-binding regions and related sequences. J Dent Res 73, 1133-1141, doi:10.1177/00220345940730060201 (1994).
116 Garcia, P., Gonzalez, M. P., Garcia, E., Lopez, R. & Garcia, J. L. LytB, a novel pneumococcal murein hydrolase essential for cell separation. Mol Microbiol 31, 1275-1281, doi:10.1046/j.1365-2958.1999.01238.x (1999).
117 Garcia, P., Paz Gonzalez, M., Garcia, E., Garcia, J. L. & Lopez, R. The molecular characterization of the first autolytic lysozyme of Streptococcus pneumoniae reveals evolutionary mobile domains. Mol Microbiol 33, 128-138, doi:10.1046/j.1365-2958.1999.01455.x (1999).

118 Khan, M. N., Sharma, S. K., Filkins, L. M. & Pichichero, M. E. PcpA of Streptococcus pneumoniae mediates adherence to nasopharyngeal and lung epithelial cells and elicits functional antibodies in humans. Microbes and infection 14, 1102-1110 (2012).
119 McDANIEL, L. S., Sheffield, J. S., Delucchi, P. & Briles, D. PspA, a surface protein of Streptococcus pneumoniae, is capable of eliciting protection against pneumococci of more than one capsular type. Infection and immunity 59, 222-228 (1991).
120 Berry, A. M. & Paton, J. C. Additive attenuation of virulence of Streptococcus pneumoniae by mutation of the genes encoding pneumolysin and other putative pneumococcal virulence proteins. Infection and immunity 68, 133-140 (2000).
121 Rosenow, C. et al. Contribution of novel choline-binding proteins to adherence, colonization and immunogenicity of Streptococcus pneumoniae. Mol Microbiol 25, 819-829, doi:10.1111/j.1365-2958.1997.mmi494.x (1997).
122 Loughran, A. J., Orihuela, C. J. & Tuomanen, E. I. Streptococcus pneumoniae: invasion and inflammation. Microbiology spectrum 7, 7.2. 15 (2019).
123 Nelson, A. L. et al. Capsule enhances pneumococcal colonization by limiting mucus-mediated clearance. Infection and immunity 75, 83-90 (2007).
124 Zhang, J.-R. et al. The polymeric immunoglobulin receptor translocates pneumococci across human nasopharyngeal epithelial cells. Cell 102, 827-837 (2000).
125 Gradstedt, H., Iovino, F. & Bijlsma, J. J. Streptococcus pneumoniae invades endothelial host cells via multiple pathways and is killed in a lysosome dependent manner. PloS one 8, e65626 (2013).
126 Asmat, T. M., Agarwal, V., Saleh, M. & Hammerschmidt, S. Endocytosis of Streptococcus pneumoniae via the polymeric immunoglobulin receptor of epithelial cells relies on clathrin and caveolin dependent mechanisms. International Journal of Medical Microbiology 304, 1233-1246 (2014).
127 Attali, C. et al. Streptococcus pneumoniae choline-binding protein E interaction with plasminogen/plasmin stimulates migration across the extracellular matrix. Infection and immunity 76, 466-476 (2008).
128 Weiser, J. N., Austrian, R., Sreenivasan, P. K. & Masure, H. R. Phase variation in pneumococcal opacity: relationship between colonial morphology and nasopharyngeal colonization. Infection and immunity 62, 2582-2589 (1994).
129 Kim, J. O. et al. Relationship between cell surface carbohydrates and intrastrain variation on opsonophagocytosis of Streptococcus pneumoniae. Infection and immunity 67, 2327-2333 (1999).

130 Shaper, M., Hollingshead, S. K., Benjamin Jr, W. H. & Briles, D. E. PspA protects Streptococcus pneumoniae from killing by apolactoferrin, and antibody to PspA enhances killing of pneumococci by apolactoferrin. Infection and immunity 72, 5031-5040 (2004).
131 Feigenson, G. W. Phase behavior of lipid mixtures. Nature chemical biology 2, 560-563 (2006).
132 Feigenson, G. W. Phase boundaries and biological membranes. Annu. Rev. Biophys. Biomol. Struct. 36, 63-77 (2007).
133 Davies, R. E. & Ogston, A. G. On the mechanism of secretion of ions by gastric mucosa and by other tissues. Biochemical Journal 46, 324-333 (1950).
134 Ren, Q. & Paulsen, I. T. Large-scale comparative genomic analyses of cytoplasmic membrane transport systems in prokaryotes. Journal of molecular microbiology and biotechnology 12, 165-179 (2007).
135 Busch, W. & Saier, M. H. The transporter classification (TC) system, 2002. Critical reviews in biochemistry and molecular biology 37, 287-337 (2002).
136 Hille, B. Potassium channels and chloride channels. In Ionic Channels of Excitable Membrane. Edited by Hill B, 130-133 (1992).
137 Mitchell, P. A general theory of membrane transport from studies of bacteria. Nature 180, 134-136 (1957).
138 Patlak, C. S. Contributions to the theory of active transport: II. The gate type non-carrier mechanism and generalizations concerning tracer flow, efficiency, and measurement of energy expenditure. The bulletin of mathematical biophysics 19, 209-235 (1957).
139 Mitchell, P. Osmochemistry of solute translocation. Research in microbiology 141, 286-289 (1990).
140 Agre, P. The aquaporin water channels. Proceedings of the American Thoracic Society 3, 5-13 (2006).
141 Fairman, J. W., Noinaj, N. & Buchanan, S. K. The structural biology of β-barrel membrane proteins: a summary of recent reports. Current opinion in structural biology 21, 523-531 (2011).
142 Bernèche, S. & Roux, B. A gate in the selectivity filter of potassium channels. Structure 13, 591-600 (2005).
143 Kiss, L., LoTurco, J. & Korn, S. J. Contribution of the selectivity filter to inactivation in potassium channels. Biophysical journal 76, 253-263 (1999).
144 Gadsby, D. C. Ion pumps made crystal clear. Nature 450, 957-959 (2007).
145 Skou, J. The energy coupled exchange of Na+ for K+ across the cell membrane: The Na+, K+-pump. FEBS letters 268, 314-324 (1990).
146 Tanford, C. Mechanism of free energy coupling in active transport. Annual review of biochemistry 52, 379-409 (1983).

147 Albers, R. Biochemical aspects of active transport. Annual review of biochemistry 36, 727-756 (1967).
148 Rees, D. C., Johnson, E. & Lewinson, O. ABC transporters: the power to change. Nature reviews Molecular cell biology 10, 218-227 (2009).
149 Thomas, C. & Tampe, R. Multifaceted structures and mechanisms of ABC transport systems in health and disease. Current opinion in structural biology 51, 116-128 (2018).
150 Kane, P. M. The where, when, and how of organelle acidification by the yeast vacuolar H+-ATPase. Microbiology and Molecular Biology Reviews 70, 177-191 (2006).
151 Wagner, C. A. et al. Renal vacuolar H+-ATPase. Physiological reviews 84, 1263-1314 (2004).
152 Iwamoto, A., Omote, H., Nakamoto, R. K., Maeda, M. & Futai, M. in Molecular and Cellular Mechanisms of H+ Transport 221-228 (Springer, 1994).
153 Stangeland, B. et al. P-Type H+-and Ca2+-ATPases in Plant Cells a. Annals of the New York Academy of Sciences 834, 77-87 (1997).
154 Henderson, R. K., Fendler, K. & Poolman, B. Coupling efficiency of secondary active transporters. Curr. Opin. Biotechnol 58, 62-71 (2019).
155 Forrest, L. R., Krämer, R. & Ziegler, C. The structural basis of secondary active transport mechanisms. Biochimica et Biophysica Acta (BBA)-Bioenergetics 1807, 167-188 (2011).
156 Drew, D. & Boudker, O. Shared molecular mechanisms of membrane transporters. Annual review of biochemistry 85, 543-572 (2016).
157 Yan, N. Structural biology of the major facilitator superfamily transporters. Annual review of biophysics 44, 257-283 (2015).
158 Yan, N. A glimpse of membrane transport through structures—advances in the structural biology of the GLUT glucose transporters. Journal of molecular biology 429, 2710-2725 (2017).
159 Penmatsa, A. & Gouaux, E. How LeuT shapes our understanding of the mechanisms of sodium-coupled neurotransmitter transporters. The Journal of physiology 592, 863-869 (2014).
160 Perez, C. & Ziegler, C. Mechanistic aspects of sodium-binding sites in LeuT-like fold symporters. Biol Chem 394, 641-648, doi:10.1515/hsz-2012-0336 (2013).
161 Kazmier, K. et al. Conformational dynamics of ligand-dependent alternating access in LeuT. Nature structural & molecular biology 21, 472-479 (2014).
162 Fredriksson, R., Nordstrom, K. J., Stephansson, O., Hagglund, M. G. & Schioth, H. B. The solute carrier (SLC) complement of the human genome:

phylogenetic classification reveals four major families. FEBS Lett 582, 3811-3816, doi:10.1016/j.febslet.2008.10.016 (2008).

163 Hediger, M. A., Clémençon, B., Burrier, R. E. & Bruford, E. A. The ABCs of membrane transporters in health and disease (SLC series): introduction. Molecular aspects of medicine 34, 95-107 (2013).

164 He, L., Vasiliou, K. & Nebert, D. W. Analysis and update of the human solute carrier (SLC) gene superfamily. Human genomics 3, 1-12 (2009).

165 Hediger, M. A. et al. The ABCs of solute carriers: physiological, pathological and therapeutic implications of human membrane transport proteinsIntroduction. Pflugers Arch 447, 465-468, doi:10.1007/s00424-003-1192-y (2004).

166 Widdas, W. Inability of diffusion to account for placental glucose transfer in the sheep and consideration of the kinetics of a possible carrier transfer. The Journal of physiology 118, 23-39 (1952).

167 Vidaver, G. A. Inhibition of parallel flux and augmentation of counter flux shown by transport models not involving a mobile carrier. Journal of theoretical biology 10, 301-306 (1966).

168 Jardetzky, O. Simple allosteric model for membrane pumps. Nature 211, 969-970 (1966).

169 Deng, D. et al. Molecular basis of ligand recognition and transport by glucose transporters. Nature 526, 391-396 (2015).

170 Forrest, L. R. & Rudnick, G. The rocking bundle: a mechanism for ion-coupled solute flux by symmetrical transporters. Physiology 24, 377-386 (2009).

171 Lee, C. et al. A two-domain elevator mechanism for sodium/proton antiport. Nature 501, 573-577 (2013).

172 Reyes, N., Ginter, C. & Boudker, O. Transport mechanism of a bacterial homologue of glutamate transporters. Nature 462, 880-885 (2009).

173 Jack, D. L., Yang, N. M. & Saier, M. H., Jr. The drug/metabolite transporter superfamily. Eur J Biochem 268, 3620-3639, doi:10.1046/j.1432-1327.2001.02265.x (2001).

174 Lolkema, J. S., Dobrowolski, A. & Slotboom, D.-J. Evolution of antiparallel two-domain membrane proteins: tracing multiple gene duplication events in the DUF606 family. Journal of molecular biology 378, 596-606 (2008).

175 Vastermark, A., Almen, M. S., Simmen, M. W., Fredriksson, R. & Schioth, H. B. Functional specialization in nucleotide sugar transporters occurred through differentiation of the gene cluster EamA (DUF6) before the radiation of Viridiplantae. BMC Evol Biol 11, 123, doi:10.1186/1471-2148-11-123 (2011).

176 Bay, D. C. & Turner, R. J. Diversity and evolution of the small multidrug resistance protein family. BMC evolutionary biology 9, 1-27 (2009).

177 Ubarretxena-Belandia, I., Baldwin, J. M., Schuldiner, S. & Tate, C. G. Three-dimensional structure of the bacterial multidrug transporter EmrE shows it is an asymmetric homodimer. The EMBO journal 22, 6175-6181 (2003).
178 Chen, Y.-J. et al. X-ray structure of EmrE supports dual topology model. Proceedings of the National Academy of Sciences 104, 18999-19004 (2007).
179 Kermani, A. A. et al. The structural basis of promiscuity in small multidrug resistance transporters. Nat Commun 11, 6064, doi:10.1038/s41467-020-19820-8 (2020).
180 Pornillos, O., Chen, Y.-J., Chen, A. P. & Chang, G. X-ray structure of the EmrE multidrug transporter in complex with a substrate. Science 310, 1950-1953 (2005).
181 Tsuchiya, H. et al. Structural basis for amino acid export by DMT superfamily transporter YddG. Nature 534, 417-420, doi:10.1038/nature17991 (2016).
182 Doroshenko, V. et al. YddG from Escherichia coli promotes export of aromatic amino acids. FEMS microbiology letters 275, 312-318 (2007).
183 Santiviago, C. A. et al. The Salmonella enterica sv. Typhimurium smvA, yddG and ompD (porin) genes are required for the efficient efflux of methyl viologen. Mol Microbiol 46, 687-698, doi:10.1046/j.1365-2958.2002.03204.x (2002).
184 Forrest, L. R. (Pseudo-) symmetrical transport. Science 339, 399-401 (2013).
185 Liao, J. et al. Structural insight into the ion-exchange mechanism of the sodium/calcium exchanger. Science 335, 686-690 (2012).
186 Lee, Y. et al. Structure of the triose-phosphate/phosphate translocator reveals the basis of substrate specificity. Nat Plants 3, 825-832, doi:10.1038/s41477-017-0022-8 (2017).
187 Ahuja, S. & Whorton, M. R. Structural basis for mammalian nucleotide sugar transport. Elife 8, doi:10.7554/eLife.45221 (2019).
188 Nji, E., Gulati, A., Qureshi, A. A., Coincon, M. & Drew, D. Structural basis for the delivery of activated sialic acid into Golgi for sialyation. Nat Struct Mol Biol 26, 415-423, doi:10.1038/s41594-019-0225-y (2019).
189 Parker, J. L., Corey, R. A., Stansfeld, P. J. & Newstead, S. Structural basis for substrate specificity and regulation of nucleotide sugar transporters in the lipid bilayer. Nat Commun 10, 4657, doi:10.1038/s41467-019-12673-w (2019).
190 Parker, J. L. & Newstead, S. Structural basis of nucleotide sugar transport across the Golgi membrane. Nature 551, 521-524, doi:10.1038/nature24464 (2017).
191 Ishida, N. & Kawakita, M. Molecular physiology and pathology of the nucleotide sugar transporter family (SLC35). Pflügers Archiv 447, 768-775 (2004).

192 Song, Z. Roles of the nucleotide sugar transporters (SLC35 family) in health and disease. Molecular aspects of medicine 34, 590-600 (2013).
193 Colas, C., Ung, P. M.-U. & Schlessinger, A. SLC transporters: structure, function, and drug discovery. Medchemcomm 7, 1069-1081 (2016).
194 Lin, L., Yee, S. W., Kim, R. B. & Giacomini, K. M. SLC transporters as therapeutic targets: emerging opportunities. Nature reviews Drug discovery 14, 543-560 (2015).
195 Perland, E. & Fredriksson, R. Classification systems of secondary active transporters. Trends in pharmacological sciences 38, 305-315 (2017).
196 Weber, A. P. & Linka, N. Connecting the plastid: transporters of the plastid envelope and their role in linking plastidial with cytosolic metabolism. Annual review of plant biology 62, 53-77 (2011).
197 Weber, A. P., Linka, M. & Bhattacharya, D. Single, ancient origin of a plastid metabolite translocator family in Plantae from an endomembrane-derived ancestor. Eukaryotic Cell 5, 609-612 (2006).
198 Knappe, S., Flugge, U. I. & Fischer, K. Analysis of the plastidic phosphate translocator gene family in Arabidopsis and identification of new phosphate translocator-homologous transporters, classified by their putative substrate-binding site. Plant Physiol 131, 1178-1190, doi:10.1104/pp.016519 (2003).
199 Hadley, B. et al. Structure and function of nucleotide sugar transporters: current progress. Computational and structural biotechnology journal 10, 23-32 (2014).
200 Orellana, A., Moraga, C., Araya, M. & Moreno, A. Overview of nucleotide sugar transporter gene family functions across multiple species. Journal of molecular biology 428, 3150-3165 (2016).
201 Heldt, H. W. & Rapley, L. Specific transport of inorganic phosphate, 3-phosphoglycerate and dihydroxyacetonephosphate, and of dicarboxylates across the inner membrane of spinach chloroplasts. FEBS Lett 10, 143-148, doi:10.1016/0014-5793(70)80438-0 (1970).
202 Su, X.-z., Lane, K. D., Xia, L., Sá, J. M. & Wellems, T. E. Plasmodium genomics and genetics: new insights into malaria pathogenesis, drug resistance, epidemiology, and evolution. Clinical microbiology reviews 32, e00019-00019 (2019).
203 Blasco, B., Leroy, D. & Fidock, D. A. Antimalarial drug resistance: linking Plasmodium falciparum parasite biology to the clinic. Nature medicine 23, 917-928 (2017).
204 Flügge, U.-I. Phosphate translocators in plastids. Annual review of plant biology 50, 27-45 (1999).

205 Hodgkin, A. L. & Huxley, A. F. The components of membrane conductance in the giant axon of Loligo. The Journal of physiology 116, 473-496 (1952).
206 Cole, K. S. Dynamic electrical characteristics of the squid axon membrane. Archives des sciences physiologiques 3, 253-258 (1949).
207 Neher, E. in Single-channel recording 147-153 (Springer, 1995).
208 Penner, R. in Single-channel recording 3-30 (Springer, 1995).
209 Sakmann, B. & Neher, E. in Single-channel recording 37-51 (Springer, 1983).
210 Neher, E. & Sakmann, B. Single-channel currents recorded from membrane of denervated frog muscle fibres. Nature 260, 799-802 (1976).
211 Kusano, K., Miledi, R. & Stinnakre, J. Acetylcholine receptors in the oocyte membrane. Nature 270, 739-741 (1977).
212 Umbach, J., Coady, M. & Wright, E. Intestinal Na+/glucose cotransporter expressed in Xenopus oocytes is electrogenic. Biophysical Journal 57, 1217-1224 (1990).
213 Hediger, M. A., Ikeda, T., Coady, M., Gundersen, C. B. & Wright, E. M. Expression of size-selected mRNA encoding the intestinal Na/glucose cotransporter in Xenopus laevis oocytes. Proceedings of the National Academy of Sciences 84, 2634-2637 (1987).
214 Schulz, P., Garcia-Celma, J. J. & Fendler, K. SSM-based electrophysiology. Methods 46, 97-103 (2008).
215 Drachev, L. et al. Direct measurement of electric current generation by cytochrome oxidase, H+-ATPase and bacteriorhodopsin. Nature 249, 321-324 (1974).
216 Geibel, S., Flores-Herr, N., Licher, T. & Vollert, H. Establishment of cell-free electrophysiology for ion transporters: application for pharmacological profiling. Journal of biomolecular screening 11, 262-268 (2006).
217 Garcia-Celma, J. J. et al. Rapid activation of the melibiose permease MelB immobilized on a solid-supported membrane. Langmuir 24, 8119-8126 (2008).
218 Bazzone, A., Barthmes, M. & Fendler, K. in Methods in enzymology Vol. 594 31-83 (Elsevier, 2017).
219 Kendrew, J. C. et al. A three-dimensional model of the myoglobin molecule obtained by x-ray analysis. Nature 181, 662-666 (1958).
220 Blake, C. et al. Structure of hen egg-white lysozyme: a three-dimensional Fourier synthesis at 2 Å resolution. Nature 206, 757-761 (1965).
221 Johnson, L. N. & Phillips, D. Structure of some crystalline lysozyme-inhibitor complexes determined by X-ray analysis at 6 Å resolution. Nature 206, 761-763 (1965).

222 Ferreira, L. G., Dos Santos, R. N., Oliva, G. & Andricopulo, A. D. Molecular docking and structure-based drug design strategies. Molecules 20, 13384-13421 (2015).
223 Choy, B. C., Cater, R. J., Mancia, F. & Pryor Jr, E. E. A 10-year meta-analysis of membrane protein structural biology: detergents, membrane mimetics, and structure determination techniques. Biochimica et Biophysica Acta (BBA)-Biomembranes 1863, 183533 (2021).
224 Seddon, A. M., Curnow, P. & Booth, P. J. Membrane proteins, lipids and detergents: not just a soap opera. Biochimica et Biophysica Acta (BBA)-Biomembranes 1666, 105-117 (2004).
225 Moraes, I., Evans, G., Sanchez-Weatherby, J., Newstead, S. & Stewart, P. D. S. Membrane protein structure determination—the next generation. Biochimica et Biophysica Acta (BBA)-Biomembranes 1838, 78-87 (2014).
226 Stetsenko, A. & Guskov, A. An overview of the top ten detergents used for membrane protein crystallization. Crystals 7, 197 (2017).
227 Bayburt, T. H., Grinkova, Y. V. & Sligar, S. G. Self-assembly of discoidal phospholipid bilayer nanoparticles with membrane scaffold proteins. Nano letters 2, 853-856 (2002).
228 Bayburt, T. H. & Sligar, S. G. Membrane protein assembly into Nanodiscs. FEBS letters 584, 1721-1727 (2010).
229 Teo, A. C. et al. Analysis of SMALP co-extracted phospholipids shows distinct membrane environments for three classes of bacterial membrane protein. Scientific Reports 9, 1-10 (2019).
230 Nikolaev, M. et al. Integral membrane proteins can be crystallized directly from nanodiscs. Crystal Growth & Design 17, 945-948 (2017).
231 Broecker, J., Eger, B. T. & Ernst, O. P. Crystallogenesis of membrane proteins mediated by polymer-bounded lipid nanodiscs. Structure 25, 384-392 (2017).
232 Qiu, W. et al. Structure and activity of lipid bilayer within a membrane-protein transporter. Proceedings of the National Academy of Sciences 115, 12985-12990 (2018).
233 Su, C.-C. et al. Cryo-electron microscopy structure of an Acinetobacter baumannii multidrug efflux pump. MBio 10, e01295-01219 (2019).
234 Shen, P. S. et al. The structure of the polycystic kidney disease channel PKD2 in lipid nanodiscs. Cell 167, 763-773. e711 (2016).
235 Perez, C. & Maier, T. Expression, Purification, and Structural Biology of Membrane Proteins. (Springer, 2020).
236 Ma, P. et al. The cubicon method for concentrating membrane proteins in the cubic mesophase. nature protocols 12, 1745-1762 (2017).

237 Newstead, S., Ferrandon, S. & Iwata, S. Rationalizing α-helical membrane protein crystallization. Protein Science 17, 466-472 (2008).
238 Parker, J. L. & Newstead, S. Current trends in α-helical membrane protein crystallization: an update. Protein Science 21, 1358-1365 (2012).
239 Newstead, S., Hobbs, J., Jordan, D., Carpenter, E. P. & Iwata, S. Insights into outer membrane protein crystallization. Molecular membrane biology 25, 631-638 (2008).
240 Qiu, H. & Caffrey, M. The phase diagram of the monoolein/water system: metastability and equilibrium aspects. Biomaterials 21, 223-234 (2000).
241 Landau, E. M. & Rosenbusch, J. P. Lipidic cubic phases: a novel concept for the crystallization of membrane proteins. Proceedings of the National Academy of Sciences 93, 14532-14535 (1996).
242 Hunte, C. & Michel, H. Crystallisation of membrane proteins mediated by antibody fragments. Current opinion in structural biology 12, 503-508 (2002).
243 Carpenter, E. P., Beis, K., Cameron, A. D. & Iwata, S. Overcoming the challenges of membrane protein crystallography. Current opinion in structural biology 18, 581-586 (2008).
244 Desmyter, A. et al. Crystal structure of a camel single-domain VH antibody fragment in complex with lysozyme. Nature structural biology 3, 803-811 (1996).
245 Rasmussen, S. G. et al. Structure of a nanobody-stabilized active state of the beta(2) adrenoceptor. Nature 469, 175-180, doi:10.1038/nature09648 (2011).
246 Zimmermann, I. et al. Synthetic single domain antibodies for the conformational trapping of membrane proteins. Elife 7, doi:10.7554/eLife.34317 (2018).
247 Sivia, D. S. Elementary scattering theory: for X-ray and neutron users. (Oxford University Press, 2011).
248 Murata, K. & Wolf, M. Cryo-electron microscopy for structural analysis of dynamic biological macromolecules. Biochimica et Biophysica Acta (BBA)-General Subjects 1862, 324-334 (2018).
249 Zanotti, G. & Grinzato, A. Structure of filamentous viruses. Current Opinion in Virology 51, 25-33 (2021).
250 Assaiya, A., Burada, A. P., Dhingra, S. & Kumar, J. An overview of the recent advances in cryo-electron microscopy for life sciences. Emerging Topics in Life Sciences 5, 151-168 (2021).
251 Nygaard, R., Kim, J. & Mancia, F. Cryo-electron microscopy analysis of small membrane proteins. Current Opinion in Structural Biology 64, 26-33 (2020).

252 Frank, J. Three-dimensional electron microscopy of macromolecular assemblies: visualization of biological molecules in their native state. (Oxford university press, 2006).
253 Bloch, M., Santiveri, M. & Taylor, N. M. in Expression, Purification, and Structural Biology of Membrane Proteins 227-244 (Springer, 2020).
254 Efremov, R. G., Gatsogiannis, C. & Raunser, S. in Methods in enzymology Vol. 594 1-30 (Elsevier, 2017).
255 Liu, S. et al. Cryo-EM structure of the human α5β3 GABAA receptor. Cell research 28, 958-961 (2018).
256 Deneka, D. et al. Allosteric modulation of LRRC8 channels by targeting their cytoplasmic domains. Nature communications 12, 1-14 (2021).
257 Uchański, T. et al. Megabodies expand the nanobody toolkit for protein structure determination by single-particle cryo-EM. Nature methods 18, 60-68 (2021).
258 Kim, J. et al. Structure and drug resistance of the Plasmodium falciparum transporter PfCRT. Nature 576, 315-320, doi:10.1038/s41586-019-1795-x (2019).
259 Tsutsumi, N. et al. Structure of human Frizzled5 by fiducial-assisted cryo-EM supports a heterodimeric mechanism of canonical Wnt signaling. Elife 9, e58464 (2020).
260 Yao, Q., Weaver, S. J., Mock, J.-Y. & Jensen, G. J. Fusion of DARPin to aldolase enables visualization of small protein by cryo-EM. Structure 27, 1148-1155. e1143 (2019).
261 Frank, J. et al. A model of protein synthesis based on cryo-electron microscopy of the E. coli ribosome. Nature 376, 441-444 (1995).
262 Skiniotis, G. & Southworth, D. R. Single-particle cryo-electron microscopy of macromolecular complexes. Microscopy 65, 9-22 (2016).
263 Kondo, A., Muranaka, Y., Ohta, I. & Kanno, T. Dynamic reaction in a homogeneous HDL-cholesterol assay visualized by electron microscopy. Clinical chemistry 45, 1974-1980 (1999).
264 Dubochet, J. et al. Cryo-electron microscopy of vitrified specimens. Quarterly reviews of biophysics 21, 129-228 (1988).
265 Adrian, M., Dubochet, J., Lepault, J. & McDowall, A. W. Cryo-electron microscopy of viruses. Nature 308, 32-36 (1984).
266 Dubochet, J., Lepault, J., Freeman, R., Berriman, J. & Homo, J. C. Electron microscopy of frozen water and aqueous solutions. Journal of Microscopy 128, 219-237 (1982).
267 Brenner, S. & Horne, R. A negative staining method for high resolution electron microscopy of viruses. Biochimica et biophysica acta 34, 103-110 (1959).

268 Kiselev, N., Sherman, M. & Tsuprun, V. Negative staining of proteins. Electron Microscopy Reviews 3, 43-72 (1990).
269 Chen, J. Z. et al. A dose-rate effect in single-particle electron microscopy. Journal of structural biology 161, 92-100 (2008).
270 Yip, K. M., Fischer, N., Paknia, E., Chari, A. & Stark, H. Atomic-resolution protein structure determination by cryo-EM. Nature 587, 157-161 (2020).
271 Nakane, T. et al. Single-particle cryo-EM at atomic resolution. Nature 587, 152-156 (2020).
272 Williams, D. B. & Carter, C. B. in Transmission electron microscopy 3-17 (Springer, 1996).
273 Stowell, M., Miyazawa, A. & Unwin, N. Macromolecular structure determination by electron microscopy: new advances and recent results. Current opinion in structural biology 8, 595-600 (1998).
274 Kasper, E. Field electron emission systems. (1982).
275 Reimer, L. Transmission electron microscopy: physics of image formation and microanalysis. Vol. 36 (Springer, 2013).
276 Booth, C. R., Jakana, J. & Chiu, W. Assessing the capabilities of a 4kx4k CCD camera for electron cryo-microscopy at 300 kV. Journal of structural biology 156, 556-563 (2006).
277 Sander, B., Golas, M. & Stark, H. Advantages of CCD detectors for de novo three-dimensional structure determination in single-particle electron microscopy. Journal of structural biology 151, 92-105 (2005).
278 Milazzo, A.-C. et al. Initial evaluation of a direct detection device detector for single particle cryo-electron microscopy. Journal of structural biology 176, 404-408 (2011).
279 Jin, L. et al. Applications of direct detection device in transmission electron microscopy. Journal of structural biology 161, 352-358 (2008).
280 Bammes, B. E., Rochat, R. H., Jakana, J., Chen, D.-H. & Chiu, W. Direct electron detection yields cryo-EM reconstructions at resolutions beyond 3/4 Nyquist frequency. Journal of structural biology 177, 589-601 (2012).
281 Mendez, J. H., Mehrani, A., Randolph, P. & Stagg, S. Throughput and resolution with a next-generation direct electron detector. IUCrJ 6, 1007-1013 (2019).
282 Russo, C. J. & Henderson, R. Microscopic charge fluctuations cause minimal contrast loss in cryoEM. Ultramicroscopy 187, 56-63 (2018).
283 Ripstein, Z. & Rubinstein, J. Processing of cryo-EM movie data. Methods in enzymology 579, 103-124 (2016).

284 Rubinstein, J. L. & Brubaker, M. A. Alignment of cryo-EM movies of individual particles by optimization of image translations. Journal of structural biology 192, 188-195 (2015).
285 Saad, A. et al. Fourier amplitude decay of electron cryomicroscopic images of single particles and effects on structure determination. Journal of structural biology 133, 32-42 (2001).
286 Amos, L., Henderson, R. & Unwin, P. Three-dimensional structure determination by electron microscopy of two-dimensional crystals. Progress in biophysics and molecular biology 39, 183-231 (1982).
287 Slayter, E. M. & Slayter, H. S. Light and electron microscopy. (Cambridge University Press, 1992).
288 Erickson, H. & Klug, A. Measurement and compensation of defocusing and aberrations by Fourier processing of electron micrographs. Philosophical Transactions of the Royal Society of London. B, Biological Sciences 261, 105-118 (1971).
289 Zhu, J., Penczek, P. A., Schröder, R. & Frank, J. Three-dimensional reconstruction with contrast transfer function correction from energy-filtered cryoelectron micrographs: procedure and application to the 70sescherichia coliribosome. Journal of structural biology 118, 197-219 (1997).
290 Scheres, S. H. RELION: implementation of a Bayesian approach to cryo-EM structure determination. Journal of structural biology 180, 519-530 (2012).
291 Punjani, A., Rubinstein, J. L., Fleet, D. J. & Brubaker, M. A. cryoSPARC: algorithms for rapid unsupervised cryo-EM structure determination. Nat Methods 14, 290-296, doi:10.1038/nmeth.4169 (2017).
292 MacKay, D. J. & Mac Kay, D. J. Information theory, inference and learning algorithms. (Cambridge university press, 2003).
293 Sigworth, F. J., Doerschuk, P. C., Carazo, J.-M. & Scheres, S. H. in Methods in enzymology Vol. 482 263-294 (Elsevier, 2010).
294 Noble, A. J. et al. Reducing effects of particle adsorption to the air–water interface in cryo-EM. Nature methods 15, 793-795 (2018).
295 Tan, Y. Z. et al. Addressing preferred specimen orientation in single-particle cryo-EM through tilting. Nature methods 14, 793-796 (2017).
296 Orlova, E. & Saibil, H. R. Structural analysis of macromolecular assemblies by electron microscopy. Chemical reviews 111, 7710-7748 (2011).
297 Scheres, S. H. A Bayesian view on cryo-EM structure determination. Journal of molecular biology 415, 406-418 (2012).
298 Henderson, R. Avoiding the pitfalls of single particle cryo-electron microscopy: Einstein from noise. Proceedings of the National Academy of Sciences 110, 18037-18041 (2013).

299 Belnap, D. M., Olson, N. H. & Baker, T. S. A method for establishing the handedness of biological macromolecules. Journal of structural biology 120, 44-51 (1997).
300 Rosenthal, P. B. & Henderson, R. Optimal determination of particle orientation, absolute hand, and contrast loss in single-particle electron cryomicroscopy. J Mol Biol 333, 721-745, doi:10.1016/j.jmb.2003.07.013 (2003).
301 Liao, H. Y. & Frank, J. Definition and estimation of resolution in single-particle reconstructions. Structure 18, 768-775 (2010).
302 Henderson, R. et al. Outcome of the first electron microscopy validation task force meeting. Structure 20, 205-214 (2012).
303 Wu, S. et al. Fabs enable single particle cryoEM studies of small proteins. Structure 20, 582-592, doi:10.1016/j.str.2012.02.017 (2012).
304 Rawson, S., Iadanza, M., Ranson, N. & Muench, S. Methods to account for movement and flexibility in cryo-EM data processing. Methods 100, 35-41 (2016).
305 Hahn, A., Vonck, J., Mills, D. J., Meier, T. & Kühlbrandt, W. Structure, mechanism, and regulation of the chloroplast ATP synthase. Science 360, eaat4318 (2018).
306 Daum, B. et al. Structure and in situ organisation of the Pyrococcus furiosus archaellum machinery. Elife 6, e27470 (2017).
307 Overington, J. P., Al-Lazikani, B. & Hopkins, A. L. How many drug targets are there? Nature reviews Drug discovery 5, 993-996 (2006).
308 Jumper, J. et al. Highly accurate protein structure prediction with AlphaFold. Nature 596, 583-589 (2021).
309 Varadi, M. et al. AlphaFold Protein Structure Database: Massively expanding the structural coverage of protein-sequence space with high-accuracy models. Nucleic acids research 50, D439-D444 (2022).
310 Baek, M. et al. Accurate prediction of protein structures and interactions using a three-track neural network. Science 373, 871-876 (2021).
311 Fidock, D. A. et al. Mutations in the P. falciparum digestive vacuole transmembrane protein PfCRT and evidence for their role in chloroquine resistance. Mol Cell 6, 861-871, doi:10.1016/s1097-2765(05)00077-8 (2000).
312 Aidoo, A. Y. & Ward, K. Spatio-temporal concentration of acetylcholine in vertebrate synaptic cleft. Mathematical and computer modelling 44, 952-962 (2006).
313 Barbier, M. et al. Novel phosphorylcholine-containing protein of Pseudomonas aeruginosa chronic infection isolates interacts with airway epithelial cells. J Infect Dis 197, 465-473, doi:10.1086/525048 (2008).

314 Bondy, J. et al. Haemophilus influenzae LicB contributes to lung damage in an aged mice co-infection model. Microb Pathog 90, 1-6, doi:10.1016/j.micpath.2015.10.010 (2016).
315 Harper, M. et al. Decoration of Pasteurella multocida lipopolysaccharide with phosphocholine is important for virulence. J Bacteriol 189, 7384-7391, doi:10.1128/JB.00948-07 (2007).
316 Swords, W. E. et al. Binding of the non-typeable Haemophilus influenzae lipooligosaccharide to the PAF receptor initiates host cell signalling. Cell Microbiol 3, 525-536, doi:10.1046/j.1462-5822.2001.00132.x (2001).
317 Kharat, A. S. & Tomasz, A. Drastic reduction in the virulence of Streptococcus pneumoniae expressing type 2 capsular polysaccharide but lacking choline residues in the cell wall. Mol Microbiol 60, 93-107, doi:10.1111/j.1365-2958.2006.05082.x (2006).
318 Muyldermans, S. Nanobodies: natural single-domain antibodies. Annual review of biochemistry 82, 775-797 (2013).
319 Muyldermans, S., Cambillau, C. & Wyns, L. Recognition of antigens by single-domain antibody fragments: the superfluous luxury of paired domains. Trends in biochemical sciences 26, 230-235 (2001).
320 McMahon, C. et al. Yeast surface display platform for rapid discovery of conformationally selective nanobodies. Nature structural & molecular biology 25, 289-296 (2018).
321 Pardon, E. et al. A general protocol for the generation of Nanobodies for structural biology. Nature protocols 9, 674-693 (2014).
322 Yan, J., Li, G., Hu, Y., Ou, W. & Wan, Y. Construction of a synthetic phage-displayed Nanobody library with CDR3 regions randomized by trinucleotide cassettes for diagnostic applications. Journal of translational medicine 12, 1-12 (2014).
323 Liu, M., Li, L., Jin, D. & Liu, Y. Nanobody—A versatile tool for cancer diagnosis and therapeutics. Wiley Interdisciplinary Reviews: Nanomedicine and Nanobiotechnology 13, e1697 (2021).
324 Morrison, C. Nanobody approval gives domain antibodies a boost. Nature Reviews Drug Discovery 18, 485-488 (2019).
325 D Cromie, K., Van Heeke, G. & Boutton, C. Nanobodies and their use in GPCR drug discovery. Current Topics in Medicinal Chemistry 15, 2543-2557 (2015).
326 Rajarathnam, K. & Rösgen, J. Isothermal titration calorimetry of membrane proteins—Progress and challenges. Biochimica et Biophysica Acta (BBA)-Biomembranes 1838, 69-77 (2014).
327 Salamon, Z., Wang, Y., Soulages, J., Brown, M. & Tollin, G. Surface plasmon resonance spectroscopy studies of membrane proteins: transducin binding

and activation by rhodopsin monitored in thin membrane films. Biophysical journal 71, 283-294 (1996).
328 Jerabek-Willemsen, M. et al. MicroScale Thermophoresis: Interaction analysis and beyond. Journal of Molecular Structure 1077, 101-113 (2014).
329 Okuda, T. & Haga, T. Functional characterization of the human high-affinity choline transporter. FEBS Lett 484, 92-97, doi:10.1016/s0014-5793(00)02134-7 (2000).
330 Apparsundaram, S., Ferguson, S. M., George Jr, A. L. & Blakely, R. D. Molecular cloning of a human, hemicholinium-3-sensitive choline transporter. Biochemical and biophysical research communications 276, 862-867 (2000).
331 Ferguson, S. M. et al. Lethal impairment of cholinergic neurotransmission in hemicholinium-3-sensitive choline transporter knockout mice. Proceedings of the National Academy of Sciences 101, 8762-8767 (2004).
332 Gualerzi, C. O., Brandi, L., Fabbretti, A. & Pon, C. L. Antibiotics: targets, mechanisms and resistance. (John Wiley & Sons, 2013).
333 Årdal, C. et al. Antibiotic development—economic, regulatory and societal challenges. Nature Reviews Microbiology 18, 267-274 (2020).
334 Woolf, P. J. & Linderman, J. J. Self organization of membrane proteins via dimerization. Biophysical chemistry 104, 217-227 (2003).
335 Chadda, R. et al. Membrane transporter dimerization driven by differential lipid solvation energetics of dissociated and associated states. Elife 10, e63288 (2021).
336 Gupta, K. et al. The role of interfacial lipids in stabilizing membrane protein oligomers. Nature 541, 421-424 (2017).
337 Škerle, J. et al. Membrane protein dimerization in cell-derived lipid membranes measured by FRET with MC simulations. Biophysical journal 118, 1861-1875 (2020).
338 Hadley, B. et al. Nucleotide sugar transporter SLC35 family structure and function. Computational and structural biotechnology journal 17, 1123-1134 (2019).
339 Wallin, E. & Heijne, G. V. Genome-wide analysis of integral membrane proteins from eubacterial, archaean, and eukaryotic organisms. Protein Science 7, 1029-1038 (1998).
340 Gong, J. et al. Understanding membrane protein drug targets in computational perspective. Current Drug Targets 20, 551-564 (2019).
341 Li, F. et al. Highlighting membrane protein structure and function: A celebration of the Protein Data Bank. Journal of Biological Chemistry 296 (2021).
342 Yin, H. & Flynn, A. D. Drugging membrane protein interactions. Annual review of biomedical engineering 18, 51-76 (2016).